Near-Infrared Polarimetric Survey toward the Galactic Center

– The Efficiency and Wavelength Dependence of Interstellar Polarization –

A dissertation submitted to
the Department of Astrophysics of Nagoya University
in partial satisfaction of the requirements for
the degree of Doctor of Philosophy in Astrophysics

by

Hirofumi Hatano

January 2010

Abstract

Non-spherical dust grains rotating in a magnetic field are aligned with their rotational axes parallel to the direction of the magnetic field via paramagnetic relaxation. Starlight passing through a cloud of such dust grains is caused to be linearly polarized parallel to the magnetic field direction on the plane-of-the-sky. This is called interstellar polarization. Observations of interstellar polarization yield information of the magnetic field and properties of polarizing dust grains.

Near-infrared polarimetric imaging survey toward the Galactic center has been carried out with the IRSF 1.4 m telescope, near-infrared camera SIRIUS, and its polarimeter SIRPOL. A total area of about 7.6 deg^2 is covered in the J, H, and K_S bands. From analyzed data of about 5.7 deg^2 area, we catalogued positions, degrees of polarization, position angles, and magnitudes in the JHK_S bands for about 3.5 million point sources.

We investigated the magnetic field toward the Galactic center. Position angles are nearly parallel to the Galactic plane, indicating that the magnetic field between the Galactic center and us runs almost parallel to the spiral arms. Compared to the interstellar medium close to us, the interstellar medium between the Galactic center and us shows lower polarization efficiency (ratio of degree of polarization to color excess). Moreover we investigated the spatial variation of the polarization efficiency by comparing it with those of color excess, degree of polarization, and position angle. The spatial variations of color excess and degree of polarization depend on Galactic latitude, while the polarization efficiency varies independently of the Galactic structure. The polarization efficiency anti-correlates with dispersions of position angles. Low polarization efficiency and its spatial variation can be explained by the differences of the magnetic field directions along the line-of-sight. The low polarization efficiency suggests that a random component of magnetic field predominates over a uniform component in magnetic field strength between the GC and us.

We also derived the ratios of degree of polarization $p_H/p_J = 0.581 \pm 0.004$ and $p_{K_S}/p_H = 0.620 \pm 0.002$, giving $\beta_{JH} = 2.08 \pm 0.02$ and $\beta_{HK_S} = 1.76 \pm 0.01$ as the power law indices of the wavelength dependence of interstellar polarization. The wavelength dependence of interstellar polarization exhibits flattening toward longer wavelengths in the range of 1.25$-$2.14 μm, invoking great numbers of aligned large-size dust grains.

Contents

1 Introduction **1**
- 1.1 Polarization in Astronomy . . . 1
  - 1.1.1 History of Astronomical Polarimetry . . . 1
  - 1.1.2 Nature of Astronomical Polarization at the Optical and NIR Wavelengths . . . 1
- 1.2 The Galaxy – Dust and Magnetic Field – . . . 4
- 1.3 This Study . . . 7

2 NIR Polarimetric Survey toward the GC **12**
- 2.1 IRSF . . . 12
  - 2.1.1 1.4 m Telescope . . . 12
  - 2.1.2 SIRIUS . . . 12
  - 2.1.3 SIRPOL . . . 15
  - 2.1.4 Site . . . 16
- 2.2 Observations . . . 16

3 Data Reduction and Analysis **22**
- 3.1 Data Reduction . . . 23
- 3.2 Data Analysis for Point Sources . . . 23
  - 3.2.1 Photometry . . . 23
  - 3.2.2 Polarimetry . . . 25
  - 3.2.3 Astrometry . . . 28
  - 3.2.4 Catalog . . . 28
- 3.3 Data Quality for Point Sources . . . 31
  - 3.3.1 Seeing . . . 31
  - 3.3.2 Photometric Accuracy . . . 31
  - 3.3.3 Polarimetric Accuracy . . . 31
  - 3.3.4 Astrometric Accuracy . . . 34
  - 3.3.5 Limiting Magnitude . . . 34
- 3.4 Data Analysis for Extended Sources . . . 39

4 Polarization Efficiency toward the GC **41**
- 4.1 Introduction . . . 41
- 4.2 Results . . . 45
  - 4.2.1 MK Classifications and Locations . . . 45

4.2.2 Color Excess . . . 45
4.2.3 Degree of Polarization and Position Angle . . . 49
4.2.4 Polarization Efficiency . . . 54
4.3 Discussion . . . 57
4.3.1 Low Polarization Efficiency and Its Spatial Variation . . . 57
4.3.2 Magnetic Field Strength Ratio of the Random to the Uniform Component . . . 59
4.4 Conclusion . . . 61

5 Wavelength Dependence of Polarization toward the GC 64
5.1 Introduction . . . 64
5.2 Results . . . 67
5.3 Discussion . . . 69
5.4 Conclusion . . . 71

6 Summary 74

A Extended Polarized Sources toward the GC 76
A.1 Search for Extended Polarized Sources . . . 76
A.2 Each Extended Polarized Source . . . 89
A.3 Conclusion . . . 95

B Interstellar Extinction Map toward the GC 97
B.1 Introduction . . . 97
B.2 Results and Discussion . . . 101
B.3 Conclusion . . . 104

Chapter 1

Introduction

1.1 Polarization in Astronomy

Polarization yields information about asymmetry inherent in the astronomical configuration, which cannot be available from other methods of observation except polarimetry. In this section, we review a brief history of astronomical polarimetry and nature of astronomical polarization at the optical and near-infrared (NIR) wavelengths.

1.1.1 History of Astronomical Polarimetry

In 1923, Lyot performed polarimetry of the sunlight scattered by Venus; this is the start of polarimetry as an effective astronomical technique (Tinbergen 1996). Chandrasekhar (1946) introduced the Stokes parameters into astronomy and predicted that linear polarization (hereafter just polarization) of starlight from an early-type star in an eclipsing binary system due to scattering by electrons can be detected when the early-type star is partially eclipsed by a companion. In order to verify the prediction, Hiltner (1949) and Hall (1949) have made polarimetric observations of early-type stars and unexpectedly found polarization caused by the interstellar medium (ISM). Polarization due to synchrotron radiation was first detected from the Crab Nebula at the optical (Dombrovsky 1954), radio (Mayer et al. 1957), and X-ray (Novick et al. 1972) wavelengths. Since then, progress of polarimetry has continued, and now polarimetry is accepted as a standard but unique observational technique in astronomy.

1.1.2 Nature of Astronomical Polarization at the Optical and Near-Infrared Wavelengths

Astronomical polarization is caused by asymmetry, which is, for example, a configuration of the magnetic field and an asymmetric distribution of scattered radiation. At the optical and NIR wavelengths, polarization due to interstellar polarization, scattering by dust grains and electrons, and synchrotron radiation can be observed. We review the mechanisms related to dust grains except for scattering by electrons and synchrotron

radiation[1].

Interstellar Polarization

Dust grains in the ISM cause extinction, which is attenuation of transmitted light in intensity, by two physical processes – absorption and scattering; the energy of absorbed light is converted into the internal energy (heat) of dust grains, while scattered light is deflected from the line-of-sight (Whittet 2003). Interstellar linear polarization (hereafter just interstellar polarization) results from linear dichroism of non-spherical dust grains aligned by a magnetic field (Fig. 1.1). Dust grains spin by gas collisions, and the spin axes corresponding to their minor axes with the largest moment of inertia are oriented to the direction of a magnetic field by paramagnetic relaxation (Davis & Greenstein 1951; Lazarian 2003, 2007). We consider a medium of non-spherical dust grains (such as long cylinders), which are oriented with their major axes perpendicular to the direction of a magnetic field and to the direction of propagation of starlight. Extinction efficiency factors $Q_{\parallel}$ and $Q_{\perp}$ when the $\boldsymbol{E}$-vector of starlight is parallel and perpendicular to the major axis of the dust grain against size parameter $X = 2\pi a/\lambda$ (a: radius of cylinders, λ: wavelengths of starlight) are shown in Figure 1.2. The difference $\Delta Q = Q_{\parallel} - Q_{\perp}$ causes polarization (differential extinction).

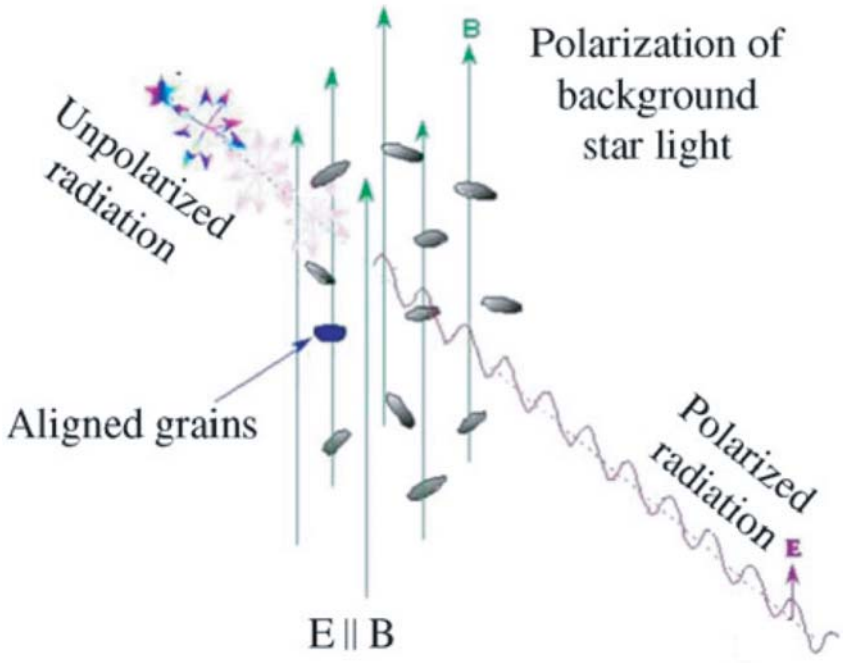

Figure 1.1: Polarization of starlight passing through a medium of aligned dust grains (Fig. 2a of Lazarian 2007). The direction of polarization ($\boldsymbol{E}$) is parallel to the direction of a magnetic field ($\boldsymbol{B}$) on the plane-of-the-sky.

[1]Synchrotron radiation is generated by the acceleration of relativistic electrons through a magnetic field.

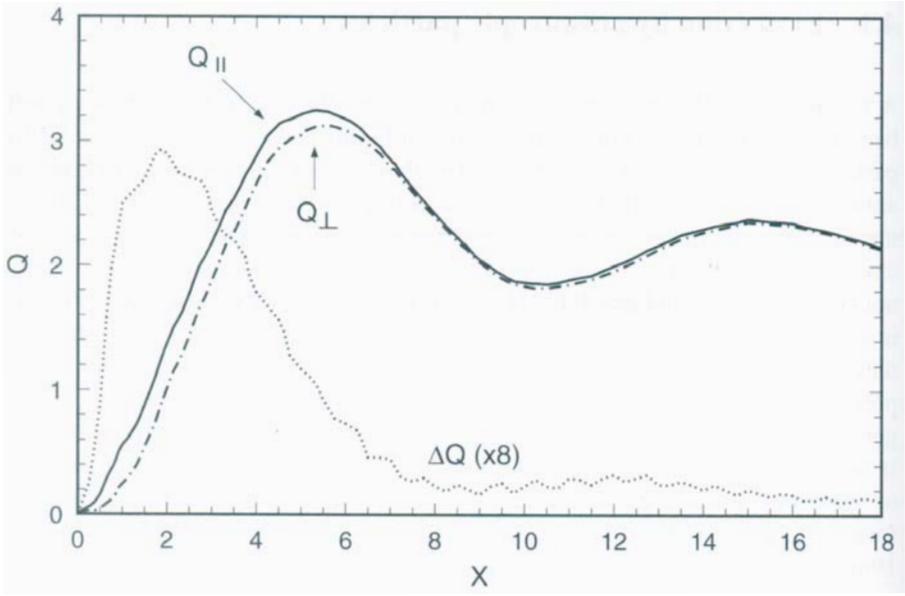

Figure 1.2: $Q_{\parallel}$ (continuous curve) and $Q_{\perp}$ (broken curve) plotted against $X = 2\pi a/\lambda$ for infinite cylinders of radius a and refractive index $1.33 - 0.05$i (Fig. 4.1 of Whittet 2003). The dotted curve shows $\Delta Q = Q_{\parallel} - Q_{\perp}$, scaled up by a factor of eight.

Interstellar circular polarization is also caused by linear birefringence of aligned dust grains; previously generated linear polarization is converted into circular polarization if the directions of magnetic fields, that is, the directions of grain alignment change monotonically along the line-of-sight (Martin 1974).

Observations of interstellar polarization are used to investigate the properties of polarizing dust grains as well as the magnetic field configurations projected on the plane-of-the-sky.

Scattering by Dust Grains

Light scattered by dust grains is linearly polarized. The $\boldsymbol{E}$-vector of the polarized light is perpendicular to the scattering plane, the plane containing the incident and scattered light. Light scattering by dust grains is described by Mie theory, which is solution of Maxwell's equations with appropriate boundary conditions at the surface of dust grains (Mie 1908). At the NIR wavelengths ($\lambda = 1{-}5$ μm), sizes of dust grains ($a \sim 0.01{-}0.1$ μm) are small compared with the wavelengths; in this limit ($X = 2\pi a/\lambda \ll 1$), useful approximation by Rayleigh scattering (Rayleigh 1871) can be used. Suppose that unpolarized light incident on a dust grain, the scattered light in the forward (backward) direction is unpolarized. As the scattering angle increases it is polarized, and when the angle is right angle it is completely linearly polarized (Fig. 1.3*a*).

From polarimetric observations of reflection nebulae, young stellar objects (YSOs), and asymptotic giant branch (AGB) stars, we can get information on illuminating sources and geometry of reflection nebulae, circumstellar structures (dust disk, envelope, shell, etc.) of YSOs and AGB stars (Fig. 1.3*b*).

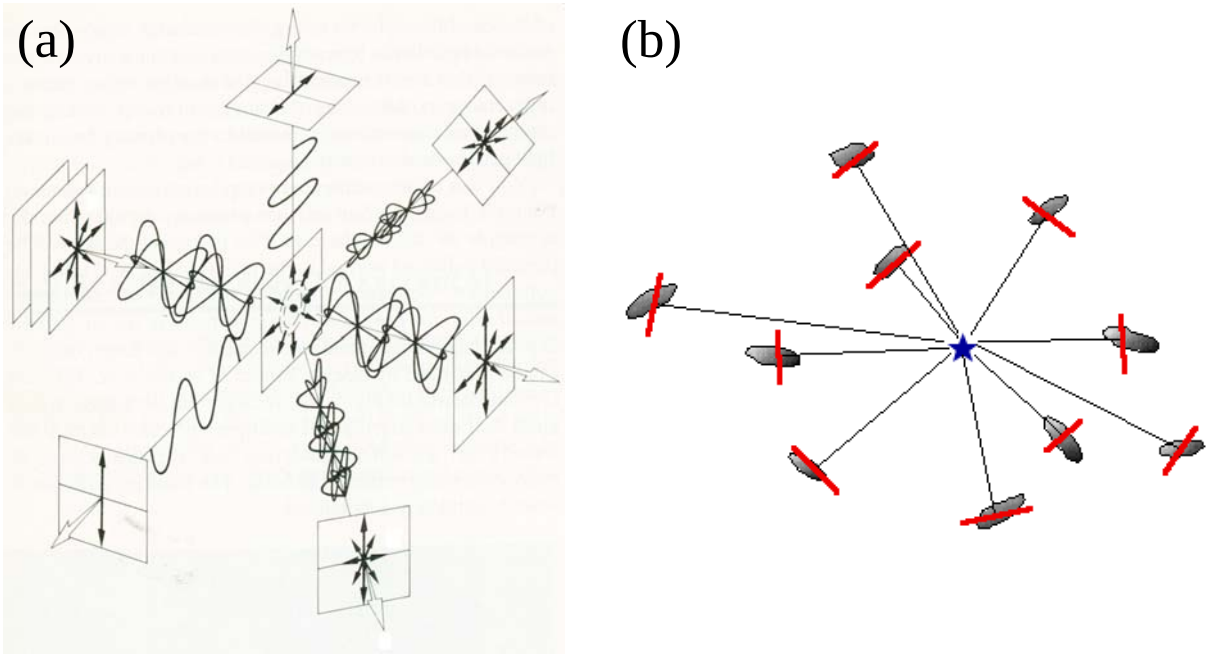

Figure 1.3: (*a*) Scattering of unpolarized light by a dust grain in the case of Rayleigh scattering (Fig. 8.36 of Heckt 1998). (*b*) Polarization of scattered starlight (Fig. 1 of Weintraub et al. 2000; http://www.cfa.harvard.edu/˜agoodman/ppiv/sld007.htm). The observed polarization is perpendicular to light from the illuminating source to the scatterer.

1.2 The Galaxy – Dust and Magnetic Field –

In this section, we introduce general knowledge of dust and magnetic field in the Milky Way Galaxy (hereafter just the Galaxy), which cause polarization.

We begin with the structure of the Galaxy (Fig. 1.4). The most conspicuous feature of the Galaxy is its highly flattened disk of stars with a diameter of about 30 kpc. The densest concentration of stars at the center of the Galaxy is called bulge. It shows a nearly spherical configuration extending out of the disk plane and has a radius about 3 kpc. The bulge mainly comprises of old red giants with relatively low mass. In contrast, the spiral arms in the plane of the Galaxy are configured with young massive stars.

From observations of extinction, the distribution of dust in the Galaxy has been investigated (Fig. 1.5). As a general rule, dust is confined to the Galactic plane, essentially within a layer no more than about 200 pc thick in the solar neighborhood (Whittet 2003). Not only young massive stars but also dust is concentrated to the spiral arms. Extinction toward the Galactic center (GC) is estimated to be $A_V \sim 30$ mag over the about 8.5 kpc path. Infrared observations enable us to penetrate dust and to investigate the GC region.

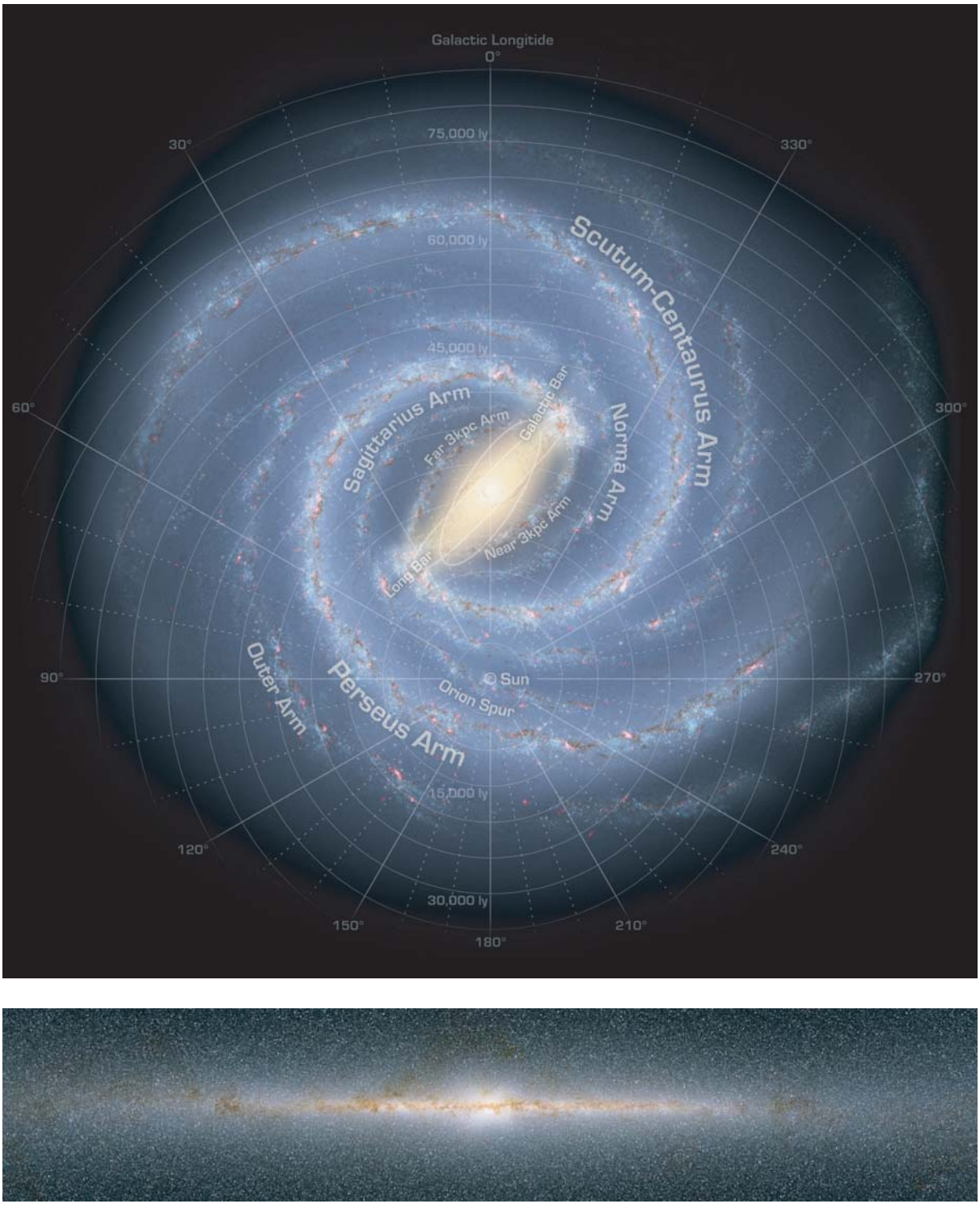

Figure 1.4: *Top*: artist's concept of the Galaxy seen from Galactic north pole (R. Hurt; NASA/JPL-Caltech, http://ipac.jpl.nasa.gov/media_images/ssc2008-10b.jpg). The distance of the Sun from the center of the Galaxy is about 8.5 kpc (Ghez et al. 2008). *Bottom*: NIR view of the Galaxy by 2MASS (J. Carpenter, T. H. Jarrett, & R. Hurt; NASA/IPAC, http://www.ipac.caltech.edu/2mass/gallery/showcase/allsky_stars/enlarged.html).

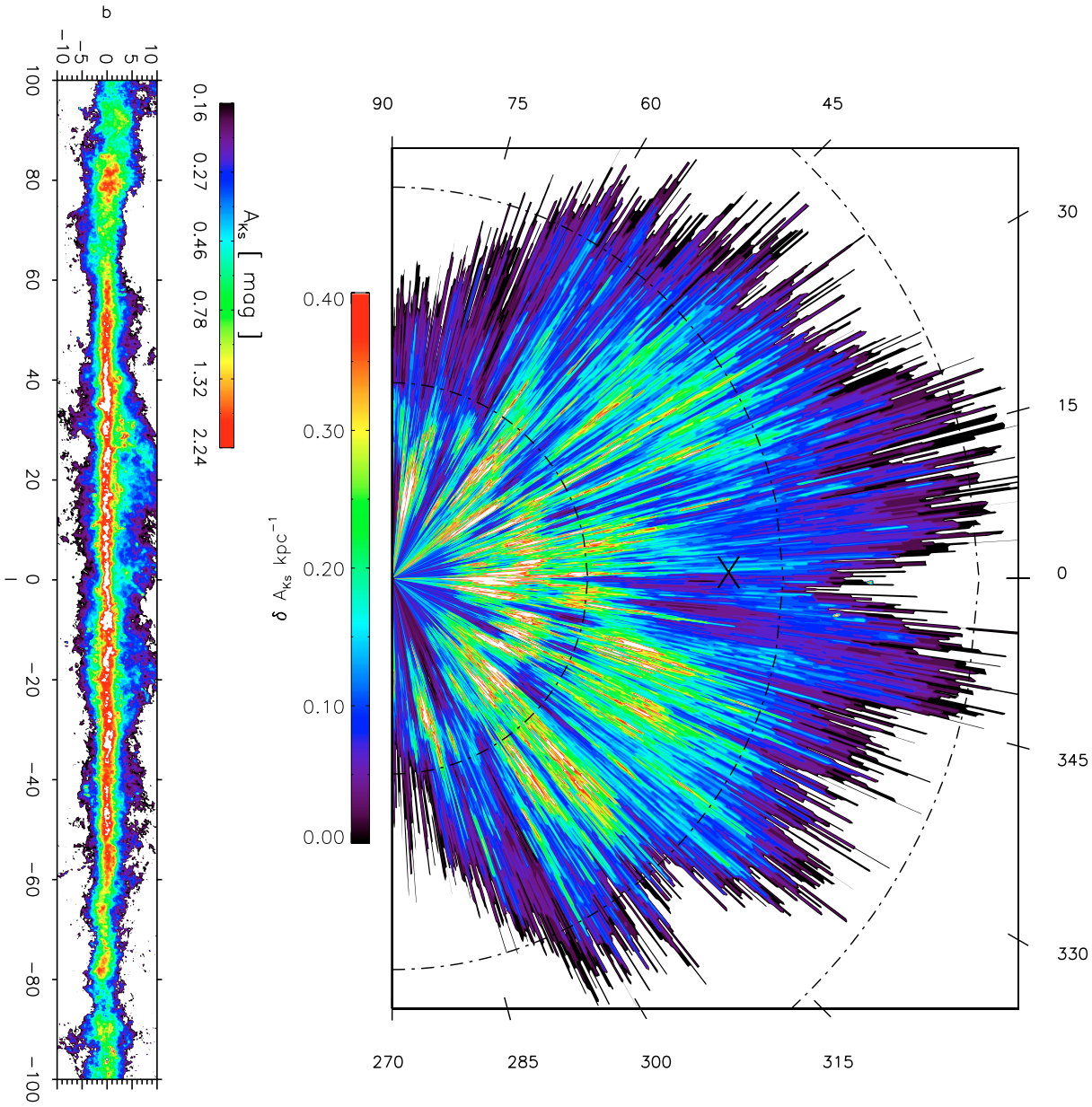

Figure 1.5: *Left*: total extinction integrated along the line-of-sight (Fig. 7 of Marshall et al. 2006). The coordinates are expressed in degrees (l, b). *Right*: location of extincting dust in the Galactic plane ($|b| \leq 0.^{\circ}25$; Fig. 9 of Marshall et al. 2006). The Galactic center, assumed to be at 8.5 kpc from the Sun, is marked with an "X"; the Sun is located in the middle on the left side of the plot. The dotted lines are placed every 5 kpc from the Sun. Ticks on the border indicate Galactic longitude.

The observed polarization of starlight yields the configuration of the magnetic field on the plane-of-the-sky (e.g., Mathewson & Ford 1970; Heiles 2000). In the disk the directions of the $\boldsymbol{E}$-vectors of polarization are predominantly parallel to the Galactic plane, suggesting that the directions of magnetic fields are almost longitudinal (Fig. 1.6). Observations of Faraday rotation of linearly polarized radiation from pulsars and extragalactic radio sources (EGRs) give a measure of the line-of-sight component of the magnetic field, as shown in Figure 1.7 (e.g., Heiles 1996; Han 2009). These observations indicate that the large-scale uniform magnetic field in the Galaxy (the Galactic magnetic field) aligns with the spiral arms in the disk. The strength of the uniform magnetic field is estimated to be $B_u = 2.2$ μG in the solar neighborhood (Heiles 1996).

The $\boldsymbol{E}$-vectors of starlight polarization also show irregular fluctuations, suggesting the existence of a random component of the magnetic field on a small-scale. The random component is caused by the motions of gas in which the magnetic field is frozen arising from turbulence, gravitational contraction of the ISM, expansion of H II regions, and supernova explosions. In the solar neighborhood, the strength of the random component is derived to be $B_r = 3.6$ μG, higher than that of the uniform component of the magnetic field (Heiles 1996).

1.3 This Study

We have conducted a polarimetric imaging survey toward the GC in the NIR bands. The previous NIR polarimetric observations (e.g., Lebofsky et al. 1982; Kobayashi et al. 1983; Bailey et al. 1984) covered only narrow regions around the GC ($\leq 20' \times 20'$). We present for the first time the results of wide field ($\sim 3^\circ \times 2^\circ$) observations.

The scientific purposes of the survey are as follows:

(1) Investigating the magnetic field toward the GC based on the interstellar polarization efficiency and position angles.

(2) Examining the wavelength dependence of interstellar polarization at the NIR wavelengths, which provides information of the polarizing grain properties.

(3) Searching for extended polarized sources toward the GC.

First we describe the details of the instruments, observations, and data reduction and analysis in Chapters 2 and 3. In Chapters 4, 5, and Appendix A, we present the results for (1), (2), and (3). Finally this study is summarized in Chapter 6. Furthermore, we discuss interstellar extinction maps toward the GC in Appendix B.

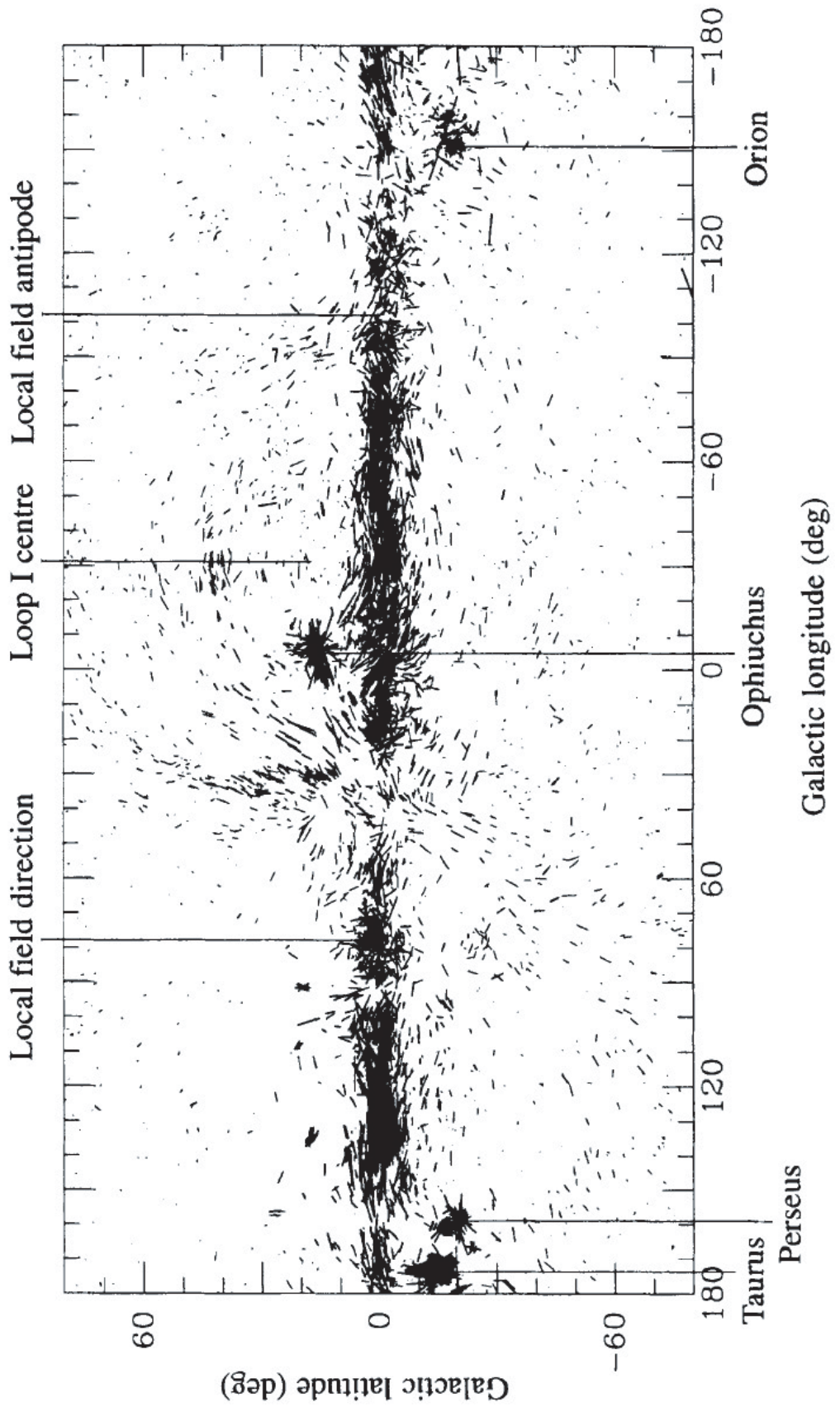

Figure 1.6: Starlight polarization based on a catalogue of 7,503 stars and several additional studies concentrating on the named star-forming regions (Fig. 3 of Zweibel & Heiles 1997). The orientation of each line is along the polarization, which is parallel to the magnetic field direction projected on the plane-of-the-sky. The length of the line indicating the polarization p, for which there are two scales; thin lines have $p < 0.6\%$ and are proportionately four times longer than thick lines.

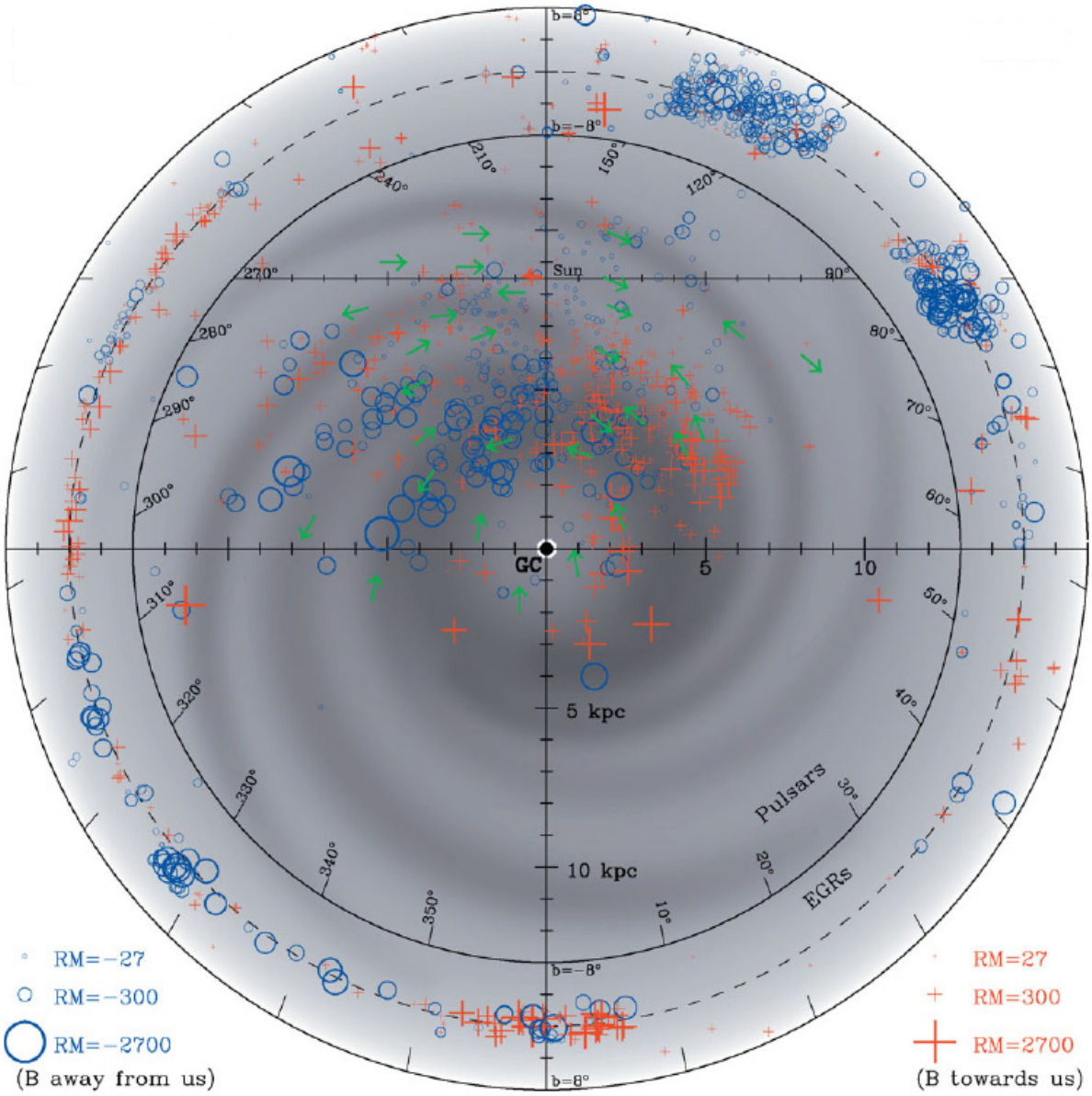

Figure 1.7: The rotation measure (RM) distribution of 736 pulsars with $|b| < 8°$ projected onto the Galactic plane (Fig. 1 of Han 2009). The linear sizes of the symbols are proportional to the square root of the RM values with limits of ± 27 and ± 2700 rad m^{-2}. Positive RMs are shown by plus signs and negative RMs by open circles. The background shows the approximate locations of the spiral arms. RMs of 1285 EGRs of $|b| < 8°$ are displayed in the outskirt ring according to their l and b, with the same convention of RM symbols and limits. The large-scale structure of magnetic fields indicated by arrows was derived from pulsar RMs and comparison of them with RMs of background EGRs.

Bibliography

Bailey, J., Hough, J. H., & Axon, D. J. 1984, MNRAS, 208, 661

Chandrasekhar, S. 1946, ApJ, 103, 351

Davis, L., Jr., & Greenstein, J. L. 1951, ApJ, 114, 206

Dombrovsky, V. A. 1954, Dokl. Akad. Nauk SSSR, 94, 1021

Ghez, A. M., Salim, S., Weinberg, N. N., Lu, J. R., Do, T., Dunn, J. K., Matthews, K., Morris, M. R., Yelda, S., Becklin, E. E., Kremenek, T., Milosavljevic, M., & Naiman, J. 2008, ApJ, 689, 1044

Hall, J. S. 1949, Sci, 109, 166

Heckt, E. 1998, Optics (3rd ed.; Addison Wesley Publishing)

Hiltner, W. A. 1949, Sci, 109, 165

Han, J. L. 2009, in IAU Symp. 259. Cosmic Magnetic Fields: From Planets, to Stars and Galaxies, ed. K. G. Strassmeir, A. G. Kosovichev, & J. E. Beckman (Dordrecht: Kluwer), 455

Heiles, C. 1996, in Polarimetry of the Interstellar Medium, ed. W. G. Roberge & D. C. B. Whittet (San Francisco: ASP), 457

Heiles, C. 2000, AJ, 119, 923

Kobayashi, Y., Okuda, H., Sato, S., Jugaku, J., & Dyck, H. M. 1983, PASJ, 35, 101

Lazarian, A. 2003, J. Quant. Spectrosc. Radiat. Transfer, 79, 881

Lazarian, A. 2007, J. Quant. Spectrosc. Radiat. Transfer, 106, 225

Lebofsky, M. J., Rieke, G. H., Deshpande, M. R., & Kemp, J. C. 1982, ApJ, 263, L672

Marshall, D. J., Robin, A. C., Reyle, C., Schultheis, M., & Picaud, S. 2006, A&A, 453, 635

Martin, P. G. 1974, ApJ, 187, 461

Mathewson, D. S., & Ford, V. L. Mem. R. Astron. Soc., 74, 139

Mayer, C. H., McCullough, T. P., & Sloanaker, R. M. 1957, ApJ, 126, 468

Mie, G. 1908, Ann. Phys., 25, 377

Novick, R., Weisskopf, M. C., Berthelsdorf, R., Linke, R., & Wolff, R. S. 1972, ApJ, 174, 1

Rayleigh, L. 1871, Phil. Mag., 41, 107

Tinbergen, J. 1996, Astronomical Polarimetry (Cambridge, UK: Cambridge University Press)

Weintraub, D. A., Goodman, A. A., & Akeson, R. L. 2000, in Protostars and Planets I V, ed. V. Mannings, A. P. Boss, & S. S. Russell (Tucson: University of Arizona Press), 247

Whittet, D. C. B. 2003, Dust in the Galactic Environment (2nd ed; Bristol: Institute of Physics Publishing)

Zweibel, E. G., & Heiles, C. 1997, Nature, 385, 131

Chapter 2

Near-Infrared Polarimetric Survey toward the Galactic Center

We have carried out a polarimetric imaging survey toward the GC in the NIR bands on IRSF (InfraRed Survey Facility). In this chapter, we describe the details of IRSF and the observations for the survey.

2.1 IRSF

IRSF has an 1.4 m telescope, the NIR camera SIRIUS (Simultaneous three-color InfraRed Imager for Unbiased Survey), and its polarimeter SIRPOL (Fig. 2.1). IRSF is located at the South African Astronomical Observatory (SAAO) in Sutherland.

2.1.1 1.4 m Telescope

The telescope is a classical Cassegrain design with an 1.4 m primary mirror on an alt-azimuth mount. It was constructed by Nagoya University in collaboration with the Nishimura telescope company in Japan. The pointing accuracy was measured to be about $3''$ (RMS) for the entire sky, and the tracking accuracy is about $0\farcs3$ per 30 s exposure (Kato 2001). The specifications of the telescope are listed in Table 2.1.

2.1.2 SIRIUS

SIRIUS is a simultaneous three-channel NIR camera developed by Nagoya University and the National Astronomical Observatory of Japan (NAOJ). It is equipped with three 1024 pixel × 1024 pixel HgCdTe Astronomical Wide Area Infrared Imaging (HAWAII) arrays. This enables simultaneous observations in the J (central wavelength $\lambda_J = 1.25$ μm), H ($\lambda_H = 1.63$ μm), and K_S ($\lambda_{K_S} = 2.14$ μm) bands by splitting the beam into the three wavelengths with two dichroic mirrors (Fig. 2.2). The pixel scale of the arrays is $0\farcs45$ pixel^{-1}, yielding a field of view of $7\farcm7 \times 7\farcm7$. The specifications of SIRIUS are listed in Table 2.1. For more details about the camera, refer to Nagashima et al. (1999) and Nagayama et al. (2003).

Figure 2.1: 1.4 m telescope and the SIRIUS camera. The camera is installed at the Cassegrain focus of the telescope.

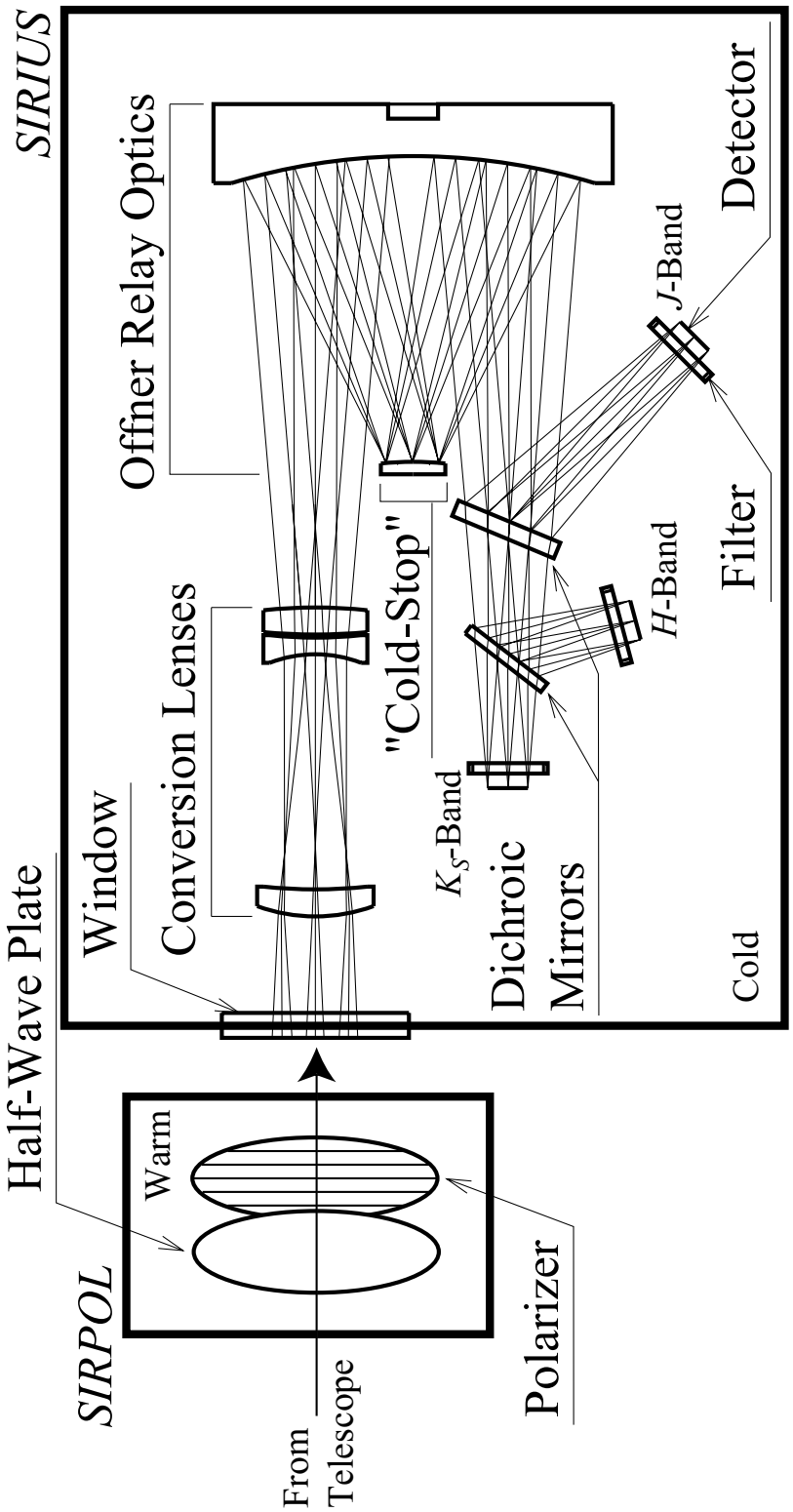

Figure 2.2: The optical layout of the SIRIUS camera and polarimeter SIRPOL.

Table 2.1: Specifications of the Instruments and Site

telescope	
design	classical Cassegrain
effective aperture of primary mirror	1395 mm
effective aperture of secondary mirror	382 mm
mount	alt-azimuth
pointing accuracy	$\sim 3''$ (RMS)
tracking accuracy	$\sim 0''.3$ per 30 s exposure
SIRIUS	
detectors	1024 × 1024 HAWAII array × 3
filters	J, H, K_S
central wavelengths	1.25 μm (J), 1.63 μm (H), 2.14 μm (K_S)
pixel scale	$0''.45$
field of view	$7'.7 \times 7'.7$
SIRPOL	
polarization efficiency	95.5% (J), 96.3% (H), 98.5% (K_S)
correction angle	105°
site	
location	20°48′38″ E, 32°22′46″ S
altitude	1761 m
sky background values [mag arcsec^{-2}]	15.0−15.5 (J), 13.2−14.4 (H), 12.0−13.2 (K_S)

2.1.3 SIRPOL

SIRPOL is a single-beam polarimeter for the SIRIUS camera. It consists of an achromatic (1.0−2.5 μm) half-wave plate, its rotator, and a wire grid polarizer. The polarimeter is set up upstream of SIRIUS at a room temperature (Fig. 2.2). By the observations of field stars, the polarization efficiency of the half-wave plate and polarizer was measured to be 95.5%, 96.3%, and 98.5% in the J, H, and K_S bands, respectively. The correction angle of the polarimeter (105°) was also determined from the observations of infrared reflection nebulae with known centrosymmetric patterns of polarization vectors. The specifications of SIRPOL are listed in Table 2.1. For more details about the polarimeter, refer to Kandori et al. (2006).

2.1.4 Site

Sutherland is about 370 km north-east of Cape Town in the Republic of South Africa (20°48′38″ E, 32°22′46″ S, and 1761 m above the sea level). The typical sky background values on the site are 15.0−15.5, 13.2−14.4, 12.0−13.2 mag / arcsec^2 in the J, H, and K_S bands, respectively (Nagayama 2004). The specifications of the site are listed in Table 2.1.

2.2 Observations

The NIR polarimetric imaging survey toward the GC is planned to cover the region of 4° (Galactic longitude) × 2° (Galactic latitude) centered on the GC (Fig. 2.3). From 2006 to 2009, we have observed 613 fields, and the total area covered is about 7.6 deg^2. The grids of the survey area are along right ascension and declination (J2000) and same in the photometric survey of Nishiyama (2005), which are listed in Table 2.2. We obtained 10 dithered frames with 10 s exposures at four wave plate angles (in the order of 0°, 45°, 22.°5, and 67.°5), resulting in a total exposure time of 100 s per wave plate angle for each field. Our observations were carried out under stable conditions of the sky. The average seeing sizes were 1.″3, 1.″2, and 1.″1 (FWHM) in the J, H, and K_S bands, respectively (§3.3.1). To make median sky frames we observed two sparse stellar fields. Twilight flat frames were obtained before and after the observations. Dark frames were obtained at the end of the nights. For a check of our polarimetry, the polarimetric standard star R CrA No. 88 (Whittet et al. 1992) was observed 15 times through the observing runs. We performed 1.6 s or 2 s exposures at each wave plate angle at 10 dithered positions. The scheme of the observations is listed in Table 2.3.

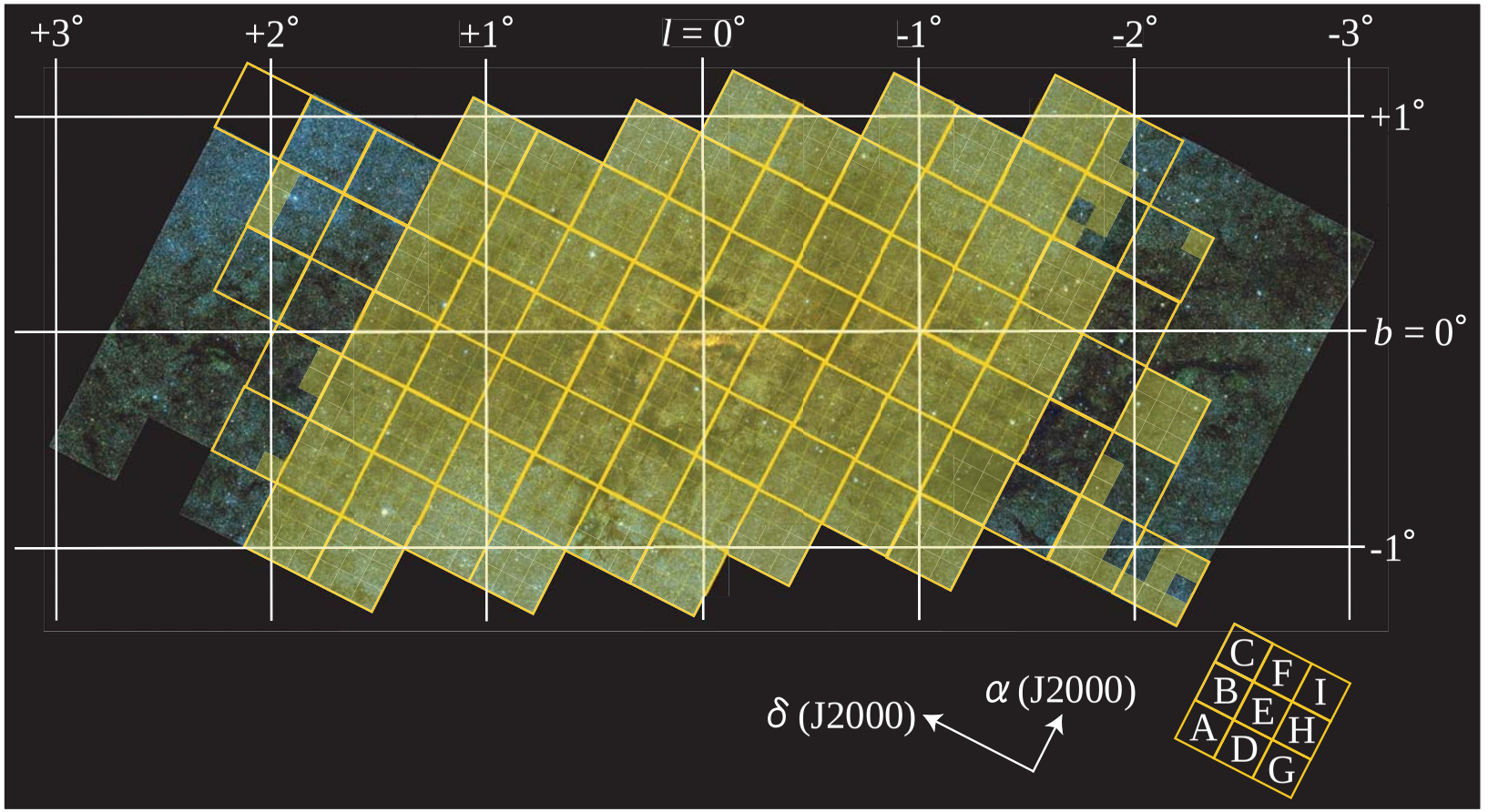

Figure 2.3: The area of the survey superimposed on the JHK_S composite image of the GC (Fig. 1.5 of Nishiyama 2005). Each open square denotes 3 × 3 fields, which are designated A to I as shown in the lower right of the figure. Filled squares indicate observed fields.

Table 2.2: Grids of the Survey Area

region	α (J2000)[a]	δ (J2000)[b]	l[c]	b[d]
GC1737−3000	17:37:56.5	−30:00:28.0	−1.7924	0.8532
GC1737−3020	17:37:56.5	−30:20:28.0	−2.0740	0.6747
GC1739−2920	17:39:30.0	−29:20:28.0	−1.0479	0.9227
GC1739−2940	17:39:30.0	−29:40:28.0	−1.3301	0.7453
GC1739−3000	17:39:30.0	−30:00:28.0	−1.6124	0.5679
GC1739−3020	17:39:30.0	−30:20:28.0	−1.8945	0.3904
GC1739−3040	17:39:30.0	−30:40:28.0	−2.1767	0.2130
GC1741−2840	17:41:03.5	−28:40:28.0	−0.3020	0.9878
GC1741−2900	17:41:03.5	−29:00:28.0	−0.5848	0.8113
GC1741−2920	17:41:03.5	−29:20:28.0	−0.8676	0.6349
GC1741−2940	17:41:03.5	−29:40:28.0	−1.1505	0.4584
GC1741−3000	17:41:03.5	−30:00:28.0	−1.4333	0.2820
GC1741−3020	17:41:03.5	−30:20:28.0	−1.7160	0.1055
GC1741−3040	17:41:03.5	−30:40:28.0	−1.9988	−0.0710
GC1742−2820	17:42:36.0	−28:20:28.0	0.1600	0.8760
GC1742−2840	17:42:36.0	−28:40:28.0	−0.1235	0.7005
GC1742−2900	17:42:36.0	−29:00:28.0	−0.4069	0.5251
GC1742−2920	17:42:36.0	−29:20:28.0	−0.6903	0.3496
GC1742−2940	17:42:36.0	−29:40:28.0	−0.9737	0.1740
GC1742−3000	17:42:36.0	−30:00:28.0	−1.2570	−0.0015
GC1742−3020	17:42:36.0	−30:20:28.0	−1.5404	−0.1770
GC1742−3040	17:42:36.0	−30:40:28.0	−1.8238	−0.3525
GC1742−3100	17:42:36.0	−31:00:28.0	−2.1072	−0.5280
GC1744−2740	17:44:08.5	−27:40:28.0	0.9061	0.9364
GC1744−2800	17:44:08.5	−28:00:28.0	0.6221	0.7619
GC1744−2820	17:44:08.5	−28:20:28.0	0.3381	0.5873
GC1744−2840	17:44:08.5	−28:40:28.0	0.0541	0.4128
GC1744−2900	17:44:08.5	−29:00:28.0	−0.2299	0.2382
GC1744−2920	17:44:08.5	−29:20:28.0	−0.5138	0.0636
GC1744−2940	17:44:08.5	−29:40:28.0	−0.7978	−0.1109
GC1744−3000	17:44:08.5	−30:00:28.0	−1.0818	−0.2855
GC1744−3020	17:44:08.5	−30:20:28.0	−1.3658	−0.4601
GC1744−3040	17:44:08.5	−30:40:28.0	−1.6497	−0.6346
GC1744−3100	17:44:08.5	−31:00:28.0	−1.9338	−0.8092

Table 2.2: *Continued*

region	α (J2000)[a]	δ (J2000)[b]	l[c]	b[d]
GC1745−2640	17:45:40.0	−26:40:28.0	1.9362	1.1692
GC1745−2700	17:45:40.0	−27:00:28.0	1.6516	0.9956
GC1745−2720	17:45:40.0	−27:20:28.0	1.3670	0.8220
GC1745−2740	17:45:40.0	−27:40:28.0	1.0824	0.6484
GC1745−2800	17:45:40.0	−28:00:28.0	0.7979	0.4748
GC1745−2820	17:45:40.0	−28:20:28.0	0.5133	0.3012
GC1745−2840	17:45:40.0	−28:40:28.0	0.2288	0.1275
GC1745−2900	17:45:40.0	−29:00:28.0	−0.0557	−0.0461
GC1745−2920	17:45:40.0	−29:20:28.0	−0.3403	−0.2198
GC1745−2940	17:45:40.0	−29:40:28.0	−0.6248	−0.3934
GC1745−3000	17:45:40.0	−30:00:28.0	−0.9093	−0.5670
GC1745−3020	17:45:40.0	−30:20:28.0	−1.1939	−0.7407
GC1745−3040	17:45:40.0	−30:40:28.0	−1.4785	−0.9143
GC1745−3100	17:45:40.0	−31:00:28.0	−1.7631	−1.0878
GC1745−3120	17:45:40.0	−31:20:28.0	−2.0478	−1.2614
GC1747−2700	17:47:11.5	−27:00:28.0	1.8281	0.7054
GC1747−2720	17:47:11.5	−27:20:28.0	1.5429	0.5327
GC1747−2740	17:47:11.5	−27:40:28.0	1.2578	0.3599
GC1747−2800	17:47:11.5	−28:00:28.0	0.9728	0.1872
GC1747−2820	17:47:11.5	−28:20:28.0	0.6877	0.0145
GC1747−2840	17:47:11.5	−28:40:28.0	0.4026	−0.1583
GC1747−2900	17:47:11.5	−29:00:28.0	0.1175	−0.3310
GC1747−2920	17:47:11.5	−29:20:28.0	−0.1676	−0.5037
GC1747−2940	17:47:11.5	−29:40:28.0	−0.4527	−0.6765
GC1747−3000	17:47:11.5	−30:00:28.0	−0.7378	−0.8492
GC1747−3020	17:47:11.5	−30:20:28.0	−1.0230	−1.0218
GC1748−2700	17:48:42.0	−27:00:28.0	2.0017	0.4178
GC1748−2720	17:48:42.0	−27:20:28.0	1.7161	0.2459
GC1748−2740	17:48:42.0	−27:40:28.0	1.4305	0.0741
GC1748−2800	17:48:42.0	−28:00:28.0	1.1448	−0.0978
GC1748−2820	17:48:42.0	−28:20:28.0	0.8592	−0.2697
GC1748−2840	17:48:42.0	−28:40:28.0	0.5736	−0.4415
GC1748−2900	17:48:42.0	−29:00:28.0	0.2880	−0.6133
GC1748−2920	17:48:42.0	−29:20:28.0	0.0023	−0.7852
GC1748−2940	17:48:42.0	−29:40:28.0	−0.2834	−0.9570

Table 2.2: *Continued*

region	α (J2000)[a]	δ (J2000)[b]	l[c]	b[d]
GC1750−2720	17:50:12.5	−27:20:28.0	1.8883	−0.0414
GC1750−2740	17:50:12.5	−27:40:28.0	1.6022	−0.2123
GC1750−2800	17:50:12.5	−28:00:28.0	1.3160	−0.3833
GC1750−2820	17:50:12.5	−28:20:28.0	1.0299	−0.5543
GC1750−2840	17:50:12.5	−28:40:28.0	0.7437	−0.7253
GC1750−2900	17:50:12.5	−29:00:28.0	0.4575	−0.8962
GC1750−2920	17:50:12.5	−29:20:28.0	0.1713	−1.0671
GC1751−2720	17:51:42.5	−27:20:28.0	2.0588	−0.3276
GC1751−2740	17:51:42.5	−27:40:28.0	1.7721	−0.4977
GC1751−2800	17:51:42.5	−28:00:28.0	1.4854	−0.6678
GC1751−2820	17:51:42.5	−28:20:28.0	1.1987	−0.8379
GC1751−2840	17:51:42.5	−28:40:28.0	0.9120	−1.0080
GC1753−2740	17:53:12.5	−27:40:28.0	1.9412	−0.7835
GC1753−2800	17:53:12.5	−28:00:28.0	1.6540	−0.9528

[a,b] Units of right ascension are hours, minutes, and seconds, and units of declination are degrees, arcminutes, and arcseconds.
[c,d] Units of Galactic longitude and latitude are degrees.

Table 2.3: Scheme of the Observations

Galactic Center	
central coordinates (J2000)	$\alpha = 17^{\rm h}45^{\rm m}40\overset{\rm s}{.}0$, $\delta = -29°00'28\overset{''}{.}0$
coverage	7.6 deg^2 (613 fields)
exposure time	10 s per a frame
dithering	10 times on the circle with a radius of 20″
sky	
central coordinates (J2000)	$\alpha = 17^{\rm h}11^{\rm m}24\overset{\rm s}{.}7$, $\delta = -27°27'20\overset{''}{.}0$, or $\alpha = 18^{\rm h}47^{\rm m}45\overset{\rm s}{.}7$, $\delta = -30°56'20\overset{''}{.}0$
exposure time	10 s per a frame
dithering	10 times on the circle with a radius of 60″
R CrA No. 88	
coordinates (J2000)	$\alpha = 19^{\rm h}06^{\rm m}09\overset{\rm s}{.}7$, $\delta = -37°18'09\overset{''}{.}8$
exposure time	1.6 s or 2 s per a frame
dithering	10 times on the circle with a radius of 20″
atmospheric condition	
average seeing sizes (FWHM)	$1\overset{''}{.}3$ (J), $1\overset{''}{.}2$ (H), $1\overset{''}{.}1$ (K_S)

Bibliography

Kandori, R., Kusakabe, N., Tamura, M., Nakajima, Y., Nagayama, T., Nagashima, C., Hashimoto, J., Hough, J., Sato, S., Nagata, T., Ishihara, A., Lucas, P., & Fukagawa, M. 2006, Proc. SPIE, 6269, 159

Kato, D., 2001, Master's thesis, Nagoya University

Nagashima, C., Nagayama, T., Nakajima, Y., Tamura, M., Sugitani, K., Nagata, T., Hirao, T., Nakaya, H., Yanagisawa, K., & Sato, S. 1999, in Star Formation 1999, ed. T. Nakamoto (Nobeyama: Nobeyama Radio Obs.), 397

Nagayama, T., Nagashima, C., Nakajima, Y., Nagata, T., Sato, S., Nakaya, H., Yamamuro, T., Sugitani, K., & Tamura, M. 2003, Proc. SPIE, 4841, 51

Nagayama, T., 2004, Ph.D. thesis, Nagoya University

Nishiyama, S., 2005, Ph.D. thesis, Nagoya University

Whittet, D. C. B., Martin, P. G., Hough, J. H., Rouse, M. F., Bailey, J. A., & Axon, D. J. 1992, ApJ, 386, 562

Chapter 3

Data Reduction and Analysis

We have carried out data reduction and data analysis for point sources and extended sources. From among all the survey data, we analyzed the data of 459 fields, which have an area of about 5.7 deg^2 (Fig. 3.1). In this chapter, we describe the details of the data reduction and analysis.

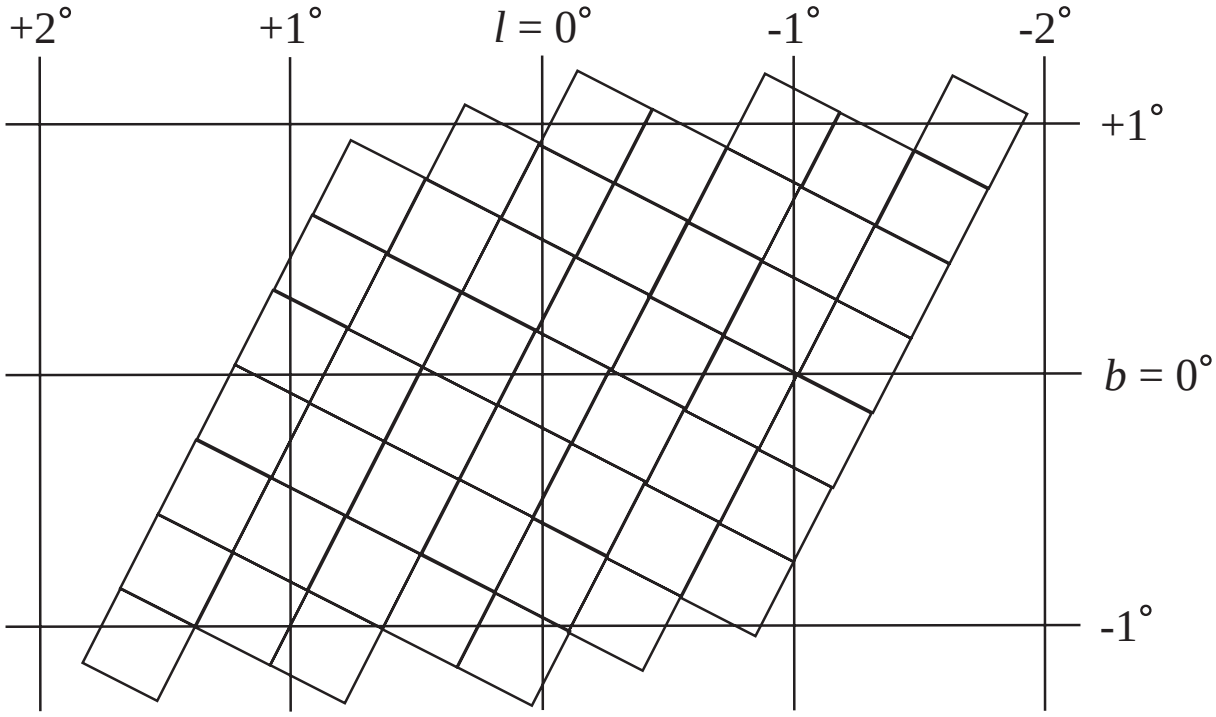

Figure 3.1: The area in which data were analyzed. Each square denotes 3 × 3 fields with a size of 20′ × 20′.

3.1 Data Reduction

We conducted data reduction using the SIRPOL pipeline package[1]. The standard procedures of NIR array image reduction, including dark-current subtraction, flat-fielding, sky subtraction, and frame combination were applied. After subtraction of an averaged dark frame, each frame was divided by a normalized flat frame. Then the thermal emission pattern, the fringe pattern due to OH emission, and the reset-anomaly slope pattern of the HAWAII arrays were subtracted from each frame with a median sky frame. We obtained images by combining 10 frames for each wave plate angle. For Stokes I images, we summed frames for wave plate angles at 0° and 45°, 22.°5 and 67.°5, and averaged 2 summed frames, then combined 10 averaged frames. We also obtained instrumental Stokes Q or U images by subtracting frames for wave plate angle at 45° or 67.°5 from those at 0° or 22.°5 and combining 10 subtracted frames.

3.2 Data Analysis for Point Sources

3.2.1 Photometry

Photometry of point sources was performed using the DAOPHOT package in the IRAF (Image Reduction and Analysis Facility)[2] software package. From PSF-fitting photometry of Stokes I images we obtained positions and magnitudes of point sources. The procedures of the photometry are as follows:

(1) Measure mode and standard deviation (σ) of sky background level.

(2) Detect bright point sources with 10σ detection threshold above the mode of sky background level using the DAOFIND task.

(3) Measure seeing sizes (FWHM) of the bright point sources detected in (2) using the PSFMEASURE task.

(4) Detect point sources with 5σ detection threshold above the mode of sky background level.

(5) Perform aperture photometry for the point sources detected in (4) using the PHOT task.

(6) Select bright and isolated point sources as PSF stars using the PSTSELECT task.

(7) Compute PSF model from the PSF stars selected in (6)[3].

[1]The SIRPOL pipeline package was developed by Dr. Y. Nakajima.

[2]IRAF is distributed by the National Optical Astronomy Observatories, which are operated by the Association of Universities for Research in Astronomy, Inc., under cooperative agreement with the National Science Foundation.

[3]Number of the PSF stars were typically 20−60, 50−90, and 60−90 in the J, H, and K_S bands.

(8) Perform PSF-fitting photometry for the point sources detected in (4), and subtract the fitted point sources from the original image using the ALLSTAR task.

(9) Detect faint point sources on the image created in (8) with 5σ detection threshold above the mode of sky background level.

(10) Perform aperture photometry and PSF-fitting photometry for the faint point sources detected in (9).

(11) Repeat (9) and (10).

(12) Subtract all the point sources except for the PSF stars from the original image using the SUBSTAR task.

(13) Recompute PSF model from the PSF stars on the image created in (12)[3].

(14) Repeat (8) to (12) using the PSF model recomputed in (13), and recompute PSF model[3].

(15) Perform PSF-fitting photometry in the same manner as (8) to (11) using the final PSF model recomputed in (14).

(16) Perform aperture photometry for the PSF stars.

(17) Apply aperture correction calculated by comparing magnitudes of the PSF stars obtained in (15) and (16).

For photometric calibration, we compared magnitudes for the detected sources with those for the 2MASS Point Source Catalog sources in the observed field (Skrutskie et al. 2006)[4]. In this comparison magnitude transformations from the 2MASS system to the IRSF system were applied using the following equations:

$$J_{\rm IRSF} = J_{\rm 2MASS} - 0.045 \times (J-H)_{\rm 2MASS} - 0.001,$$

$$H_{\rm IRSF} = H_{\rm 2MASS} + 0.025 \times (H-K_S)_{\rm 2MASS} + 0.010,$$

$$K_{S\,\rm IRSF} = K_{S\,\rm 2MASS} + 0.036 \times (H-K_S)_{\rm 2MASS} + 0.003,$$

where $J_{\rm IRSF}$, $H_{\rm IRSF}$, and $K_{S\,\rm IRSF}$ are magnitudes in the IRSF system, and $J_{\rm 2MASS}$, $H_{\rm 2MASS}$, and $K_{S\,\rm 2MASS}$ and $(J-H)_{\rm 2MASS}$ and $(H-K_S)_{\rm 2MASS}$ are magnitudes and colors in the 2MASS system (Y. Nakajima 2007, private communication).

[4]This thesis makes use of data products from the Two Micron All Sky Survey, which is a joint project of the University of Massachusetts and the Infrared Processing and Analysis Center/California Institute of Technology, funded by the National Aeronautics and Space Administration and the National Science Foundation

3.2.2 Polarimetry

Using the APPHOT package in IRAF, we performed aperture photometry of combined images for each wave plate angle to obtain flux of point sources. Aperture sizes we applied were 1.5 times as large as sizes of seeing (FWHM) measured on Stokes I images. The procedures of the photometry are as follows:

(1) Measure mode and standard deviation (σ) of sky background level.

(2) Detect point sources with 5σ detection threshold above the mode of sky background level.

(3) Perform aperture photometry for the point sources detected in (2) using the PHOT task.

Based on flux of point sources for each wave plate angle (I_0, $I_{22.5}$, I_{45}, and $I_{67.5}$), we calculated Stokes parameters I, Q, U, and their statistical errors δI, $\delta Q_{\rm sta}$, $\delta U_{\rm sta}$ (calculated from noise of signal, sky background, dark current, and readout) following the equations:

$$
\begin{aligned}
I &= \frac{I_0 + I_{45} + I_{22.5} + I_{67.5}}{2} \quad [\mathrm{ADU}], \\
\delta I &= \frac{\sqrt{{\delta I_0}^2 + {\delta I_{45}}^2 + {\delta I_{22.5}}^2 + {\delta I_{67.5}}^2}}{2} \quad [\mathrm{ADU}], \\
Q_{\rm ins} &= I_0 - I_{45} \quad [\mathrm{ADU}], \\
\delta Q_{\rm ins} &= \sqrt{{\delta I_0}^2 + {\delta I_{45}}^2} \quad [\mathrm{ADU}], \\
U_{\rm ins} &= I_{22.5} - I_{67.5} \quad [\mathrm{ADU}], \\
\delta U_{\rm ins} &= \sqrt{{\delta I_{22.5}}^2 + {\delta I_{67.5}}^2} \quad [\mathrm{ADU}], \\
Q &= \frac{Q_{\rm ins} \times \cos(2\alpha) - U_{\rm ins} \times \sin(2\alpha)}{p_{\rm eff}/100} \quad [\mathrm{ADU}], \\
\delta Q_{\rm sta} &= \frac{\sqrt{{\delta Q_{\rm ins}}^2 \times \cos^2(2\alpha) + {\delta U_{\rm ins}}^2 \times \sin^2(2\alpha)}}{p_{\rm eff}/100} \quad [\mathrm{ADU}], \\
U &= \frac{Q_{\rm ins} \times \sin(2\alpha) + U_{\rm ins} \times \cos(2\alpha)}{p_{\rm eff}/100} \quad [\mathrm{ADU}], \\
\delta U_{\rm sta} &= \frac{\sqrt{{\delta Q_{\rm ins}}^2 \times \sin^2(2\alpha) + {\delta U_{\rm ins}}^2 \times \cos^2(2\alpha)}}{p_{\rm eff}/100} \quad [\mathrm{ADU}],
\end{aligned}
$$

where $Q_{\rm ins}$ and $U_{\rm ins}$ are instrumental Stokes parameters Q and U, and $\delta Q_{\rm ins}$ and $\delta U_{\rm ins}$ are their statistical errors. Q, U, $\delta Q_{\rm sta}$, and $\delta U_{\rm sta}$ were calibrated for the correction angle (α = 105°) and polarization efficiency ($p_{\rm eff}$ = 95.5%, 96.3%, and 98.5% in the J, H, and K_S bands) of the wave plate and polarizer (Kandori et al. 2006).

Q, U also have systematic errors originating from change of atmospheric conditions (seeing and transparency of atmosphere) at each wave plate angle for each field. To estimate these systematic errors we have made a comparison of normalized Stokes parameters Q/I and U/I of the same sources in overlapping regions between adjacent fields. We defined the same sources as the sources having closest positions within 1″. Using the point sources whose statistical errors of Q/I and U/I were less than 1%, average differences of Q/I and U/I were calculated in each overlapping region (Fig. 3.2). The means of the average differences of Q/I and U/I in overlapping regions were 0.33% and 0.35% in the J band, 0.26% and 0.27% in the H band, and 0.25% and 0.26% in the K_S band. We assigned these values to typical systematic errors of Q/I and U/I, and calculated errors of Q and U (δQ and δU) by combining the estimated systematic errors ($\delta Q_{\rm sys}$ and $\delta U_{\rm sys}$) with the statistical errors ($\delta Q_{\rm sta}$ and $\delta U_{\rm sta}$) following the equations:

$$\delta Q = \sqrt{{\delta Q_{\rm sta}}^2 + {\delta Q_{\rm sys}}^2} \quad [\rm ADU],$$

$$\delta U = \sqrt{{\delta U_{\rm sta}}^2 + {\delta U_{\rm sys}}^2} \quad [\rm ADU].$$

Then observed degree of polarization $p_{\rm obs}$, position angle θ, and their errors δp and $\delta\theta$ were derived by the equations:

$$p_{\rm obs} = \frac{\sqrt{Q^2+U^2}}{I} \times 100 \quad [\%],$$

$$\delta p = \sqrt{\frac{Q^2\times\delta Q^2 + U^2\times\delta U^2}{(p_{\rm obs}/100\times I^2)^2} + \left(\frac{p_{\rm obs}}{100}\times\frac{\delta I}{I}\right)^2} \times 100 \quad [\%],$$

$$\theta = \frac{1}{2}\arctan\frac{U}{Q} \quad [^\circ],$$

$$\delta\theta = \frac{\sqrt{U^2\times\delta Q^2 + Q^2\times\delta U^2}}{Q^2+U^2} \times \frac{180}{2\pi} \quad [^\circ].$$

θ is defined as the angle between the $\boldsymbol{E}$-vector of polarization and the direction of north celestial pole and increasing to the east ($0^\circ \le \theta < 180^\circ$ or $-90^\circ \le \theta < 90^\circ$). To correct noise biasing we calculated degree of polarization p using the following formula:

$$p = \sqrt{{p_{\rm obs}}^2 - \delta p^2} \quad [\%]$$

(Wardle & Kronberg 1974; Clarke & Stewart 1986). We regarded point sources with $p_{\rm obs} \le \delta p$ as unpolarized ($p = 0$) sources.

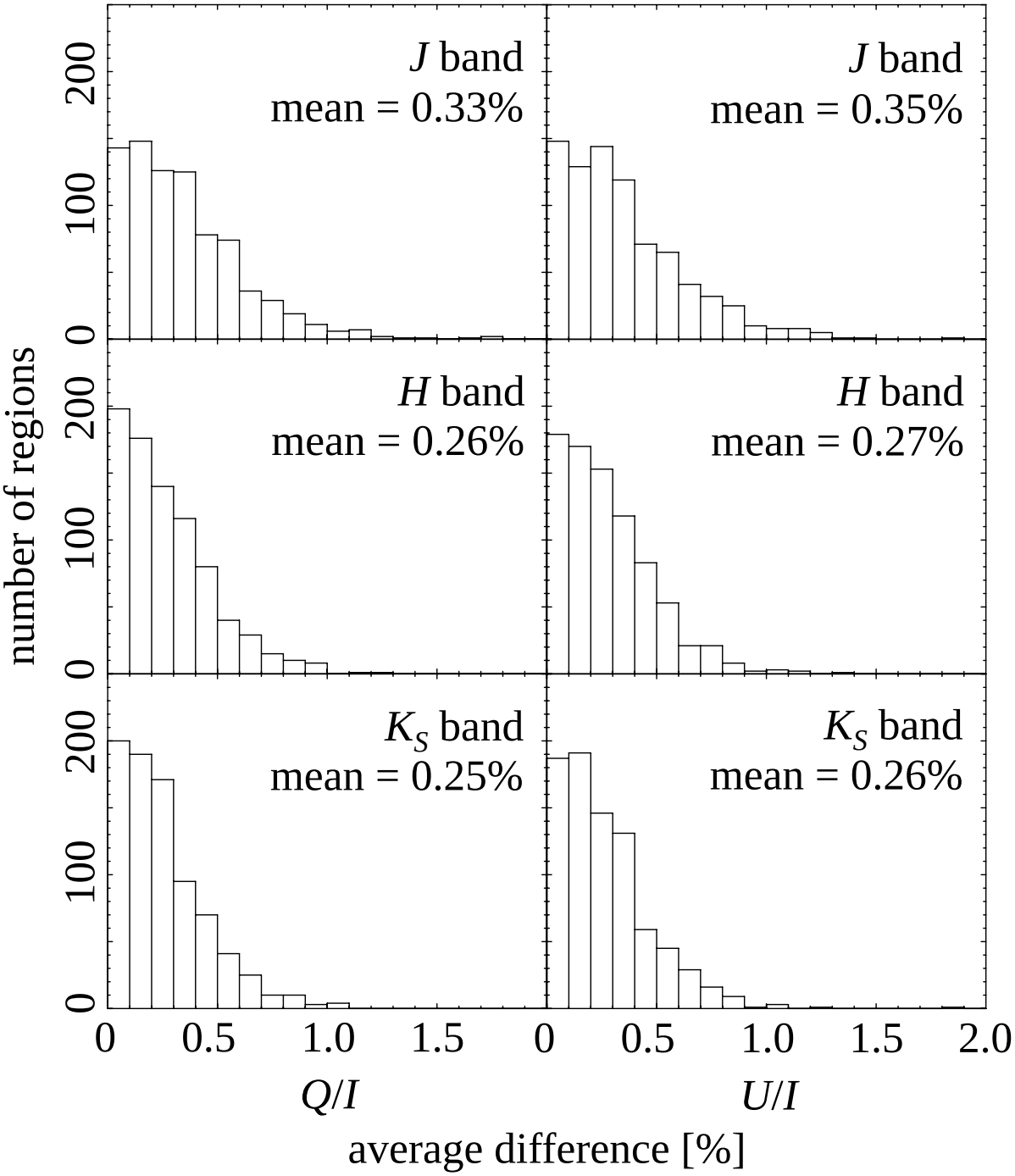

Figure 3.2: Histograms of average differences of normalized Stokes parameters Q/I $(left)$ and U/I $(right)$ in the J (top), H $(middle)$, and K_S $(bottom)$ bands based on the comparison of the same sources in overlapping regions between adjacent fields. The means of the average differences of Q/I and U/I in overlapping regions are shown at the upper right of the panels.

3.2.3 Astrometry

We related pixel coordinates to celestial coordinates by referencing the 2MASS Point Source Catalog using the OPM software[5]. Then positions of point sources on image coordinate system were converted to those on celestial coordinate systems. In the point source catalog (§3.2.4), the positions of point sources are represented by the equatorial coordinates.

3.2.4 Catalog

Point sources in each band were matched and merged into a list of point sources for each field. We first matched and merged point sources in the K_S and H bands, then those in the J band via positional association. A match was defined as the closest counterpart within an $1''$ radius. Position in the point source list is that at the longest wavelength at which a source is detected. Finally we united lists of point sources for each field into a point source catalog. Duplicative data for the same sources in overlapping regions between adjacent fields were included in the catalog. For a same source whose magnitude difference are less than 0.5 mag, duplicative data whichever was detected in less bands or measured with larger errors in polarization degree and position angle, was excluded from the final point source catalog.

There are a total of 3,539,087 point sources in the catalog; 1,536,017, 2,979,994, and 3,190,511 point sources are detected in the J, H, and K_S bands, respectively. A portion of the point source catalog is listed in Table 3.1. The columns of the catalog are as follows:

Column (1): ID — Identifier, which comes from α and δ.
Column (2): α — Right ascension in J2000.
Column (3): δ — Declination in J2000.
Column (4): I_J — Stokes I in the J band.
Column (5): δI_J — Error of Stokes I in the J band.
Column (6): Q_J — Stokes Q in the J band.
Column (7): δQ_J — Error of Stokes Q in the J band.
Column (8): U_J — Stokes U in the J band.
Column (9): δU_J — Error of Stokes U in the J band.
Column (10): p_J — Degree of polarization in the J band.
Column (11): δp_J — Error of degree of polarization in the J band.
Column (12): θ_J — Position angle in the J band.
Column (13): $\delta\theta_J$ — Error of position angle in the J band.
Column (14): J — J magnitude.
Column (15): δJ — Error of J magnitude.
Column (16): X_J — X of pixel coordinates in the J band.
Column (17): Y_J — Y of pixel coordinates in the J band.

[5]The OPM software is compiled by Dr. N. Matsunaga and based on the Optimistic Pattern Matching algorithm proposed by Tabur (2007).

Column (18): I_H — Stokes I in the H band.
Column (19): δI_H — Error of Stokes I in the H band.
Column (20): Q_H — Stokes Q in the H band.
Column (21): δQ_H — Error of Stokes Q in the H band.
Column (22): U_H — Stokes U in the H band.
Column (23): δU_H — Error of Stokes U in the H band.
Column (24): p_H — Degree of polarization in the H band.
Column (25): δp_H — Error of degree of polarization in the H band.
Column (26): θ_H — Position angle in the H band.
Column (27): $\delta\theta_H$ — Error of position angle in the H band.
Column (28): H — H magnitude.
Column (29): δH — Error of H magnitude.
Column (30): X_H — X of pixel coordinates in the H band.
Column (31): Y_H — Y of pixel coordinates in the H band.
Column (32): I_{K_S} — Stokes I in the K_S band.
Column (33): δI_{K_S} — Error of Stokes I in the K_S band.
Column (34): Q_{K_S} — Stokes Q in the K_S band.
Column (35): δQ_{K_S} — Error of Stokes Q in the K_S band.
Column (36): U_{K_S} — Stokes U in the K_S band.
Column (37): δU_{K_S} — Error of Stokes U in the K_S band.
Column (38): p_{K_S} — Degree of polarization in the K_S band.
Column (39): δp_{K_S} — Error of degree of polarization in the K_S band.
Column (40): θ_{K_S} — Position angle in the K_S band.
Column (41): $\delta\theta_{K_S}$ — Error of position angle in the K_S band.
Column (42): K_S — K_S magnitude.
Column (43): δK_S — Error of K_S magnitude.
Column (44): X_{K_S} — X of pixel coordinates in the K_S band.
Column (45): Y_{K_S} — Y of pixel coordinates in the K_S band.
Column (46): Field — Field in which a source was detected.
The parameters in each band are set to "null" when a source is not detected in the band.

Table 3.1: Point Source Catalog

ID	α (J2000)[a]	δ (J2000)[b]	I_J [ADU]	δI_J [ADU]	Q_J [ADU]	δQ_J [ADU]
17452672−2903097	17:45:26.72	−29:03:09.7	656	11	47	16
17452674−2857068	17:45:26.74	−28:57:06.8	null	null	null	null
17452675−2859202	17:45:26.75	−28:59:20.2	null	null	null	null
17452680−2858480	17:45:26.80	−28:58:48.0	432	10	46	16
17452680−2903003	17:45:26.80	−29:03:00.3	226	10	12	15

[a,b] Units of right ascension are hours, minutes, and seconds, and units of declination are degrees, arcminutes, and arcseconds.

Table 3.1: *Continued*

U_J [ADU]	δU_J [ADU]	p_J [%]	δp_J [%]	θ_J [°]	$\delta\theta_J$ [°]	J [mag]	δJ [mag]	X_J	Y_J
59	15	11.25	2.38	25.73	5.99	15.882	0.029	940.659	167.800
null	null	null	null	null	null	null	null	null	null
null	null	null	null	null	null	null	null	null	null
40	15	13.63	3.64	20.50	7.29	16.373	0.029	950.724	746.226
30	15	12.64	6.68	34.10	13.32	17.239	0.053	937.154	190.306

I_H [ADU]	δI_H [ADU]	Q_H [ADU]	δQ_H [ADU]	U_H [ADU]	δU_H [ADU]	p_H [%]	δp_H [%]	θ_H [°]	$\delta\theta_H$ [°]
24550	65	1447	113	1281	117	7.86	0.47	20.76	1.71
9243	46	425	70	552	72	7.50	0.78	26.20	2.92
null	null	null	null	null	null	null	null	null	null
19530	74	1511	119	991	123	9.23	0.62	16.63	1.93
5231	57	221	84	237	86	5.98	1.63	23.50	7.52

H [mag]	δH [mag]	X_H	Y_H	I_{K_S} [ADU]	δI_{K_S} [ADU]	Q_{K_S} [ADU]	δQ_{K_S} [ADU]	U_{K_S} [ADU]	δU_{K_S} [ADU]
12.264	0.048	939.830	172.931	74710	172	2902	310	3163	314
13.304	0.017	956.020	975.373	33569	116	925	186	1567	188
null	null	null	null	46071	297	2256	442	1726	443
12.448	0.026	949.605	751.615	60000	166	2835	281	1702	285
14.068	0.052	937.990	194.318	22988	148	790	221	876	220

p_{K_S} [%]	δp_{K_S} [%]	θ_{K_S} [°]	$\delta\theta_{K_S}$ [°]	K_S [mag]	δK_S [mag]	X_{K_S}	Y_{K_S}	Field
5.73	0.42	23.73	2.08	10.261	0.114	933.779	172.534	GC1745−2900E
5.39	0.56	29.72	2.93	11.193	0.018	945.013	974.028	GC1745−2900E
6.09	0.96	18.71	4.47	11.296	0.078	940.317	679.437	GC1745−2900E
5.49	0.47	15.49	2.46	10.534	0.026	940.002	750.426	GC1745−2900E
5.04	0.96	23.98	5.35	11.637	0.051	932.052	193.439	GC1745−2900E

3.3 Data Quality for Point Sources

3.3.1 Seeing

Angular resolutions in ground-based observations are limited by atmospheric seeing. Good seeing is necessary to resolve point sources in dense stellar fields, like the GC. Figure 3.3 shows histograms of seeing sizes for the observed fields, which were measured in photometry for point sources on Stokes I images (§3.2.1). The means of seeing sizes were $1\farcs3$, $1\farcs2$, and $1\farcs1$ in the J, H, and K_S bands, respectively.

3.3.2 Photometric Accuracy

In order to evaluate the photometric accuracy, we compared magnitudes of the same point sources in overlapping regions between adjacent fields. Using the point sources with magnitude errors ≤ 0.05 mag, we calculated average differences of magnitude in each overlapping region (Fig. 3.4). The means of the average differences of magnitude in overlapping regions were 0.027 mag, 0.029 mag, and 0.027 mag in the J, H, and K_S bands, respectively. From these values, we evaluated the photometric accuracy to be about 0.03 mag in all the bands.

3.3.3 Polarimetric Accuracy

We checked our observations and analysis by comparing our polarimetry of the polarimetric standard star R CrA No. 88 with that by Whittet et al. (1992). The values p and θ were derived by averaging normalized Stokes parameters Q/I and U/I obtained from 15 observations. Their errors δp and $\delta\theta$ were determined from standard deviations of means of Q/I and U/I. Note that the observations by Whittet et al. (1992) were made in a non-standard K passband whose central wavelength is 2.04 μm. The degree of polarization in the K_S band was calculated by using the power law extrapolation of the values measured at 1.64 and 2.04 μm in the same manner as Gerakines et al. (1995). As shown in Table 3.2, we confirmed that the results of our polarimetry are consistent with those of Whittet et al. (1992) within the errors in all the bands.

Table 3.2: Polarimetry of R CrA No. 88.

	p_J [%]	θ_J [°]	p_H [%]	θ_H [°]	p_{K_S} [%]	θ_{K_S} [°]
this study	3.83 ± 0.17	90 ± 1	2.66 ± 0.18	91 ± 1	1.60 ± 0.21	92 ± 3
Whittet et. al.	3.87 ± 0.06	90 ± 1	2.73 ± 0.07	92 ± 1	1.69 ± 0.08[a]	95 ± 1

[a] The value at 2.14 μm was calculated by the power law extrapolation of the values measured at 1.64 and 2.04 μm.

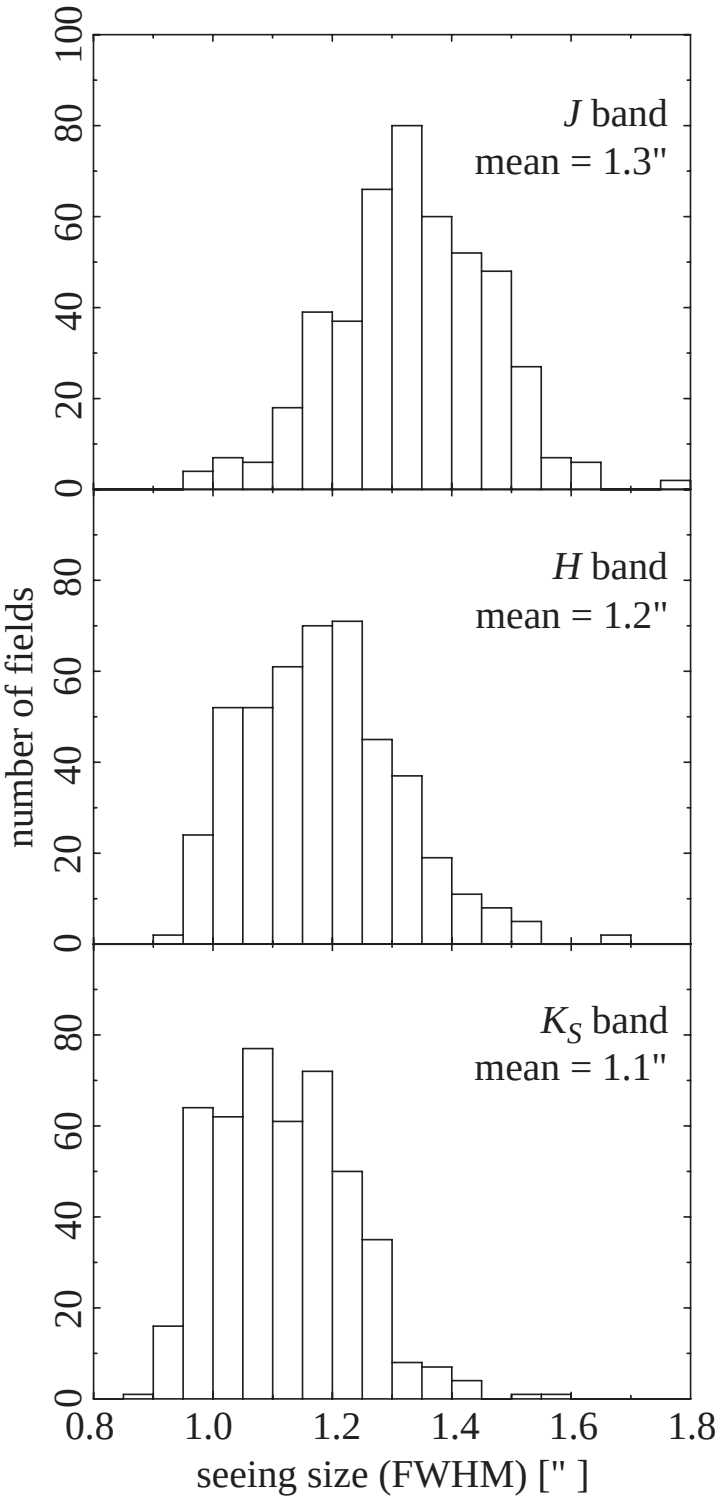

Figure 3.3: Histograms of seeing sizes for the observed fields at the J (*top*), H (*middle*), and K_S (*bottom*) bands, respectively. The means of seeing sizes are shown at the upper right of the panels.

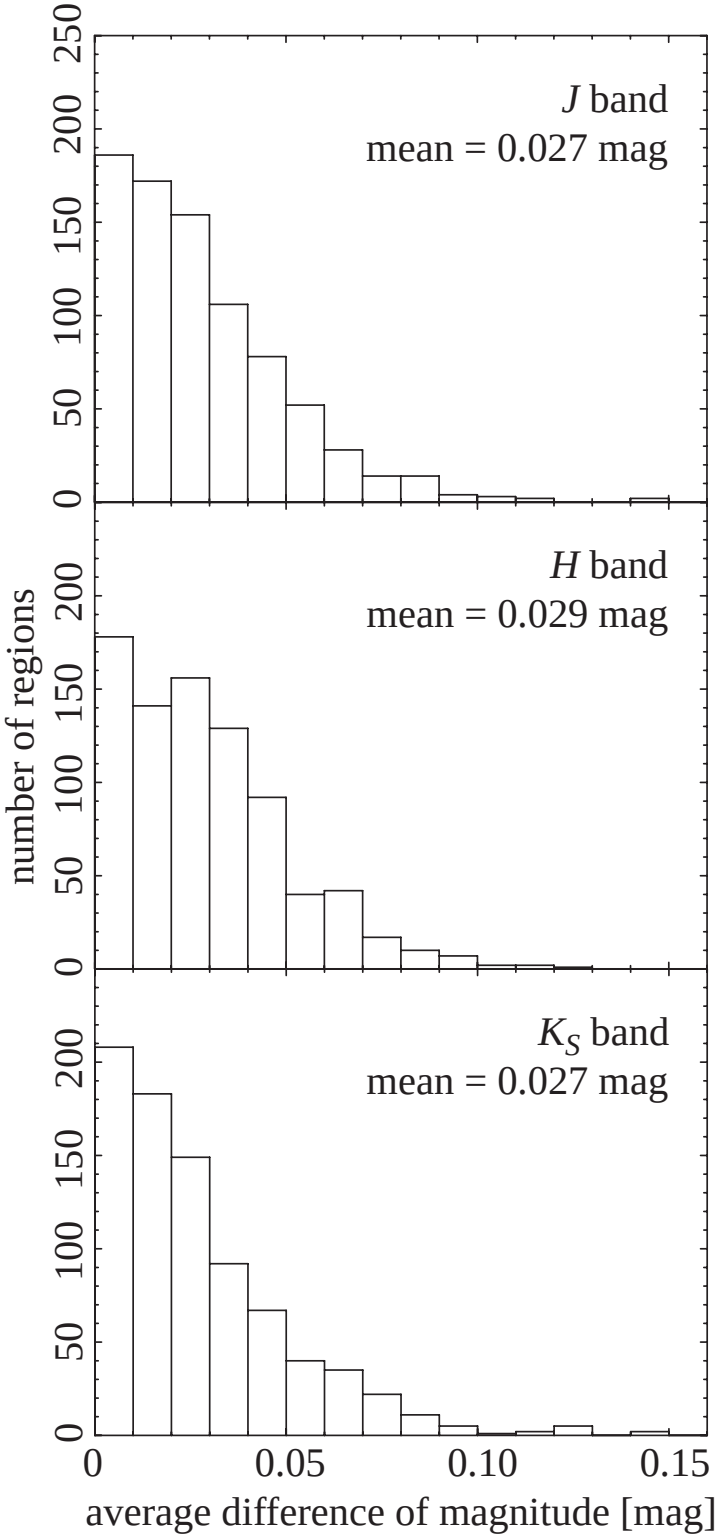

Figure 3.4: Histograms of average differences of magnitude in the J (*top*), H (*middle*), and K_S (*bottom*) bands based on the comparison of the same sources in overlapping regions between adjacent fields. The means of the average differences of magnitude in overlapping regions are shown at the upper right of the panels.

To evaluate the polarimetric accuracy, we compared p and θ of the same point sources in overlapping regions between adjacent fields. Using the point sources with $\delta p \leq 1\%$ and $\delta\theta \leq 10°$, we calculated average differences of p and θ in each overlapping region (Figs. 3.5 and 3.6). The means of the average differences of p in overlapping regions were 0.32%, 0.23%, and 0.22%, and those of θ were $3\overset{\circ}{.}11$, $2\overset{\circ}{.}89$, and $3\overset{\circ}{.}95$ in the J, H, and K_S bands, respectively. From these values, we evaluated the accuracy of p to be about 0.3% in the J band, and about 0.2% in the H and K_S bands. The accuracy of θ was also evaluated to be about 3° in the J and H bands, and about 4° in the K_S band.

3.3.4 Astrometric Accuracy

We evaluate the astrometric accuracy by comparing right ascension and declination of the same point sources in overlapping regions between adjacent fields. Using the point sources with magnitude errors ≤ 0.05 mag, average differences of right ascension and declination in each overlapping region were calculated (Fig. 3.7). The means of the average differences of right ascension and declination in overlapping regions were $0\overset{''}{.}02$ and $0\overset{''}{.}02$ in the J band, $0\overset{''}{.}02$ and $0\overset{''}{.}02$ in the H band, and $0\overset{''}{.}02$ and $0\overset{''}{.}02$ in the K_S band. From these values, we evaluated the accuracy of right ascension and declination to be about $0\overset{''}{.}02$ and $0\overset{''}{.}02$ in all the bands.

3.3.5 Limiting Magnitude

We evaluated the limiting magnitudes to polarization degree error of 1% for point sources. Distributions of polarization degree errors vs. magnitudes for point sources are shown in Figure 3.8. From the medians of magnitudes of the point sources whose errors of polarization degree range from 0.95 to 1.05%, the limiting magnitudes were evaluated to be 14.0 mag, 13.4 mag, and 12.5 mag in the J, H, and K_S bands, respectively.

Hereafter we use only the point sources with $\delta p \leq 1\%$ for the scientific results presented in this thesis. Numbers of the point sources with $\delta p \leq 1\%$ amount to 234,121, 541,990, and 558,647 in the J, H, and K_S bands, respectively.

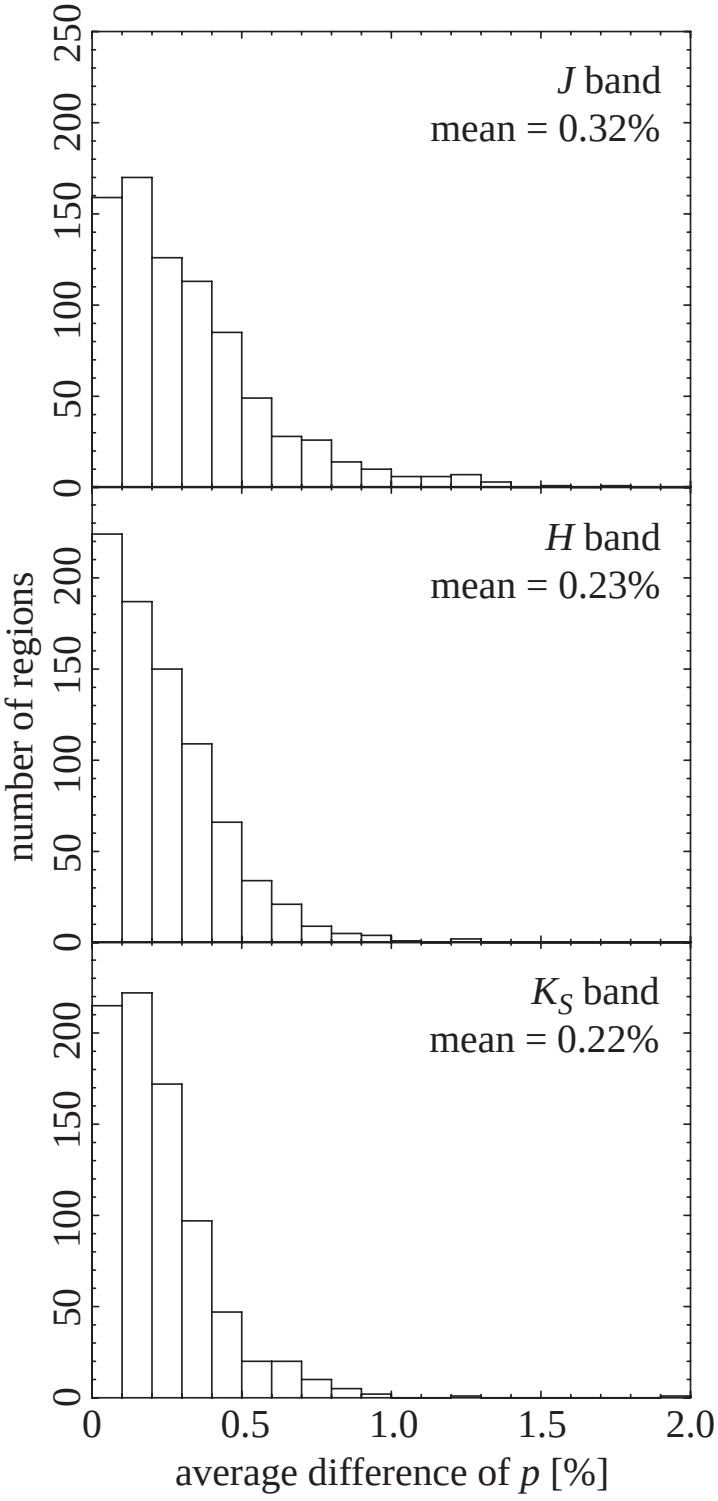

Figure 3.5: Histograms of average differences of p in the J (*top*), H (*middle*), and K_S (*bottom*) bands based on the comparison of the same sources in overlapping regions between adjacent fields. The means of the average differences of p in overlapping regions are shown at the upper right of the panels.

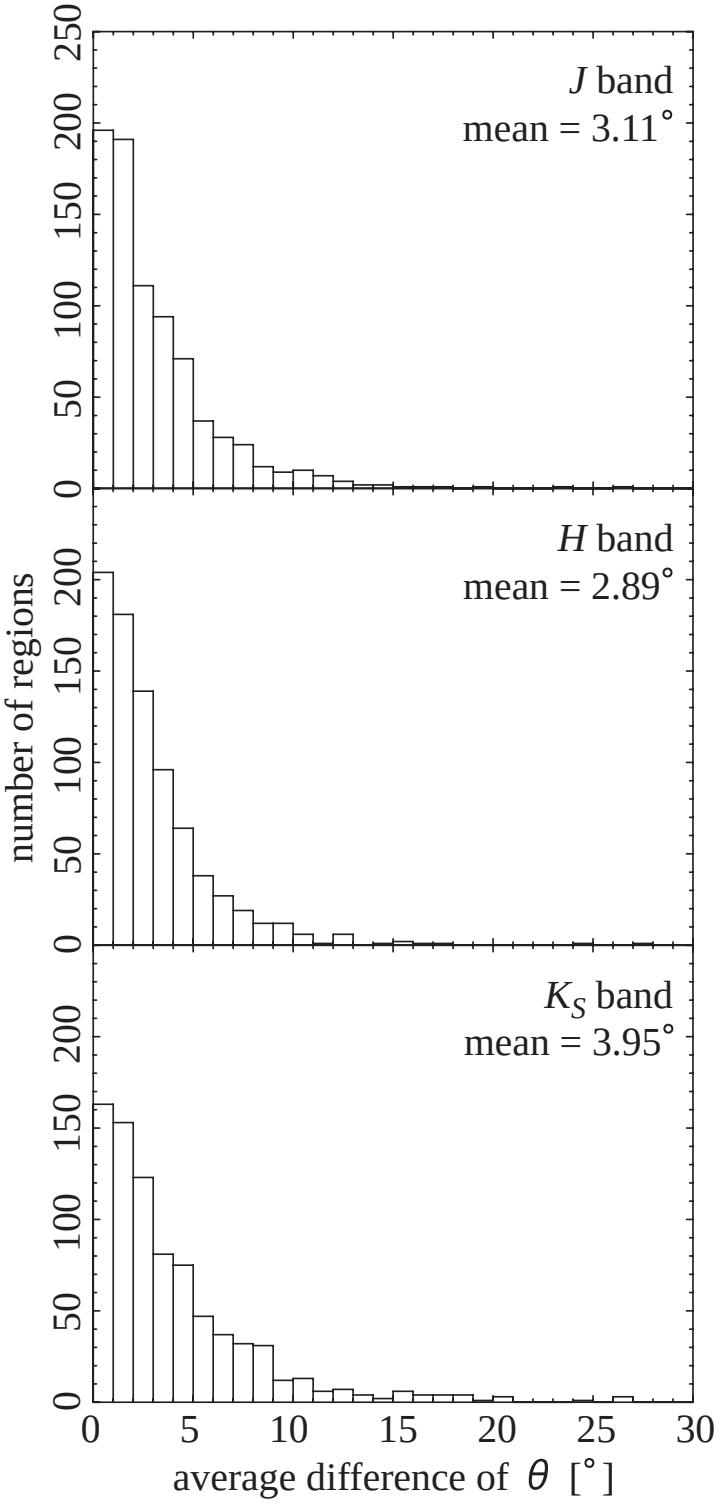

Figure 3.6: Histograms of average differences of θ in the J (*top*), H (*middle*), and K_S (*bottom*) bands based on the comparison of the same sources in overlapping regions between adjacent fields. The means of the average differences of θ in overlapping regions are shown at the upper right of the panels.

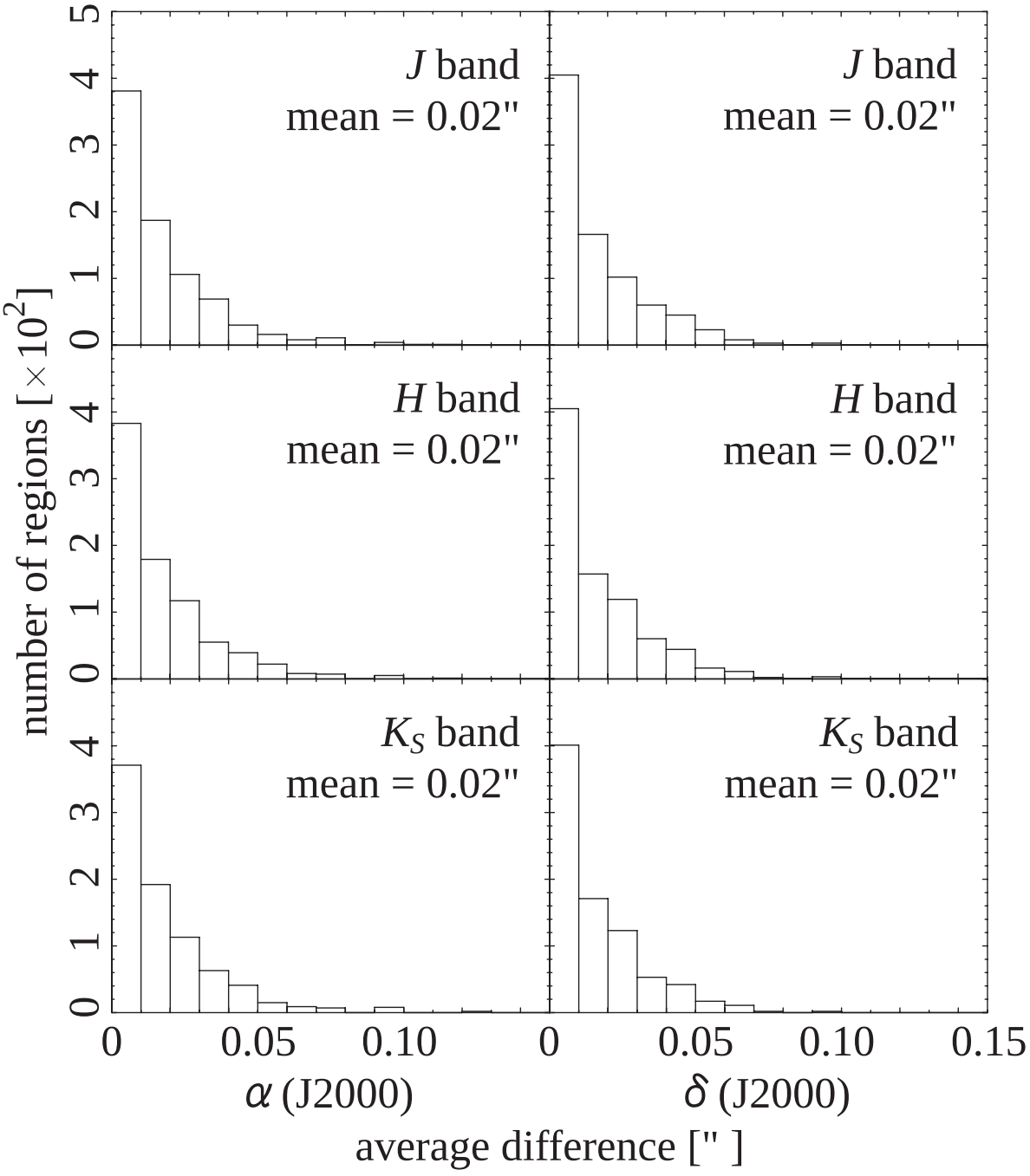

Figure 3.7: Histograms of average differences of right ascension ($left$) and declination ($right$) in the J (top), H ($middle$), and K_S ($bottom$) bands based on the comparison of the same sources in overlapping regions between adjacent fields. The means of the average differences of right ascension and declination in overlapping regions are shown at the upper right of the panels.

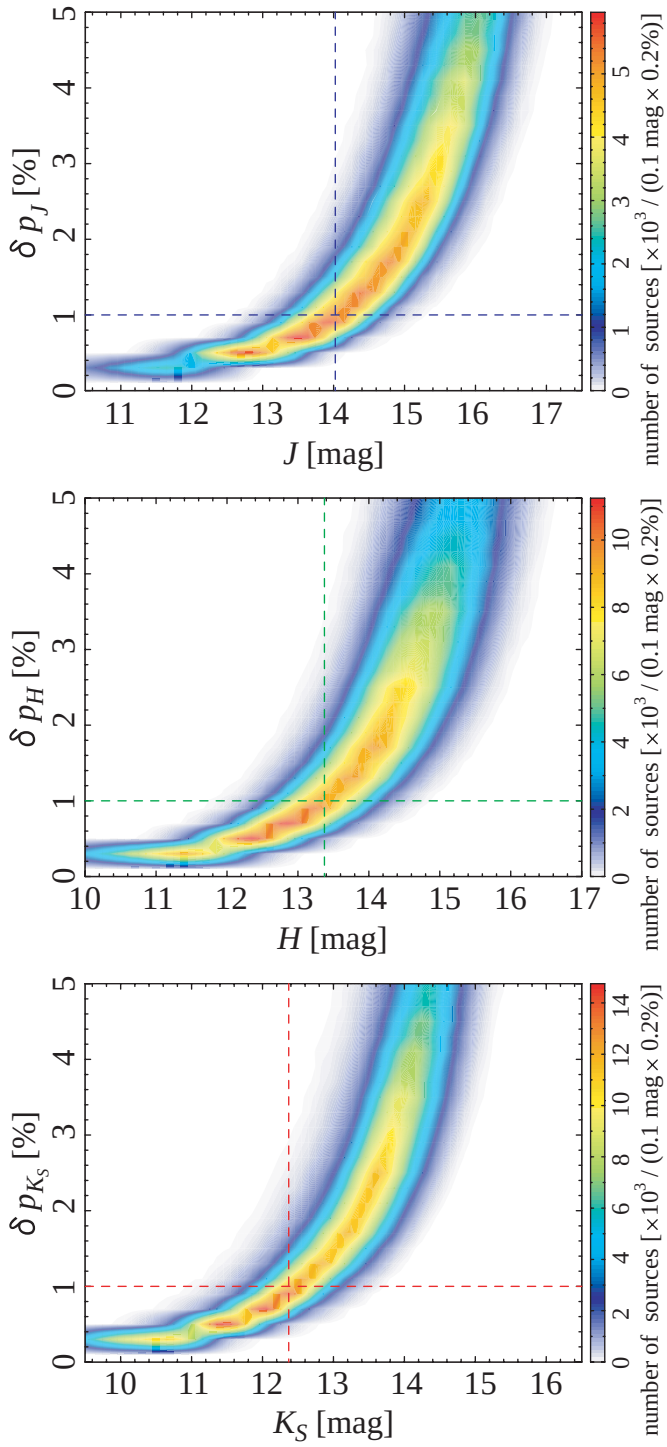

Figure 3.8: Errors of polarization degree for point sources as a function of their magnitudes in the J (*top*), H (*middle*), and K_S (*bottom*) bands. The horizontal and vertical dashed lines indicate $\delta p = 1\%$ and the corresponding limiting magnitudes.

3.4 Data Analysis for Extended Sources

For extended sources, we obtained polarized intensity PI, p, and θ images on which the parameters were calculated in each pixel. First we subtracted mode of sky background level from Stokes I image so that only flux from astronomical sources was left on the image. We also set modes of sky background levels on instrumental Stokes Q or U images to zero in order to correct differences of sky background levels between frames of wave plate angles at 0° and 45° or 22.°5 and 67.°5. Statistical errors of Stokes I, instrumental Stokes Q and U on the sky corrected images were calculated from flux and noise on the images for each wave plate angle in the same manners with point sources. We also calibrated instrumental Stokes Q and U and their errors for the correction angle and polarization efficiency of the wave plate and polarizer (Kandori et al. 2006).

Then we derived observed polarized intensity $PI_{\rm obs}$ and its error δPI by the equations:

$$PI_{\rm obs} = \sqrt{Q^2 + U^2} \quad [\mathrm{ADU}],$$

$$\delta PI = \frac{\sqrt{Q^2 \times {\delta Q_{\rm sta}}^2 + U^2 \times {\delta U_{\rm sta}}^2}}{PI_{\rm obs}} \quad [\mathrm{ADU}].$$

To correct noise biasing, PI was calculated by the following equation:

$$PI = \sqrt{{PI_{\rm obs}}^2 - \delta PI^2} \quad [\mathrm{ADU}].$$

Pixels with $PI_{\rm obs} \leq \delta PI$ were regarded as unpolarized ($PI = 0$). We also derived p, θ, and their errors by the equations:

$$p = \frac{PI}{I} \times 100 \quad [\%],$$

$$\delta p = \sqrt{\left(\frac{\delta PI}{I}\right)^2 + \left(\frac{PI_{\rm obs}}{I} \times \frac{\delta I}{I}\right)^2} \times 100 \quad [\%],$$

$$\theta = \frac{1}{2}\arctan\frac{U}{Q} \quad [^\circ],$$

$$\delta\theta = \frac{\sqrt{U^2 \times {\delta Q_{\rm sta}}^2 + Q^2 \times {\delta U_{\rm sta}}^2}}{Q^2 + U^2} \times \frac{180}{2\pi} \quad [^\circ].$$

Bibliography

Clarke, D., & Stewart, B. G. 1986, Vistas Astron., 29, 27

Gerakines, P. A., Whittet, D. C. B., & Lazarian, A. 1995, ApJ, 455, 171

Skrutskie, M. F., Cutri, R. M., Stiening, R., Weinberg, M. D., Schneider, S., Carpenter, J. M., Beichman, C., Capps, R., Chester, T., Elias, J., Huchra, J., Liebert, J., Lonsdale, C., Monet, D. G., Price, S., Seitzer, P., Jarrett, T., Kirkpatrick, J. D., Gizis, J. E., Howard, E., Evans, T., Fowler, J., Fullmer, L., Hurt, R., Light, R., Kopan, E. L., Marsh, K. A., McCallon, H. L., Tam, R., Van Dyk, S., Wheelock, S. 2006, AJ, 131, 1163

Tabur, V. 2007, PASA, 24, 189

Wardle, J. F. C., & Kronberg, P. P. 1974, ApJ, 194, 249

Whittet, D. C. B., Martin, P. G., Hough, J. H., Rouse, M. F., Bailey, J. A., & Axon, D. J. 1992, ApJ, 386, 562

Chapter 4

Interstellar Polarization Efficiency toward the Galactic Center

4.1 Introduction

From observations of interstellar polarization, position angles yield the directions of magnetic fields on the plane-of-the-sky. Mathewson & Ford (1970) compiled the polarization data of nearly 7000 stars and showed the distribution of position angles in Galactic coordinates (see Fig. 1.6). The distribution of position angles for the stars within 600 pc from us traces the structure of nearby magnetic field, while that for the stars more distant than 1 kpc traces the structure of extensive and uniform magnetic field. The large-scale magnetic field, that is, the Galactic magnetic field runs almost parallel to the spiral arms.

However, the structure of magnetic field is less simple at $l \sim 40°$, $80°$, $260°$, and away from the Galactic plane such as Taurus, Perseus, Ophiuchus, and Orion, where position angles show convergences or deviations. The interstellar magnetic field is obviously perturbed from the uniform, large-scale structure. This indicates the existence of a random component of the magnetic field on a small-scale.

The random component of the magnetic field would cause a dispersion of position angles and decrease of the polarization efficiency. The polarization efficiency is defined as a ratio of polarization degree to extinction such as p_λ/τ_λ and $p_{\lambda_2}/E(\lambda_1 - \lambda_2)$. If magnetic fields are tangled along the line-of-sight, degree of polarization p_λ does not build up as much as it would in a regular magnetic field. Extinction τ_λ or $E(\lambda_1 - \lambda_2)$, is determined only by the total amount of dust grains integrated throughout the line-of-sight, so that the polarization efficiency decreases (depolarization; Martin 1974). Thus, the polarization efficiency is a useful measure to probe the random component of the magnetic field.

Serkowski et al. (1975) analyzed a sample of 180 nearby stars that were observed polarimetrically in the U, B, V, and R bands at the optical wavelengths. They investigated a relation between maximum degree of polarization $p_{\max}$ (which occurs at $\lambda_{\max}$) and color excess $E(B-V)$ (Fig. 4.1), and empirically established an upper limit of the polarization efficiency,

$$p_{\max}/E(B-V) \leq 9.0\%/\mathrm{mag}.$$

The polarization efficiency changes from line-to-line of sight below the upper limit.

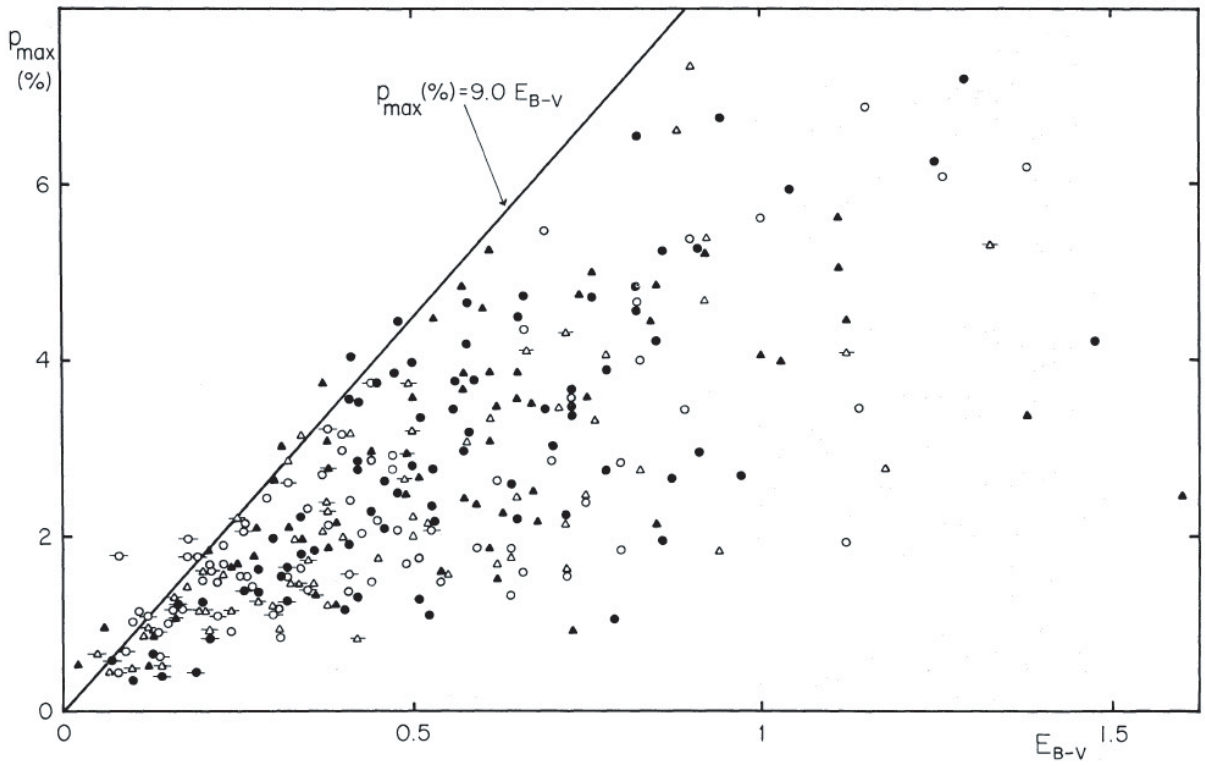

Figure 4.1: The relationship between the maximum interstellar polarization $p_{\max}$ and color excess $E(B-V)$ (Fig. 9 of Serkowski et al. 1975). A straight line corresponds to $p_{\max}/E(B-V) = 9.0$.

Toward and/or around individual dense clouds, a number of detailed polarimetric observations have been carried out at the optical and/or NIR wavelengths (e.g., references in Myers & Goodman 1991 and Jones 1989). Based on optical polarization maps for 26 dense clouds with and without an embedded star cluster, Myers & Goodman (1991) studied a relationship between a dispersion of position angles and existence of a cluster, and found that most clouds have well-defined means of position angles and that clouds with a cluster show larger dispersions of position angles over the spatial extent than clouds without a cluster. They modeled the observed distribution of position angles as arising from the uniform and random components of the magnetic field and argued that the magnetic energy density of each component is comparable inside such dense clouds if the cloud has a few correlation intervals of the random component of the magnetic field along the line-of-sight.

The behavior of the polarization efficiency at much higher extinction was studied by Jones (1989) and Jones et al. (1992). They compiled K band (2.2 μm) polarimetric measurements for about 100 sources at various locations and extinctions, and found that a good correlation between polarization and extinction holds (Fig. 4.2). By comparing the correlation and their model involving the decorrelation length of the random component of the magnetic field along the line-of-sight, they suggested equipartition of the energy density between the uniform and random components of the magnetic field.

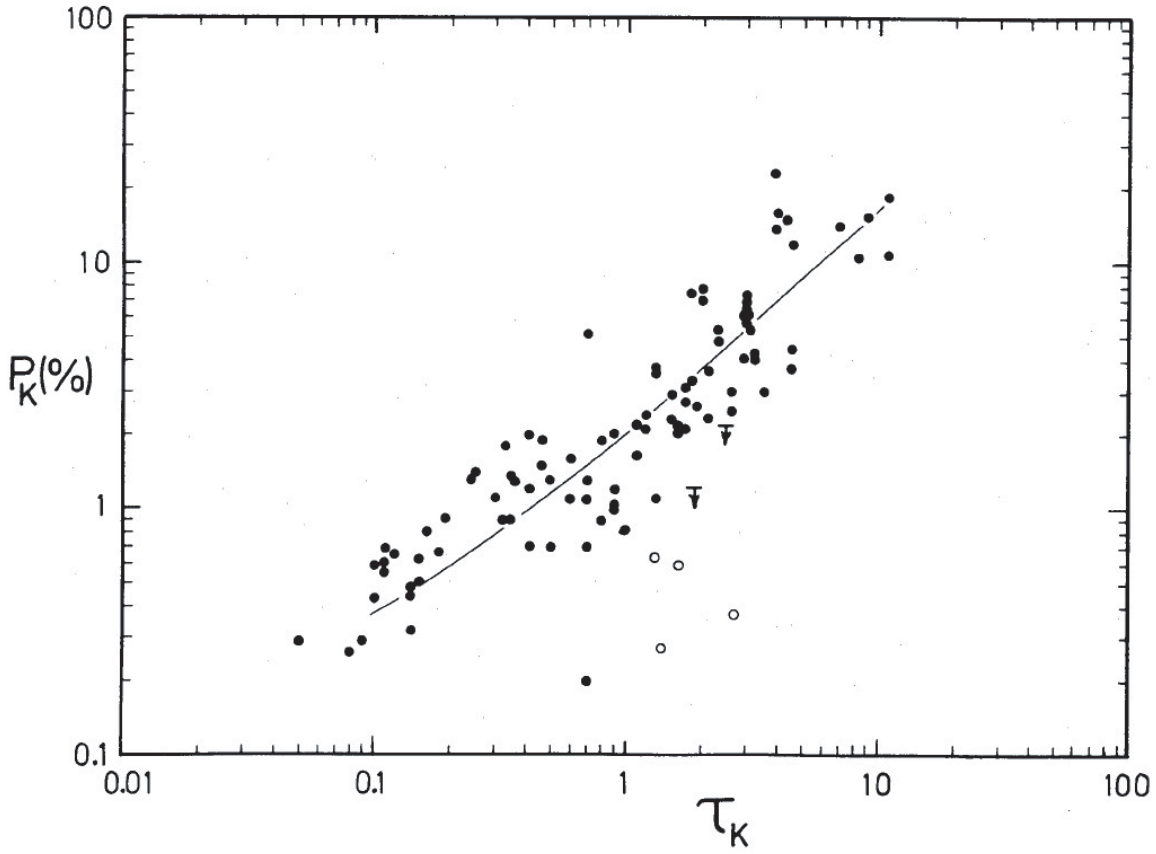

Figure 4.2: Plot of observed linear polarization at K (2.2 μm) vs. the optical depth along the line-of-sight to the star at 2.2 μm (Fig. 3 of Jones 1989). The solid line represents the results of model calculations for a magnetic field that is made up of equal contributions from a uniform component and a random component. The random component is 45% of the total field strength. The values for η, which is the ratio of the net extinction perpendicular to the grain's long axis to the net extinction parallel to the grain's long axis, is 0.9, and decorrelation length $\Delta\tau$ is 0.1.

Studies on the polarization efficiency of the diffuse ISM were carried out using the polarization data compiled comprehensively by Heiles (2000). Based on the polarization data for about 5,500 stars distributed over the entire sky and mostly located nearby at distances of $d \lesssim 4$ kpc, Fosalba et al. (2002) found a nearly linear growth of average polarization degree with extinction up to $E(B-V) \sim 1$ mag, but noted that the polarization efficiency is much lower than what is expected from the completely aligned grains under a regular magnetic field (Fig. 4.3). The ratio of observed to the upper limit of the polarization efficiency $p_{\rm obs}/p_{\rm max}$ is approximately 0.39, where $p_{\rm max}/E(B-V) = 9.0\%$ / mag (Serkowski et al. 1975); the polarization efficiency is about one-third of the upper limit. They explained lower polarization efficiency by depolarization due to the random component of the magnetic field, and estimated the magnetic field strength ratio of the uniform to the random component to be $B_u/B_r \approx 0.8$, where B_u and B_r are the strengths of the uniform and random components.

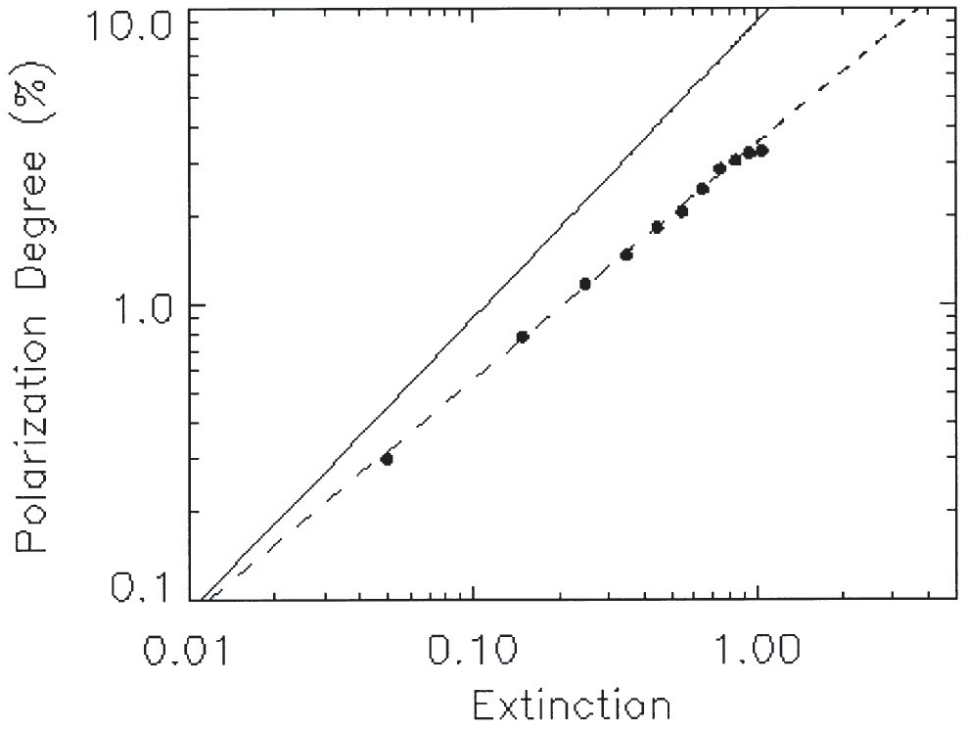

Figure 4.3: Correlation between polarization degree p averaged in extinction bin and extinction $E(B-V)$ (lower panel of Fig. 4 of Fosalba et al. 2002). Solid line shows the theoretical upper limit, $p_{\rm max} = 9.0\ E(B-V)$, for completely aligned grains by external (regular) magnetic fields. Dashed line shows $p_{\rm obs} = 3.5\ E(B-V)^{0.8}$, which is a good fit to the data up to $E(B-V) \approx 1$.

In the innermost region of the Galaxy, only a few polarimetric observations have been done (e.g., Kobayashi et al. 1983, 1986; Creese et al. 1995), except for far-infrared and radio wavelengths polarization. Kobayashi et al. (1983, 1986) measured polarization for highly reddened stars in the areas at $l \sim 0°$, $20°$, and $30°$ in the Galactic plane, and noted that the polarization efficiency is lower by a factor of about four than that in the solar neighborhood. Based on polarization measurements for 127 reddened stars, Creese et al. (1995) also concluded that greater extinction results in increased polarization, but the increase is smaller than expected. Their samples are not highly extinct ($H-K \lesssim 0.7$ mag), because they were selected from an I band objective prism survey. These observations were so sparse and shallow.

Now polarimetric imaging observations using several hundred thousand stars lying in the Galactic bulge as background sources enable us to measure polarization degrees, position angles, and color excess finely across the area and deeply to the line-of-sight. In this chapter, we provide information of the magnetic field in the deep inside of the Galaxy, based on numerous starlight polarization data obtained by our wide field ($\sim 3° \times 2°$) survey. From the polarization efficiency and dispersions of position angles, we discuss the uniform and random components of the magnetic field along the line-of-sight on the Galactic scale.

4.2 Results

4.2.1 MK Classifications and Locations

A color-color diagram for the sources is shown in Figure 4.4. There are three distinct populations; the majority of the sources are involved in a feature extended parallel to the reddening vector from the locus of giants, while two weak concentrations of the sources are seen around ($H - K_S$, $J - H$)$\sim$(0.1, 0.3) mag and $\sim$(0.2, 0.7) mag. The extended feature mainly consists of heavily reddened K/M giants located in the Galactic bulge, and the concentrations less reddened A/F dwarfs and K giants located in the Galactic disk. These MK classifications (spectral types and luminosity classes) and locations (disk or bulge) of the sources are estimated based on the model by Wainscoat et al. (1992) and our K_S band limiting magnitude ($\sim$12.5 mag; §3.3.5).

We divide the sources into two groups at $H - K_S \sim 0.4$ mag, where a saddle of the extended feature of giants exists; the disk sources are with $H - K_S < 0.4$ mag and bulge sources are with $H - K_S \geq 0.4$ mag. The numbers of the disk and bulge sources with $\delta p \leq 1\%$ amount to 58,007 and 138,644 in the J band, 54,102 and 457,928 in the H band, and 31,448 and 513,227 in the K_S band, respectively.

4.2.2 Color Excess

We calculate color excess of the sources using the color excess method (Lada et al. 1994):

$$E(H - K_S) = (H - K_S) - \langle (H - K_S)_0 \rangle.$$

The mean $\langle (H-K_S)_0 \rangle$ and the standard deviation of intrinsic colors of stars σ are derived by the equations:

$$\langle (H - K_S)_0 \rangle = \frac{\sum_{\rm C} \{(H - K_S)_{\rm C0} \times {\rm N_C}\}}{\sum_{\rm C} {\rm N_C}},$$

$$\sigma = \sqrt{\frac{\sum_{\rm C} [\{(H - K_S)_{\rm C0} - \langle (H - K_S)_0 \rangle\}^2 \times {\rm N_C}]}{\sum_{\rm C} {\rm N_C}}},$$

where $(H - K_S)_{\rm C0}$ and $\rm N_C$ are intrinsic color (Koornneef 1983; Bessell & Brett 1988) and number of stars with the MK classification. Based on the model by Wainscoat et al. (1992), we estimate the source numbers to be detected within the K_S band limiting magnitude ($\sim$12.5 mag) and with (i) $H-K_S < 0.4$ mag for the disk sources, or (ii) $H-K_S \geq 0.4$ mag for the bulge ones. $\langle (H - K_S)_0 \rangle$ and σ are estimated to be 0.08$-$0.10 mag and 0.04$-$0.05 mag for the disk sources, and 0.18$-$0.22 mag and 0.04$-$0.06 mag for the bulge ones for each line-of-sight. The bulge sources are dominated by K/M giants, and have an average intrinsic color redder than that of the disk ones being mainly composed of A/F dwarfs and K giants (§4.2.1).

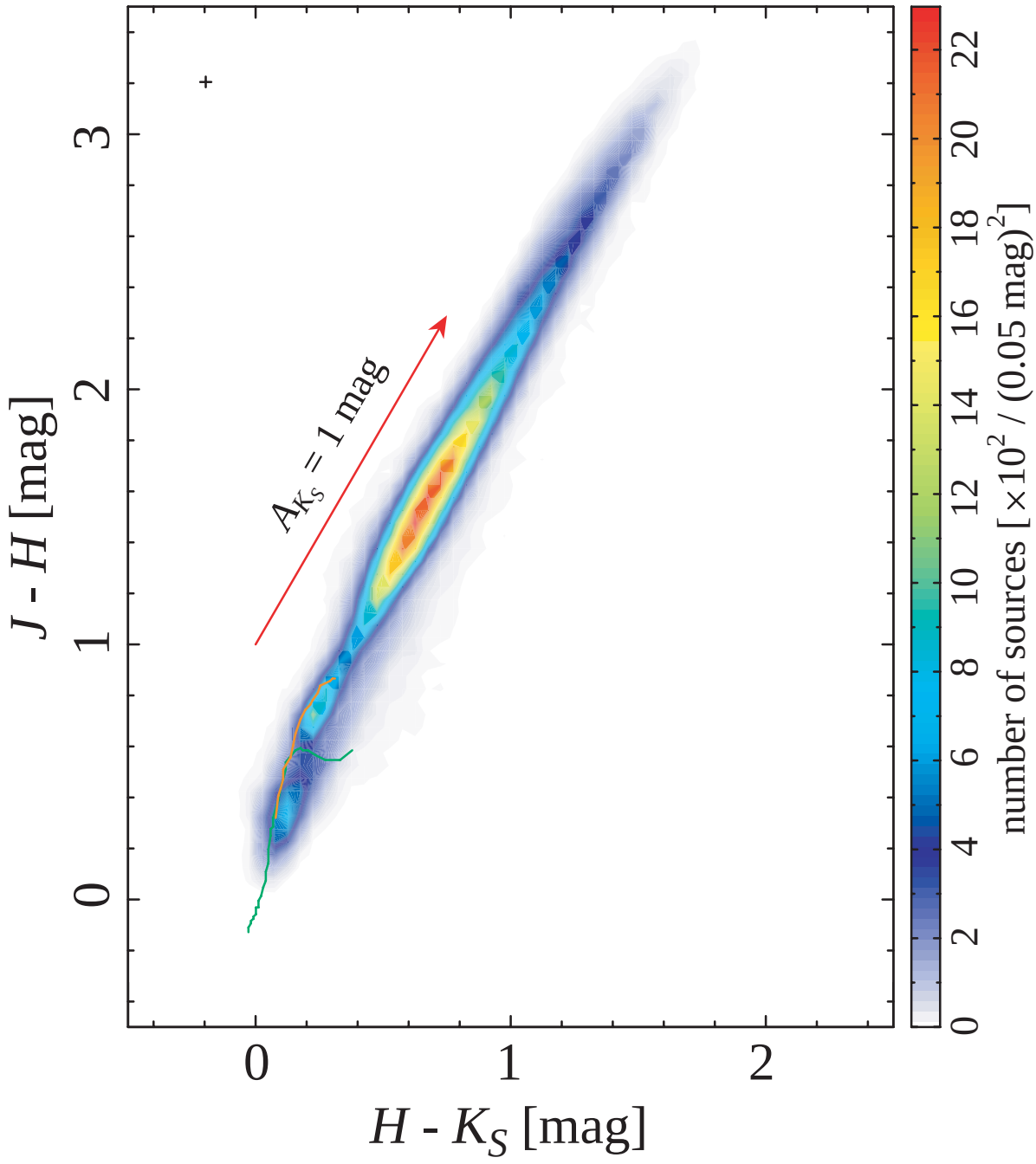

Figure 4.4: $J - H$ vs. $H - K_S$ color-color diagram for the sources that are detected in all the bands and with $\delta p \leq 1\%$. The green and orange curves are the loci of dwarfs and giants, respectively. The data for O9−B9 dwarfs are from Koornneef (1983), and those for A0−M6 dwarfs and G0−M7 giants are from Bessell & Brett (1988). The arrow indicates a reddening vector whose slope is 1.72 (Nishiyama et al. 2006), and its length corresponds to extinction of $A_{K_S} = 1$ mag. The upper left cross denotes the average errors of colors for the sources.

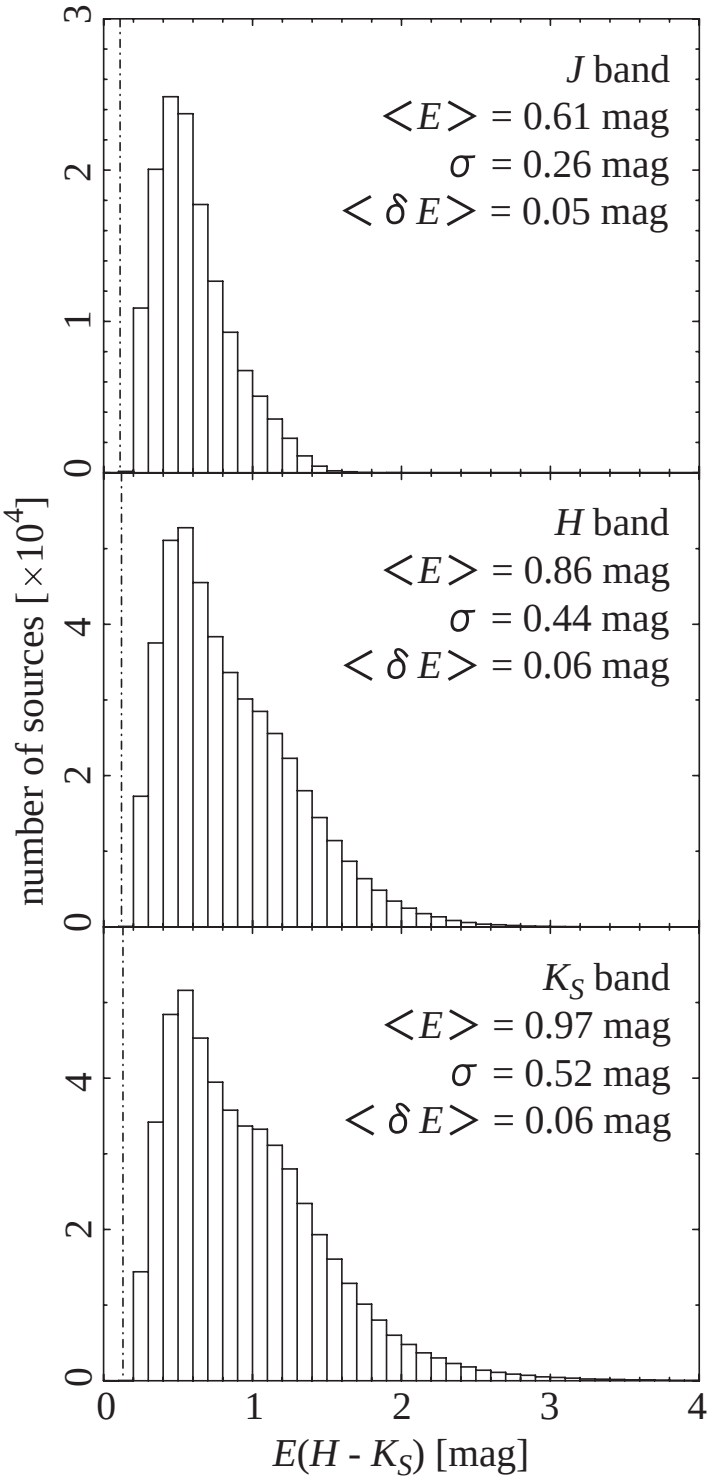

Figure 4.5: Histograms of color excess $E(H-K_S)$ for the bulge sources with $\delta p \leq 1\%$ in the J (*top*), H (*middle*), and K_S (*bottom*) bands. The means, standard deviations, and average errors of $E(H-K_S)$ for the bulge sources are shown at the upper right of the panels. The dash-dotted lines in each panel show the means of $E(H-K_S)$ for the disk sources with $\delta p \leq 1\%$.

$E(H-K_S)$ for a disk source is not so large compared with its error, and therefore cannot be accurately determined. We consider only means of $E(H-K_S)$ for the disk sources. From the means of $H-K_S$ (0.20 mag, 0.21 mag, and 0.22 mag) and average intrinsic color of the disk sources (0.09 mag), the means of $E(H-K_S)$ are calculated to be 0.11 mag, 0.12 mag, and 0.13 mag for the disk sources in the J, H, and K_S bands, respectively (dash-dotted lines in Fig. 4.5).

We show histograms of $E(H-K_S)$ for the bulge sources in Figure 4.5. The distributions of $E(H-K_S)$ peak at about 0.5 mag and have tails toward large color excess in all the bands. The bulge sources in the H and K_S bands trace larger color excess than those in the J band because of the wavelength dependence of interstellar extinction.

We draw a map of $E(H-K_S)$ for the bulge sources in the K_S band as follows. The analyzed area (Fig. 3.1) is divided into cells with a size of $2' \times 2'$. Means of $E(H-K_S)$ for the bulge sources in the K_S band are calculated in each cell. The size of cells is determined to sample as many sources in each cell as possible not to degrade the angular resolution. The resultant map of the mean $\langle E(H-K_S)\rangle$ is shown in Figure 4.6. The map shows the spatial variation of interstellar extinction depending on Galactic latitude. The cells with large values $\langle E(H-K_S)\rangle \geq 2$ mag mainly concentrate to the Galactic plane ($|b| \leq 0.^{\circ}5$), and show clumpy and filamentary structures.

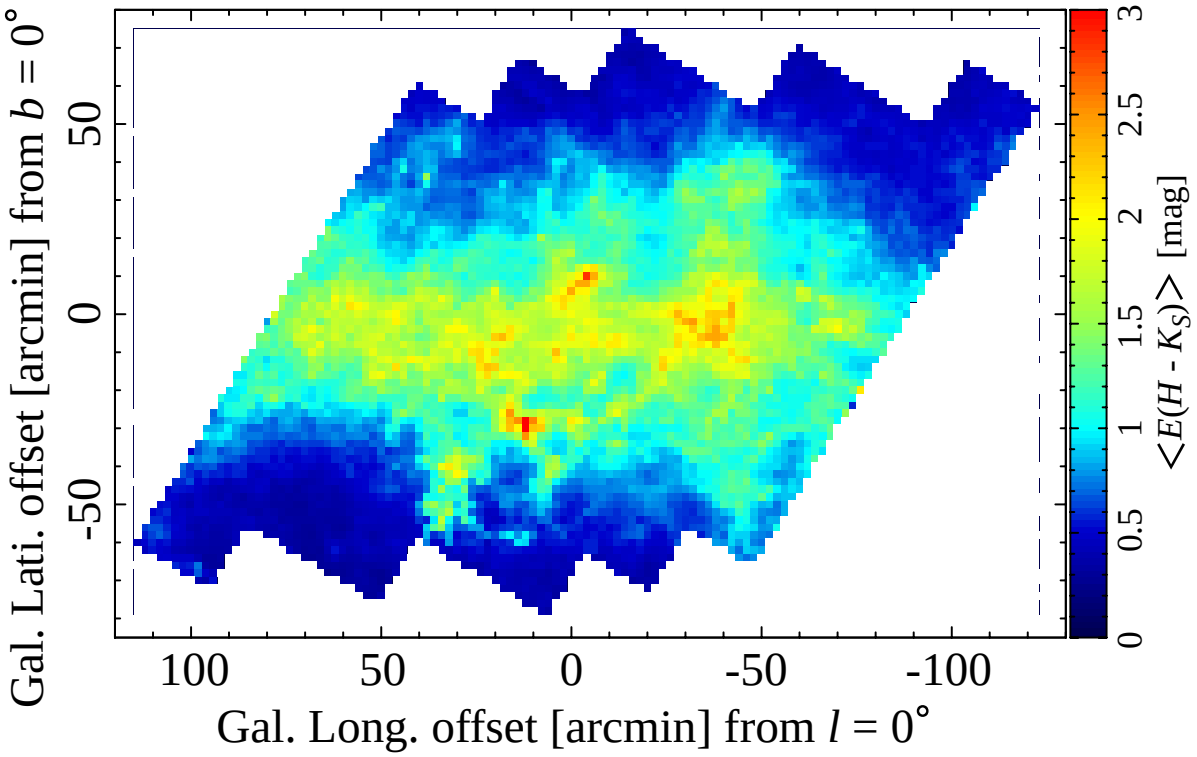

Figure 4.6: Map of $E(H-K_S)$. Each pixel represents a mean of $E(H-K_S)$ for the bulge sources with $\delta p_{K_S} \leq 1\%$ in each cell with a size of $2' \times 2'$.

4.2.3 Degree of Polarization and Position Angle

We plot a K_S band polarization vector map for the disk and bulge sources in Figure 4.7. Most of the sources show the $\boldsymbol{E}$-vectors of polarization nearly parallel to the Galactic plane, while there exist some deviations. These deviations of $\boldsymbol{E}$-vectors are seen in the regions where a relatively few sources are detected with large color excess. This suggests that the deviated $\boldsymbol{E}$-vectors reflect the local magnetic field directions in nearby dense clouds.

Figure 4.8 shows the relations between position angles and colors for the sources, in which there are two distinct populations in blue ($H - K_S < 0.4$ mag) and red ($H - K_S \geq 0.4$ mag) colors, each of which corresponds to the disk and bulge sources as discerned in the color-color diagram (§4.2.1). The blue populations for the disk sources are prominent in the J band, but less prominent in the H and K_S bands. In this figure, only the sources with $\delta\theta \leq 10^\circ$ are shown; the numbers of the disk and bulge sources amount to 38,425 and 118,045 in the J band, 20,858 and 355,124 in the H band, and 6,086 and 323,603 in the K_S band. The distributions of θ clearly differ between two populations; the means of θ are $9\overset{\circ}{.}3$, $10\overset{\circ}{.}3$, and $11\overset{\circ}{.}4$ for the bulge sources, while $-1\overset{\circ}{.}6$, $-2\overset{\circ}{.}1$, and $0\overset{\circ}{.}0$ for the disk ones in the J, H, and K_S bands, respectively, as also noted by Kobayashi et al. (1983) and Nishiyama et al. (2009a). Most of the bulge sources have θ nearly parallel to the Galactic plane ($\sim 27^\circ$), but slightly rotated westward. Position angles rotate more for the disk sources.

In a similar manner as $E(H - K_S)$, we draw a map of θ_{K_S} for the bulge sources in Figure 4.9. Most of cells show the values $0^\circ \lesssim \langle\theta_{K_S}\rangle \lesssim 20^\circ$, which indicate that the magnetic field between the GC and us are averagely longitudinal. These values are close to the average position angle which traces the magnetic field configuration in the GC (16.0°; Nishiyama et al. 2009a), suggesting that the Galactic magnetic field running nearly parallel to the spiral arms would connect to the toroidal magnetic field in the GC (see also Novak et al. 2003; Chuss et al. 2003).

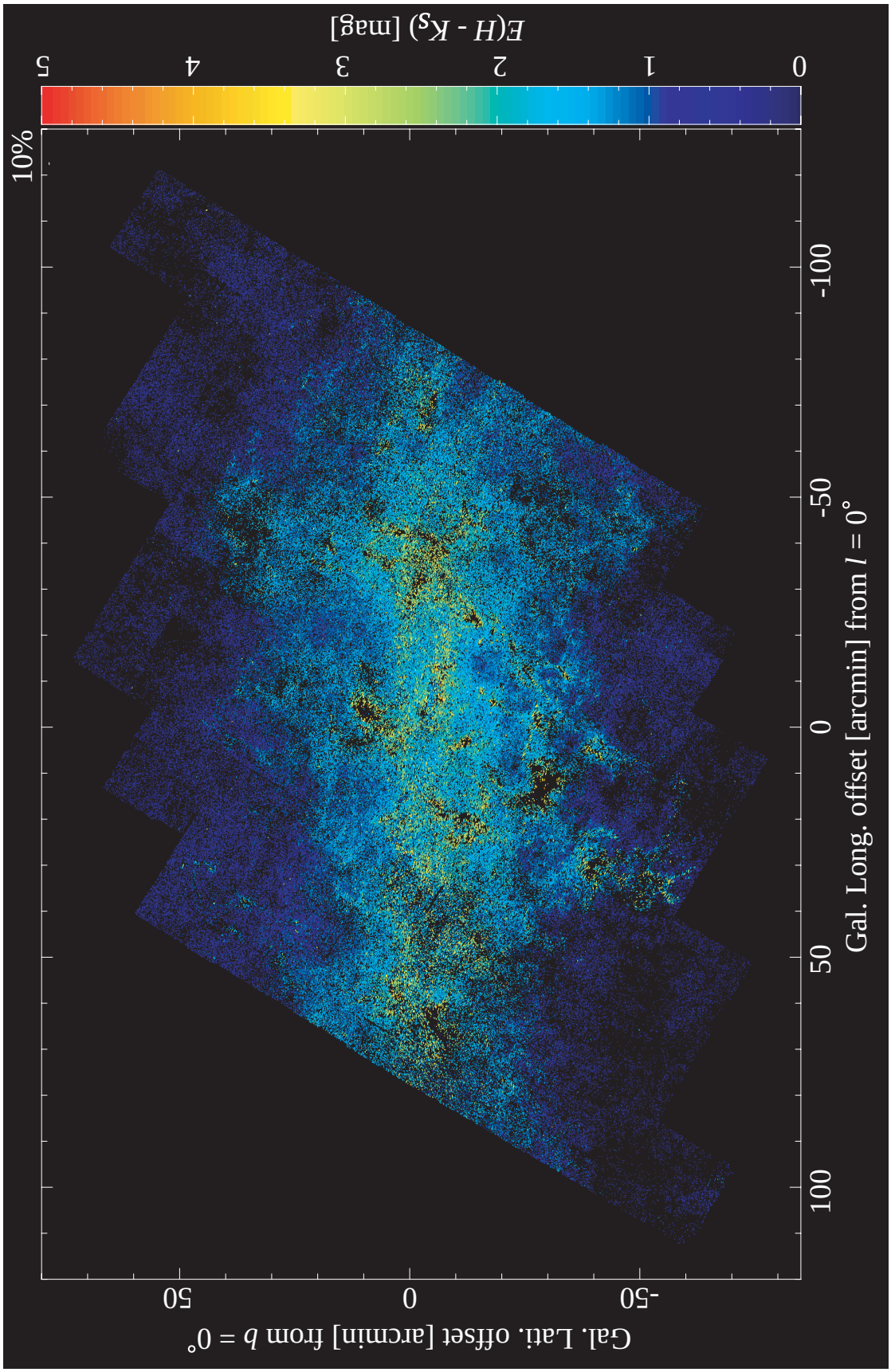

Figure 4.7: K_S band polarization vector map for the disk and bulge sources with $\delta p_{K_S} \leq 1\%$ and $\delta\theta_{K_S} \leq 10^\circ$. Each bar is parallel to the $\boldsymbol{E}$-vector of polarization. The length of each bar is proportional to degree of polarization. Color excess for the bulge sources is also shown as color of the bars. The disk sources are shown by white bars. Each bar including the bar for 10% scale of polarization degree at the upper right can be recognized by zooming the figure in the electronic edition.

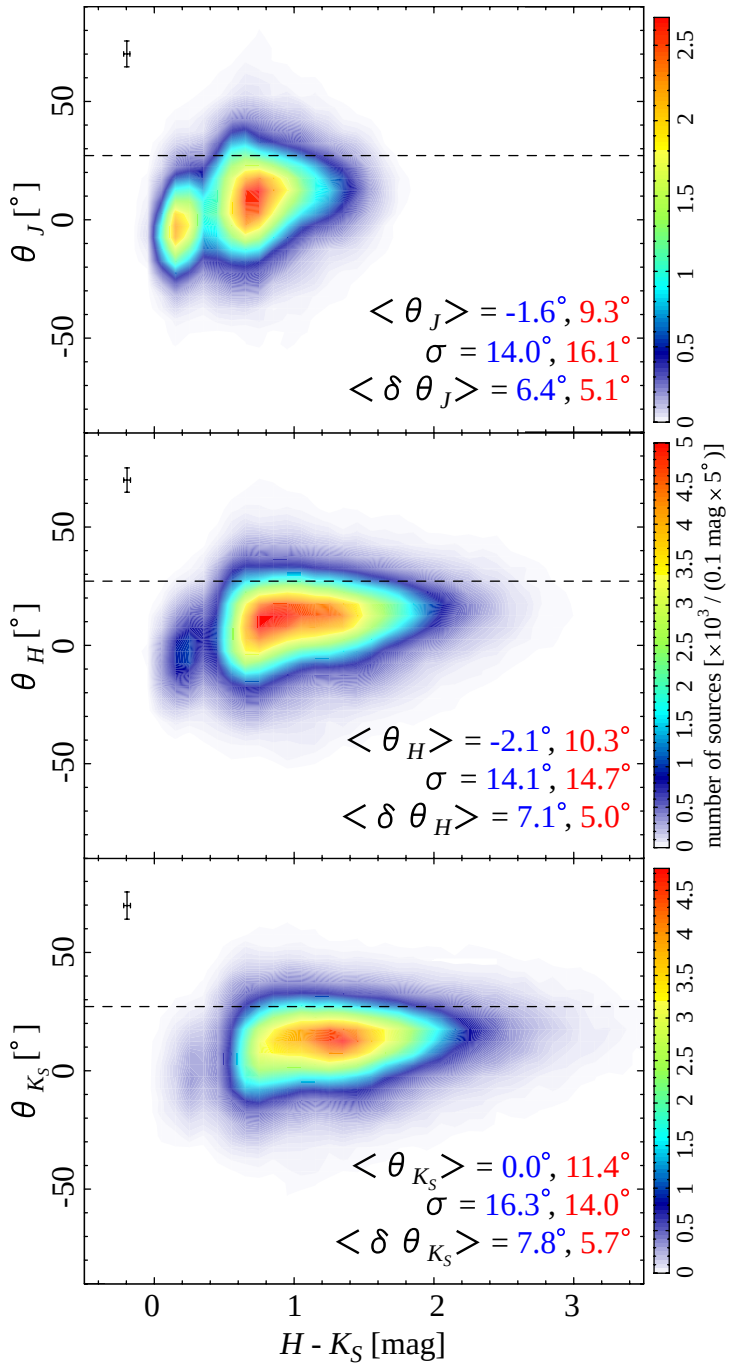

Figure 4.8: Position angles θ vs. $H - K_S$ colors for the sources with $\delta p \leq 1\%$ and $\delta\theta \leq 10^\circ$ in the J (*top*), H (*middle*), and K_S (*bottom*) bands. The dashed lines in each panel represent the orientation of Galactic plane ($\sim 27^\circ$). The means, standard deviations, and average errors of θ for the disk (*blue*) and bulge (*red*) sources are shown at the lower right of the panels. The upper left crosses in each panel denote the average errors of θ and $H - K_S$ for the sources.

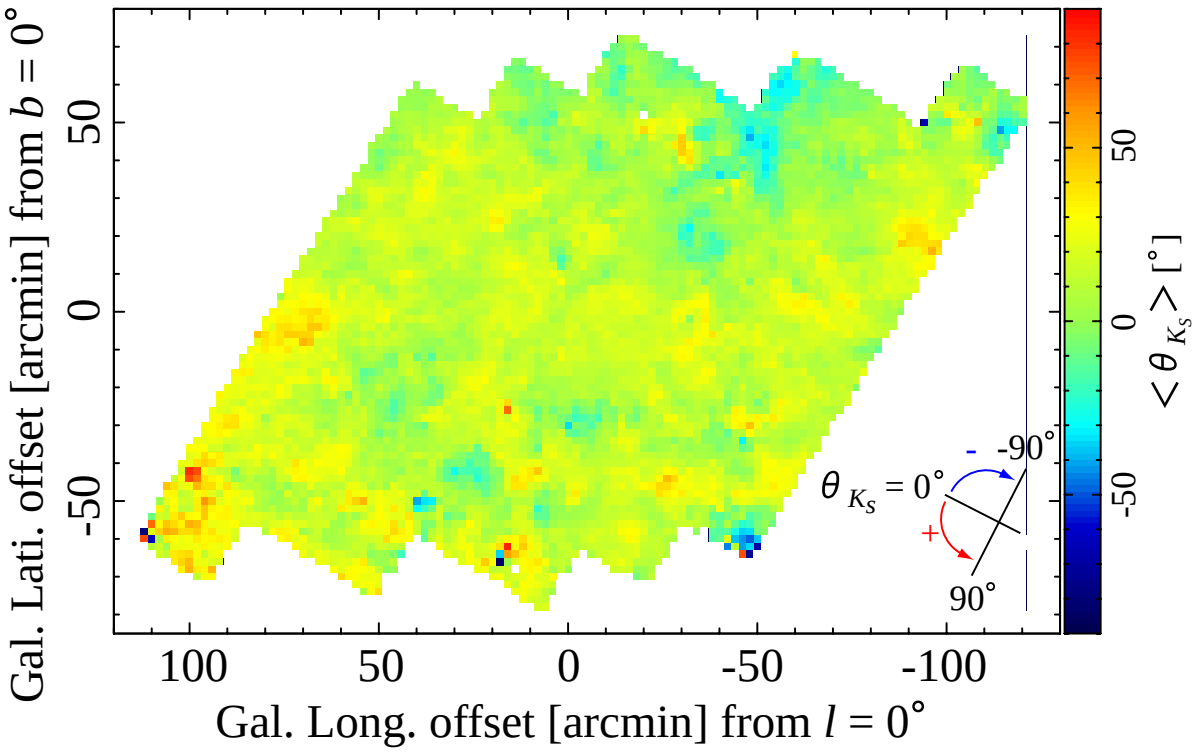

Figure 4.9: Map of θ_{K_S}. Each pixel represents a mean of θ_{K_S} for the bulge sources with $\delta p_{K_S} \leq 1\%$ and $\delta\theta_{K_S} \leq 10^\circ$ in each cell with a size of $2' \times 2'$. The white pixels include no sources and means cannot be measured.

In the relations between polarization degrees and colors for the sources (Fig. 4.10), two distinct populations corresponding to the disk and bulge sources can be also seen. The disk sources have average polarization degrees of 2.1%, 1.2%, and 0.8% in the J, H, and K_S bands, respectively. Meanwhile, the bulge sources extend redward and represent correlations between p and $H - K_S$ in all the bands; p increases with increasing $H - K_S$. The slopes of the correlations correspond to the polarization efficiency (§4.2.4), and the difference of the slopes between the bands is due to the wavelength dependence of interstellar polarization (§5.2).

In Figure 4.11, we show a map of the mean $\langle p_{K_S} \rangle$, as $E(H - K_S)$ and θ_{K_S}. In a similar way to the spatial variation of $E(H - K_S)$ (Fig. 4.6), that of p_{K_S} is dependent on Galactic latitude. Most of cells in which $\langle p_{K_S} \rangle$ exceeds 5% are close to the Galactic plane, while in cells at higher Galactic latitude $\langle p_{K_S} \rangle$ is only 1−2% or less. However, the spatial variations of $E(H - K_S)$ and p do not completely coincide with each other. This is more obvious in the form of the spatial variation of the polarization efficiency (§4.2.4).

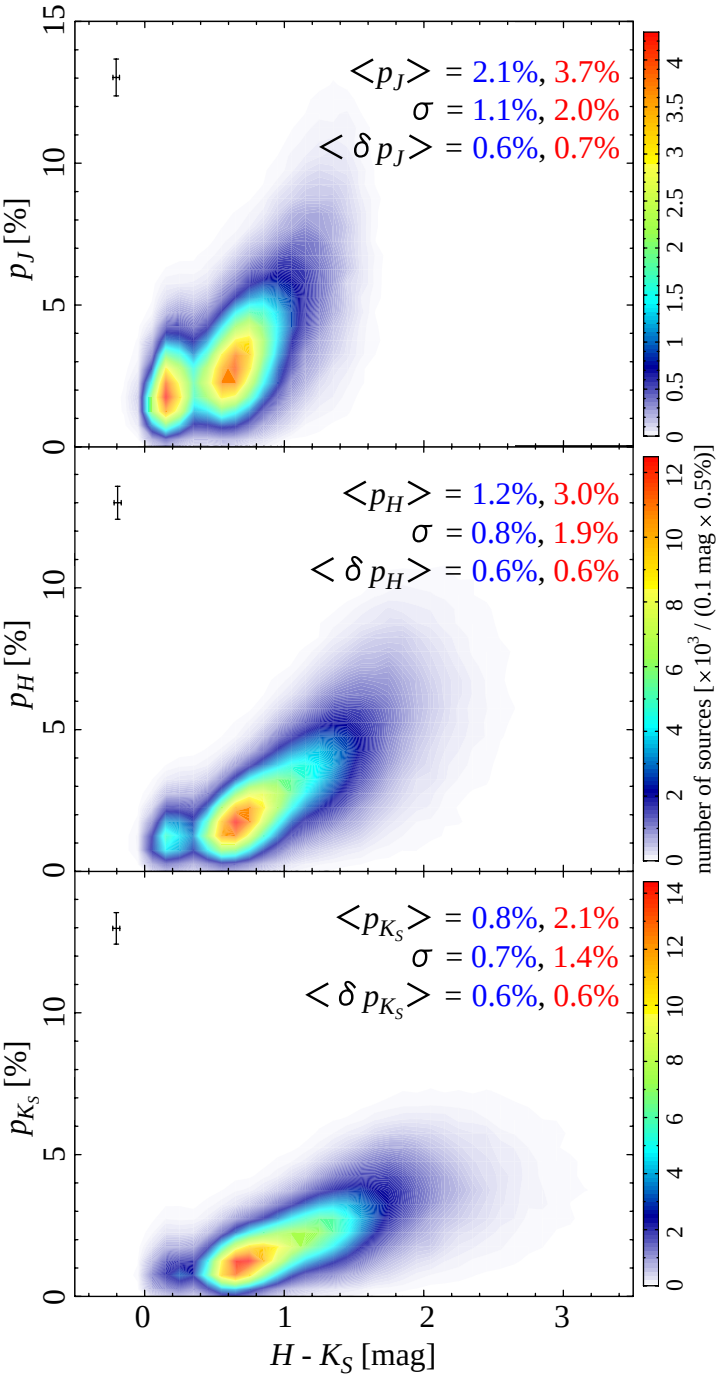

Figure 4.10: Degrees of polarization p vs. $H - K_S$ colors for the sources with $\delta p \leq 1\%$ in the J (*top*), H (*middle*), and K_S (*bottom*) bands. The means, standard deviations, and average errors of p for the disk (*blue*) and bulge (*red*) sources are shown at the upper right of the panels. The upper left crosses in each panel denote the average errors of p and $H - K_S$ for the sources.

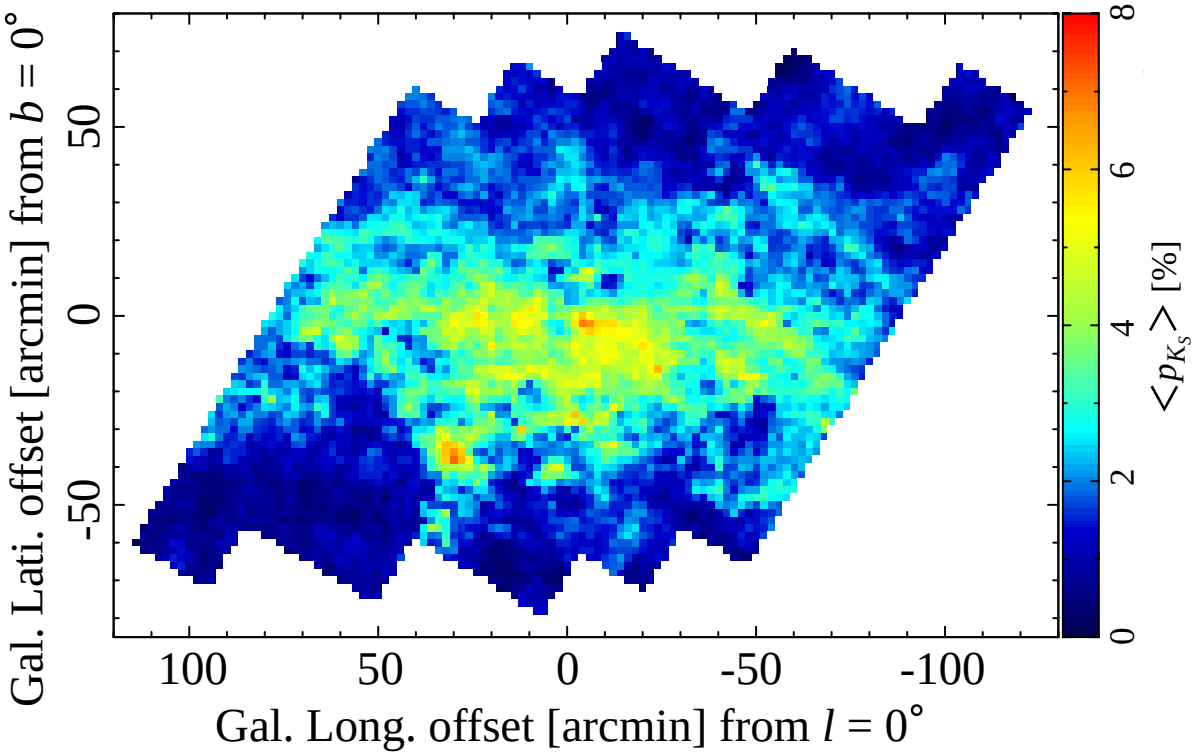

Figure 4.11: Map of p_{K_S}. Each pixel represents a mean of p_{K_S} for the bulge sources with $\delta p_{K_S} \leq 1\%$ in each cell with a size of $2' \times 2'$.

4.2.4 Polarization Efficiency

Starlight passes through the intervening ISM, which causes extinction and polarization; starlight from the disk sources passes through the ISM close to us, whereas starlight from the bulge ones through the ISM between the GC and us. From $p/E(H-K_S)$ for the disk and bulge sources, we examine the polarization efficiency of the ISM close to us and that between the GC and us.

Combining means of $E(H-K_S)$ and p, we calculate the means $\langle p \rangle / \langle E(H-K_S) \rangle$ for the disk sources to be 19.1% / mag, 10.0% / mag, and 6.2% / mag in the J, H, and K_S bands, respectively (dash-dotted lines in Fig. 4.12). The average polarization efficiency of the ISM close to us is about two-thirds of the upper limits [$p_J/E(H-K_S) = 25.0\%$ / mag, $p_H/E(H-K_S) = 14.5\%$ / mag, and $p_{K_S}/E(H-K_S) = 9.0\%$ / mag] estimated from $p_{\rm max}/E(B-V) = 9.0\%$ / mag[1].

[1]We extend the upper limit at the optical wavelengths by Serkowski et al. (1975) to the NIR wavelengths. We convert color excess $E(B-V)$ to $E(H-K_S)$ by assuming that $E(H-K)$ of the interstellar extinction law by Rieke & Lebofsky (1985) is identical to $E(H-K_S)$; $E(B-V)/E(H-K_S) = 5.14$. For degree of polarization, first $p_{\rm max}$ is converted to p_K (the value at 2.2 μm) using the average ratio $\langle p_{\rm max}/p_K \rangle = 5.4$, which is calculated by Jones (1989) from the data in Wilking et al. (1980). Then p_{K_S} are extrapolated from p_K following a power law $p_\lambda \propto \lambda^{-1.76}$, and p_J and p_H are calculated from p_{K_S} using $p_H/p_J = 0.581$ and $p_{K_S}/p_H = 0.620$ (§5.2).

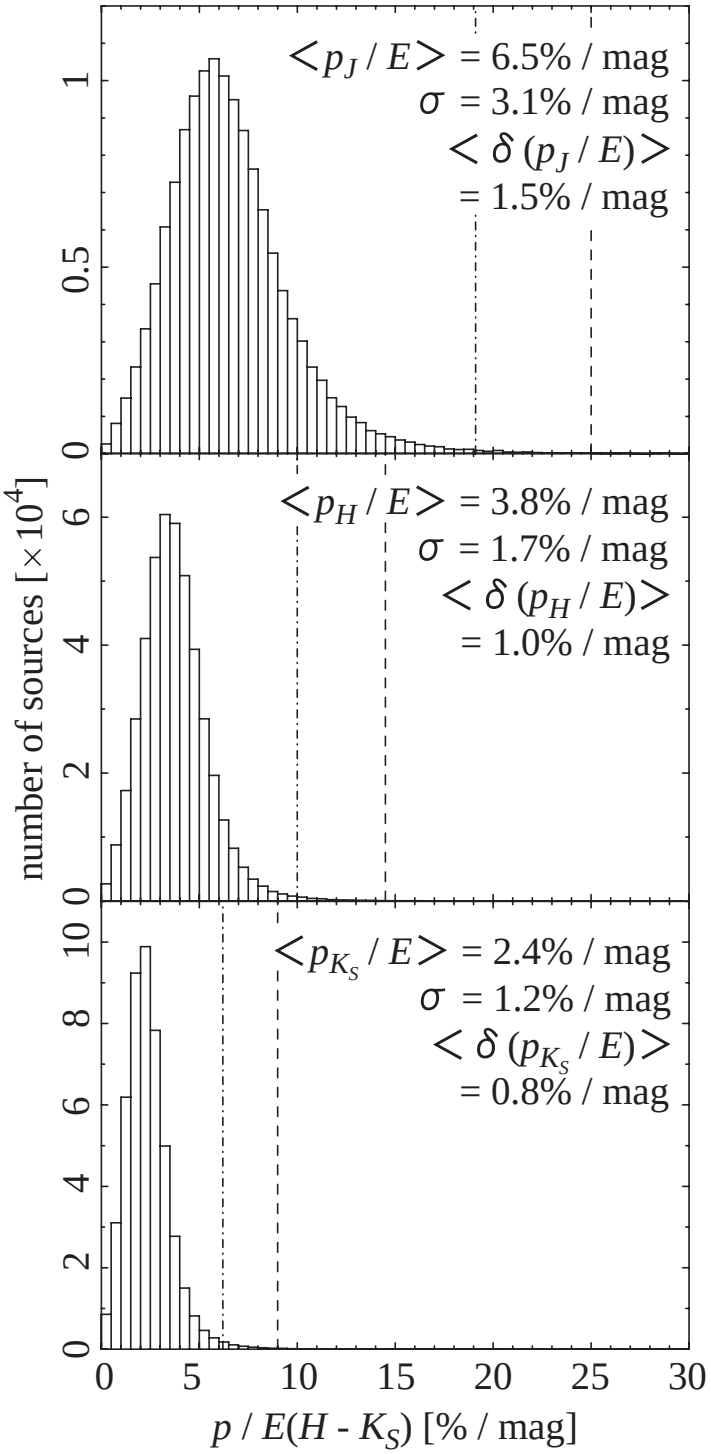

Figure 4.12: Histograms of the polarization efficiency $p/E(H-K_S)$ for the bulge sources with $\delta p \leq 1\%$ in the J (*top*), H (*middle*), and K_S (*bottom*) bands. Dashed lines in each panel are $p_J/E(H-K_S) = 25.0\%$ / mag, $p_H/E(H-K_S) = 14.5\%$ / mag, and $p_{K_S}/E(H-K_S) = 9.0\%$ / mag, which correspond to $p_{\max}/E(B-V) = 9.0\%$ / mag (Serkowski et al. 1975). The means, standard deviations, and average errors of $p/E(H-K_S)$ for the bulge sources are shown at the upper right of the panels. The dash-dotted lines in each panel show the means of $p/E(H-K_S)$ for the disk sources with $\delta p \leq 1\%$.

We show histograms of $p/E(H-K_S)$ for the bulge sources in Figure 4.12. $p/E(H-K_S)$ for most of the bulge sources falls below the estimated upper limits. The means of $p/E(H-K_S)$ for the bulge sources are 6.5% / mag, 3.8% / mag, and 2.4% / mag in the J, H, and K_S bands, respectively. The average polarization efficiency of the ISM between the GC and us is no more than about a quarter of the estimated upper limits. Moreover, it is lower than that of the ISM close to us, by a factor of about three. Kobayashi et al. (1983) also suggested that the polarization efficiency toward the GC is considerably lower than that obtained in the solar neighborhood based on K band polarimetry toward the GC ($20' \times 20'$).

As other parameters, we draw a map of $p_{K_S}/E(H-K_S)$ for the bulge sources in Figure 4.13. The Galactic structure, like the Galactic plane, is not recognized in the spatial variation of $p_{K_S}/E(H-K_S)$. The mean $\langle p_{K_S}/E(H-K_S)\rangle$ continuously changes from line-to-line of sight, and its amplitude is a factor of about five (from about 1 to 5% / mag).

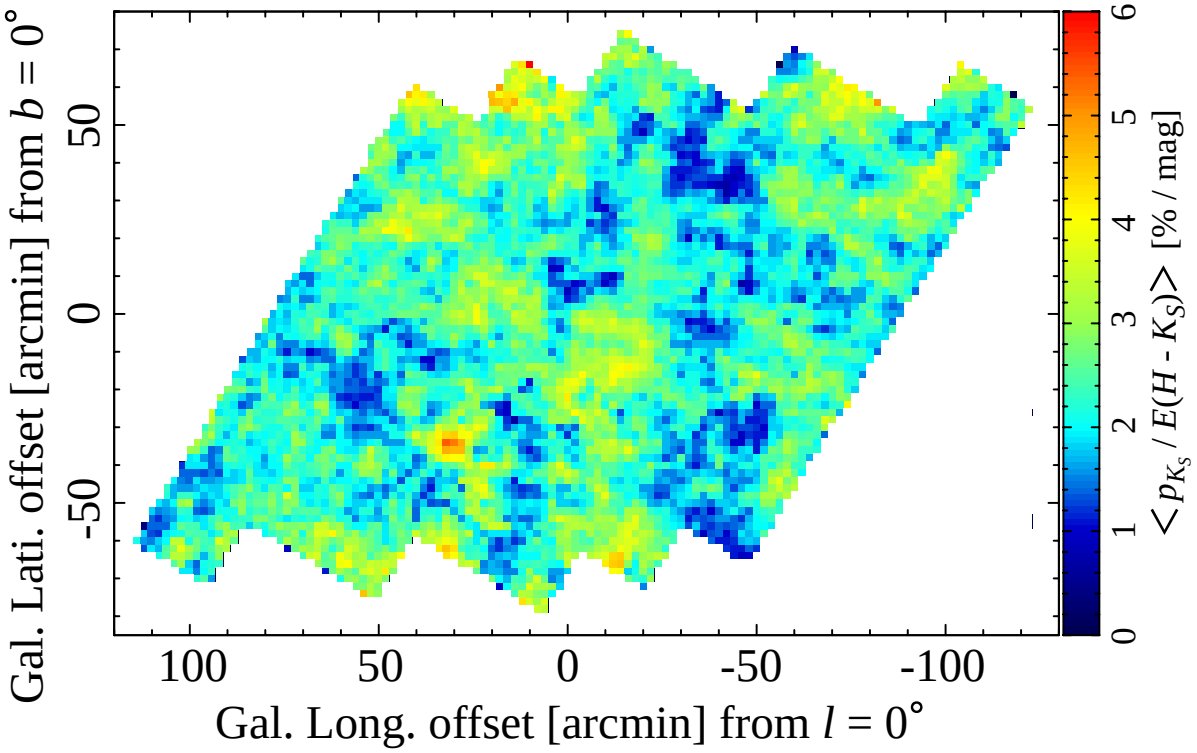

Figure 4.13: Map of $p_{K_S}/E(H-K_S)$. Each pixel represents a mean of $p_{K_S}/E(H-K_S)$ for the bulge sources with $\delta p_{K_S} \leq 1\%$ in each cell with a size of $2' \times 2'$.

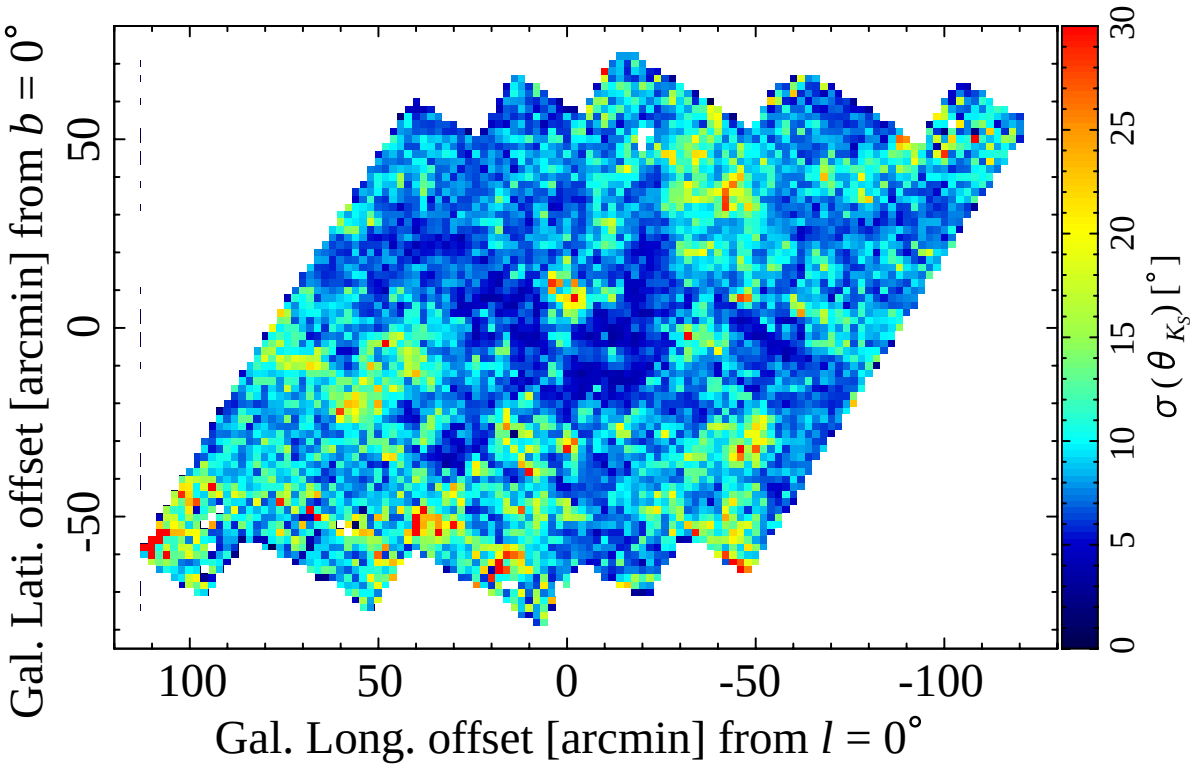

Figure 4.14: Map of $\sigma(\theta_{K_S})$. Each pixel represents a dispersion of θ_{K_S} for the bulge sources with $\delta p_{K_S} \leq 1\%$ and $\delta\theta_{K_S} \leq 10^\circ$ in each cell with a size of $2' \times 2'$. The cells including one or no source(s) are drawn by white pixels.

Dispersions of position angles $\sigma(\theta_{K_S})$ anticorrelate with $\langle p_{K_S}/E(H-K_S)\rangle$. We calculate $\sigma(\theta_{K_S})$ for the bulge sources with $\delta\theta_{K_S} \leq 10^\circ$ in each cell and show its map in Figure 4.14. Some cells show $\sigma(\theta_{K_S})$ significantly larger than the average error of θ_{K_S} for the bulge sources (5.°7). In comparison between the spatial variations of $p_{K_S}/E(H-K_S)$ and $\sigma(\theta_{K_S})$ (Figs. 4.13 and 4.14), we can see a tendency that the larger $\sigma(\theta_{K_S})$, the lower $\langle p_{K_S}/E(H-K_S)\rangle$, and vice versa. This tendency is shown in the relation between $\langle p_{K_S}/E(H-K_S)\rangle$ and $\sigma(\theta_{K_S})$ (Fig. 4.15). The medians of $\langle p_{K_S}/E(H-K_S)\rangle$ in each bin of $\sigma(\theta_{K_S})$ (2° in width) show the highest value at the bin of $\sigma(\theta_{K_S}) = 2$–4°, decrease with increasing $\sigma(\theta_{K_S})$, and then become almost flat toward bins of larger $\sigma(\theta_{K_S})$.

4.3 Discussion

4.3.1 Low Polarization Efficiency and Its Spatial Variation

As for the polarization efficiency of the ISM between the GC and us, our results show (a) low efficiency compared to that of the ISM close to us (Fig. 4.12), (b) the spatial variation throughout the analyzed area (Fig. 4.13), and (c) the anticorrelation with the dispersions of position angles (Fig. 4.15). For an explanation of our results, we consider (1) the different directions of magnetic fields along the line-of-sight.

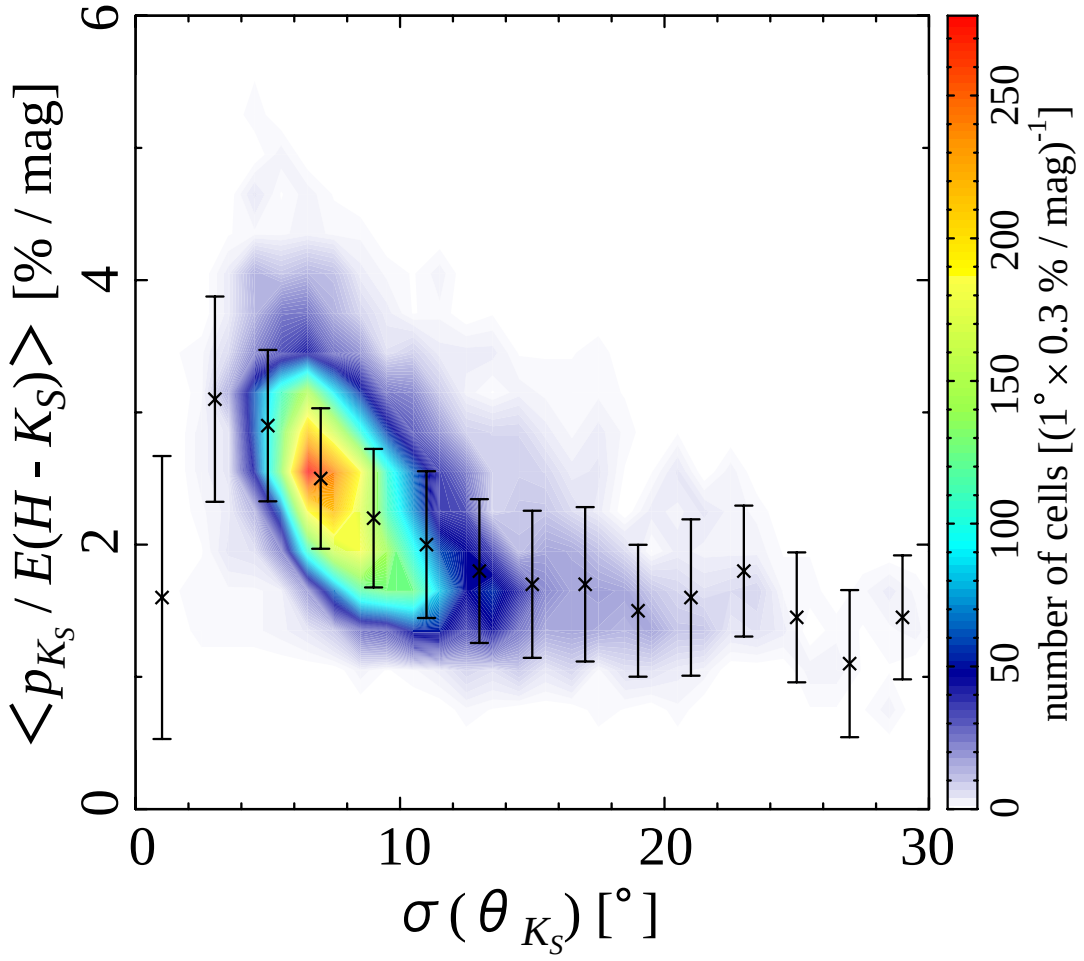

Figure 4.15: $\langle p_{K_S}/E(H-K_S)\rangle$ vs. $\sigma(\theta_{K_S})$ for the cells including more than two sources. The crosses and error bars represent medians and standard deviations of $\langle p_{K_S}/E(H-K_S)\rangle$ in 2° width bins of $\sigma(\theta_{K_S})$.

The interstellar magnetic field consists of the uniform and random components (Heiles 1987, 1996). The uniform component corresponds to the Galactic magnetic field, which runs almost parallel to the spiral arms (Heiles 1996; Han 2009). The random component deviates the magnetic field direction in each ISM from the direction of the Galactic magnetic field. Due to the differences of the magnetic field directions, superposition of the ISM along the line-of-sight lowers the polarization efficiency (depolarization). Since the ISM between the GC and us generally consists of more ISM with different magnetic field directions, depolarization would be larger and the polarization efficiency should be lower than the ISM close to us (result of (a)). To explain the observed dispersions of position angles (Fig. 4.14), nonuniform structures of the magnetic field and/or density with a size of less than 2′ (cell size) are needed. Gosling et al. (2006, 2009) detected such nonuniform density distribution with a size of 5−15″. Larger (smaller) differences of the magnetic field directions would cause lower (higher) polarization efficiency and a larger (smaller) dispersion of position angles (results of (b) and (c)).

Next, we discuss the polarization efficiency in relation to other factors; (2) the polarizing grain properties such as their shape, size distribution, and composition, and (3) the degree of grain alignment influenced by physical conditions in the ISM (density and temperature of gas, strengths of magnetic field and radiation field) also affect the polarization efficiency. As for (2), since the wavelength dependence of polarization shows little or no spatial variation (§5.2), we infer that the polarizing grain properties are almost uniform throughout the analyzed area. As for (3), in dense clouds, the degree of grain alignment may decline with increasing gas density, and the polarization efficiency becomes lower (e.g., Gerakines et al. 1995). However, even if the degree of grain alignment declines, it does not cause the observed dispersions of position angles (Fig. 4.14). In contrast, the differences of the magnetic field directions along the line-of-sight can explain our results.

4.3.2 Magnetic Field Strength Ratio of the Random to the Uniform Component

For the observed relation between extinction and degree of polarization, Jones et al. (1992) constructed two models depending on the geometry of magnetic fields along the line-of-sight. One is the two-component model, and the other is the wave model. In the two-component model, the magnetic field direction is determined by a combination of the uniform and random components in each optical depth length (segment); in each length $\Delta\tau_{K_S} = 0.1$, the random component of the magnetic field decorrelates. A segment corresponds to a part of the diffuse ISM (with typical length of a few tens of a pc) or a dense cloud (a fraction of a pc). Fitting the model to the data, they concluded that the uniform and random components have equal energy density; this is their case of $\sigma_{\boldsymbol{B}}/\boldsymbol{B} = 0.6$, where $\sigma_{\boldsymbol{B}}$ is the dispersion of the random component and $\boldsymbol{B}$ is the strength of the uniform component. We compare our data with their model results. The bulge sources show relatively lower polarization efficiency than their best-fit result and almost lie between their results with $\sigma_{\boldsymbol{B}}/\boldsymbol{B} = 0.6$ and $\sigma_{\boldsymbol{B}}/\boldsymbol{B} = 1.2$ in the model (Fig. 4.16*a*). The polarization efficiency toward the GC measured by Kobayashi et al. (1983) as shown by the red points is also lower than their best-fit result. These indicate that the energy density of the random component is higher than that of the uniform component of the magnetic field toward the GC.

In the wave model, a magnetic field is described as a wave. The amplitude of the wave determines the extent to which the magnetic field direction in each segment fluctuates along the line-of-sight. They fitted the model to the data, also concluding that the energy density of the magnetic field is in equipartition with the kinematic energy density of moving clouds; this is their case of $V_{\rm rms}/V_{\rm A} = 1.0$, where $V_{\rm rms}$ is the rms motion of individual clouds of gas and dust attached to the magnetic field lines and $V_{\rm A}$ is the Alfvén speed. Compared to their best-fit result with $V_{\rm rms}/V_{\rm A} = 1.0$, the bulge sources show relatively lower polarization efficiency, most of which are distributed between their results with $V_{\rm rms}/V_{\rm A} = 1.0$ and $V_{\rm rms}/V_{\rm A} = 1.5$ in the model (Fig. 4.16*b*). This means that the turbulent energy density is higher than the magnetic energy density in the ISM toward the GC.

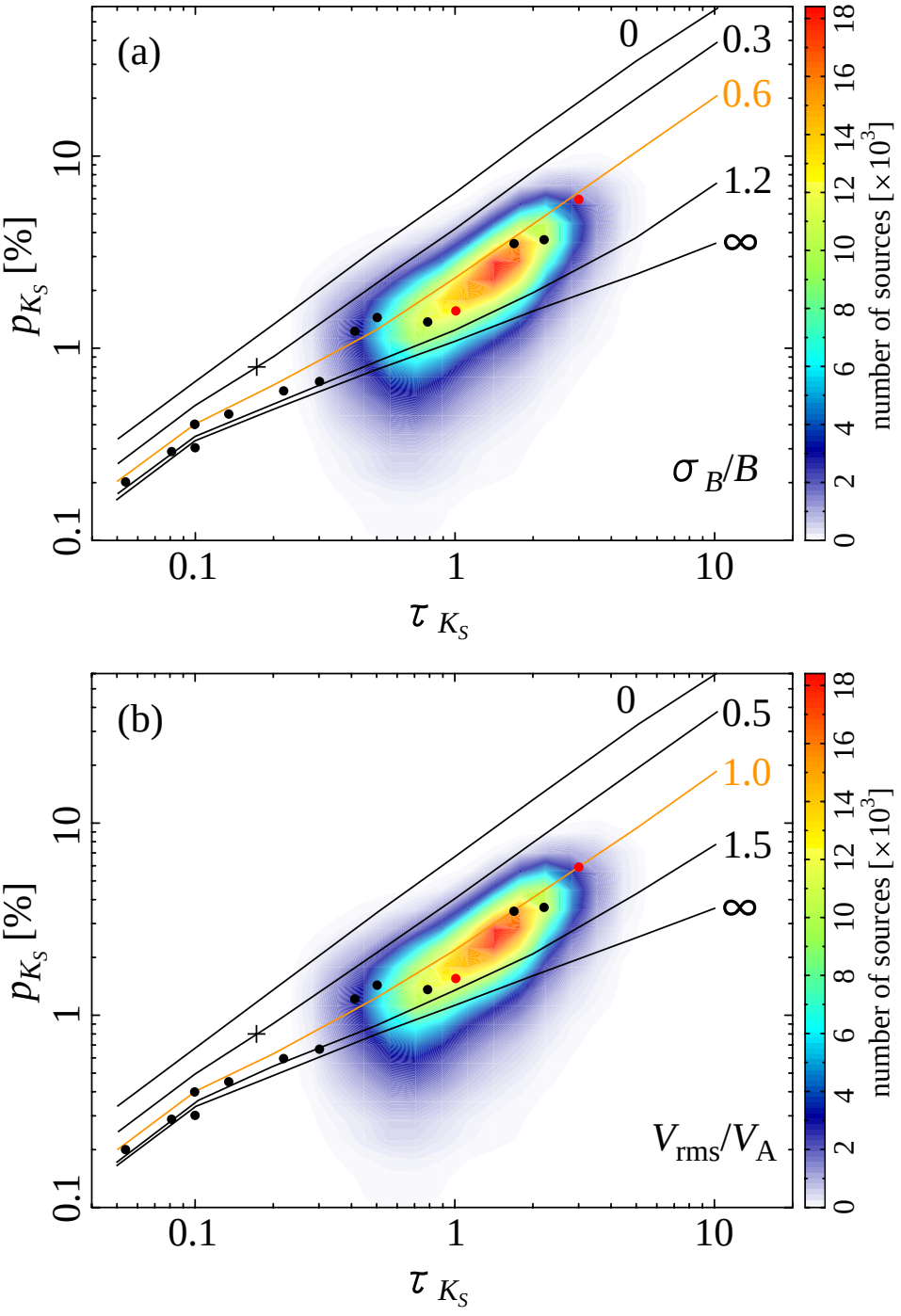

Figure 4.16: Degrees of polarization p_{K_S} vs. optical depth τ_{K_S} for the bulge sources with $\delta p_{K_S} \leq 1\%$. The cross indicates the means of p_{K_S} and τ_{K_S} for the disk sources with $\delta p_{K_S} \leq 1\%$. The lines show (a) the results for five values for the parameter $\sigma_{\boldsymbol{B}}/\boldsymbol{B}$ in the two-component model and (b) those for $V_{\rm rms}/V_{\rm A}$ in the wave model by Jones et al. (1992). The orange lines are their best-fit results. The points show average polarization seen toward several regions at various optical depth intervals and the central regions of several normal spiral galaxies (Jones et al. 1992, and references therein), of which red points correspond to the measurements toward the GC by Kobayashi et al. (1983).

The comparison in either case suggests higher magnetic field strength of the random component against that of the uniform component between the GC and us as indicated in the solar neighborhood (Heiles 1996; Fosalba et al. 2002). The gas motions such as turbulence, gravitational contraction of dense clouds, expansion of H II regions, and supernova explosions distort the magnetic field and produce its random component. These processes would be strongly active in the GC (see e.g., a review by Morris & Serabyn 1996), and contribute to higher magnetic field strength ratio of the random to the uniform component toward the GC. The processes cause relatively large deviations of the magnetic field directions from the direction of the uniform component (the Galactic magnetic field). Low polarization efficiency and its spatial variation would be explained by superposition of the diffuse ISM and dense clouds with such deviations of the magnetic field directions along the line-of-sight.

4.4 Conclusion

We have investigated the magnetic field toward the GC based on the interstellar polarization efficiency and position angles measured from the survey data. The results are as follows:

(1) The polarization efficiency of the ISM between the GC and us is lower than that of the ISM close to us, by a factor of about three on average.

(2) The spatial variation of the polarization efficiency does not depend on the Galactic structure in contrast with those of color excess and degree of polarization.

(3) Position angles are almost parallel to the Galactic plane, suggesting that the magnetic field between the GC and us has the longitudinal configuration and connects to the toroidal magnetic field in the GC.

(4) The dispersions of position angles increase with decreasing the polarization efficiency. It is likely that the polarization efficiency is caused to be low by the different directions of magnetic fields along the line-of-sight (depolarization).

(5) The comparison of our data with the models by Jones et al. (1992) suggests that the random component has higher strength than the uniform component of the magnetic field.

Bibliography

Bessell, M. S., & Brett, J. M. 1988, PASP, 100, 1134

Chuss, D. T., Davidson, J. A., Dotson, J. L., Dowell, C. D., Hildebrand, R. H., Novak, G., & Vaillancourt, J. E. 2003, ApJ, 599, 1116

Creese, M., Jones, T. Jay., Kobulnicky, H. A. 1995, AJ, 110, 268

Fosalba, P., Lazarian, A., Prunet, S., & Tauber, J. A. 2002, ApJ, 564, 762

Gerakines, P. A., Whittet, D. C. B., & Lazarian, A. 1995, ApJ, 455, 171

Gosling, A. J., Blundell, K. M., & Bandyopadhyay, R. 2006, ApJ, 640, L171

Gosling, A. J., Bandyopadhyay, R. M., & Blundell, K. M. 2009, MNRAS, 366

Han, J. L. 2009, in IAU Symp. 259. Cosmic Magnetic Fields: From Planets, to Stars and Galaxies, ed. K. G. Strassmeir, A. G. Kosovichev, & J. E. Beckman (Dordrecht: Kluwer), 455

Heiles, C. 1987, in Interstellar Processes, ed. D. J. Hollenbach & H. A. Thronson (Dordrecht: Reidel), 171

Heiles, C. 1996, in Polarimetry of the Interstellar Medium, ed. W. G. Roberge & D. C. B. Whittet (San Francisco: ASP), 457

Heiles, C. 2000, AJ, 119, 923

Jones, T. J. 1989, ApJ, 346, 728

Jones, T. J., Klebe, D., & Dickey, J. M. 1992, ApJ, 389, 602

Kobayashi, Y., Okuda, H., Sato, S., Jugaku, J., & Dyck, H. M. 1983, PASJ, 35, 101

Kobayashi, Y., Jugaku, J., Okuda, H., Sato, S., & Nagata, T. 1986, Ap&SS, 119, 135

Koornneef, J. 1983, A&A, 128, 84

Lada, C. J., Lada, E. A., Clemens, D. P., & Bally, J. 1994, ApJ, 429, 694

Mathewson, D. S., & Ford, V. L. Mem. R. Astron. Soc., 74, 139

Martin, P. G. 1974, ApJ, 187, 461

Morris, M., & Serabyn, E. 1996, ARA&A, 34, 645

Myers, P. C., & Goodman, A. A. 1991, ApJ, 373, 509

Nishiyama, S., Nagata, T., Kusakabe, N., Matsunaga, N., Naoi, T., Kato, D., Nagashima, C., Sugitani, K., Tamura, M., Tanabe, T., & Sato, S. 2006, ApJ, 638, 839

Nishiyama, S., Tamura, M., Hatano, H., Kanai, S., Kurita, M., Sato, S., Matsunaga, N., Nagata, T., Nagayama, T., Kandori, R., Kusakabe, N., Sato, Y., Hough, J. H., Sugitani, K., & Okuda, H. 2009a, ApJ, 690, 1648

Novak, G., Chuss, D. T., Renbarger, T., Griffin, G. S., Newcomb, M. G., Peterson, J. B., Loewenstein, R. F., Pernic, D., & Dotson, J. L. 2003, ApJ, 583, L83

Rieke, G. H., & Lebofsky, M. J. 1985, ApJ, 288, 618

Serkowski, K., Mathewson, D. L., & Ford, V. L. 1975, ApJ, 196, 261

Wainscoat, R. J., Cohen, M., Volk, K., Walker, H. J., & Schwartz, D. E. 1992, ApJS, 83, 111

Wilking, B. A., Lebofsky, M. J., Kemp, J. C., Martin, P. G., & Rieke, G. H. 1980, ApJ, 235, 905

Chapter 5

Wavelength Dependence of Interstellar Polarization toward the Galactic Center

5.1 Introduction

After the discovery of interstellar polarization, polarization of numerous stars has been measured through multiple passbands. Behr (1959) and Gehrels (1960) found that degree of polarization has systematic variations with wavelengths. Based on polarimetric observations of hundreds of stars over 0.3−1.0 μm, Coyne et al. (1974) and Serkowski et al. (1975) showed that polarization p_λ has a convex curve with a peak $p_{\max}$, typically occurring at around $\lambda_{\max} = 0.55$ μm (Fig. 5.1) and that the wavelength dependence of polarization at the optical wavelengths is well described by the following empirical law (Serkowski's law):

$$p_\lambda / p_{\max} = \exp[-K \ln^2(\lambda_{\max}/\lambda)]$$

where K, which determines the full width of the curve, is 1.15.

Dyck & Jones (1978) found that polarization decreases less rapidly at the NIR wavelengths (1.25−2.2 μm) than predicted by Serkowski's law. From NIR polarimetry of 33 stars, Wilking et al. (1980, 1982) showed a broadening (narrowing) of the polarization curve as $\lambda_{\max}$ decreases (increases), and revised Serkowski's law by treating K as a function of $\lambda_{\max}$, according to the relation (Serkowski-Wilking's law):

$$K = (-0.10 \pm 0.05) + (1.86 \pm 0.09)\lambda_{\max}$$

(Fig. 5.2). Whittet et al. (1992) slightly revised the empirical linear relationship [modified Serkowski's law; $K = (0.01 \pm 0.05) + (1.66 \pm 0.09)\ \lambda_{\max}$] from polarimetric observations of 105 stars in the wavelength range of 0.36−2.0 μm.

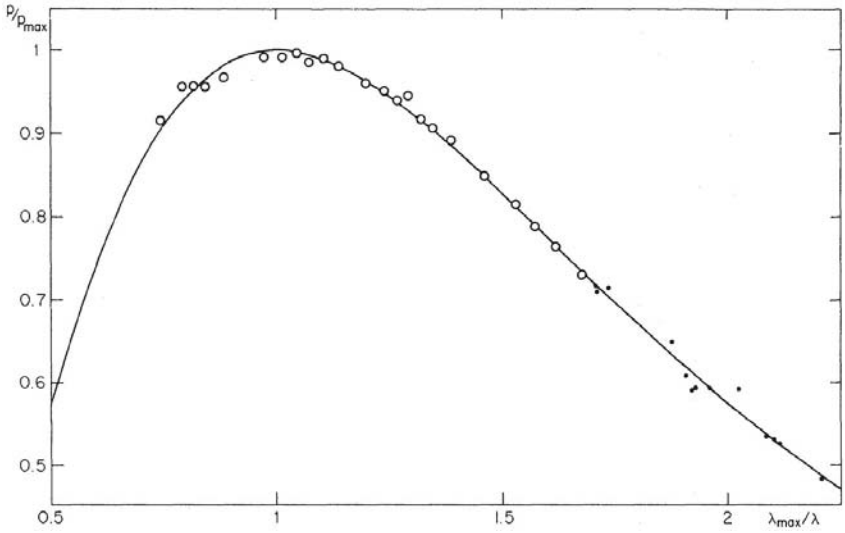

Figure 5.1: The normalized wavelength dependence of interstellar polarization derived from the observations with the Siding Spring multichannel polarimeter-photometer (Fig. 3 of Serkowski et al. 1975). The solid line is calculated from Serkowski's law for $K = 1.15$. Every open circle is based on 20 stars, while each dot represents the observations of an individual stars with a particular filter.

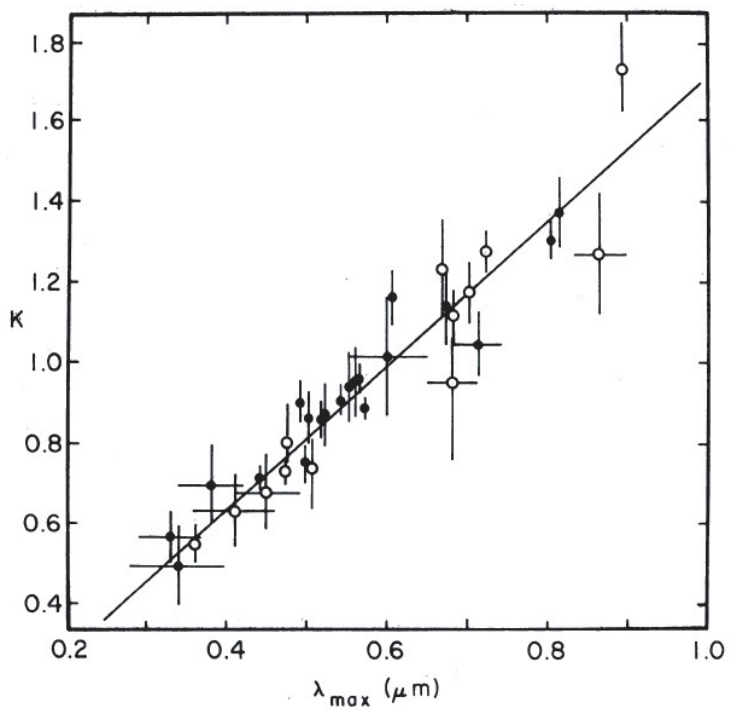

Figure 5.2: A plot of K vs. $\lambda_{\max}$ for 33 stars (Fig. 1 of Wilking et al. 1982). One-sigma confidence intervals for K are indicated for all stars; uncertainties in $\lambda_{\max}$ equal to or in excess of 0.03 μm are also shown. Also plotted are the results of the linear-squares regression performed on 32 stars.

Subsequent measurements at longer wavelengths (3−5 μm) showed that polarization exhibits significant excess compared to the extrapolation by Serkowski-Wilking's law (Fig. 5.3; Nagata 1990; Martin & Whittet 1990; Martin et al. 1992). They suggested that the wavelength dependence of polarization from 1.25 to 2.2 μm is represented by a power law:

$$p_\lambda \propto \lambda^{-\beta}$$

with β of 1.6−2.0. The wavelength dependence of interstellar *extinction* is also represented by a power law with the index α at the NIR wavelengths. The value of α is 1.6−2.0, which is close to that of β (Draine 2003; Nishiyama et al. 2006). This suggests that dust grains responsible for NIR extinction are well aligned and have similar optical properties with respect to wavelengths.

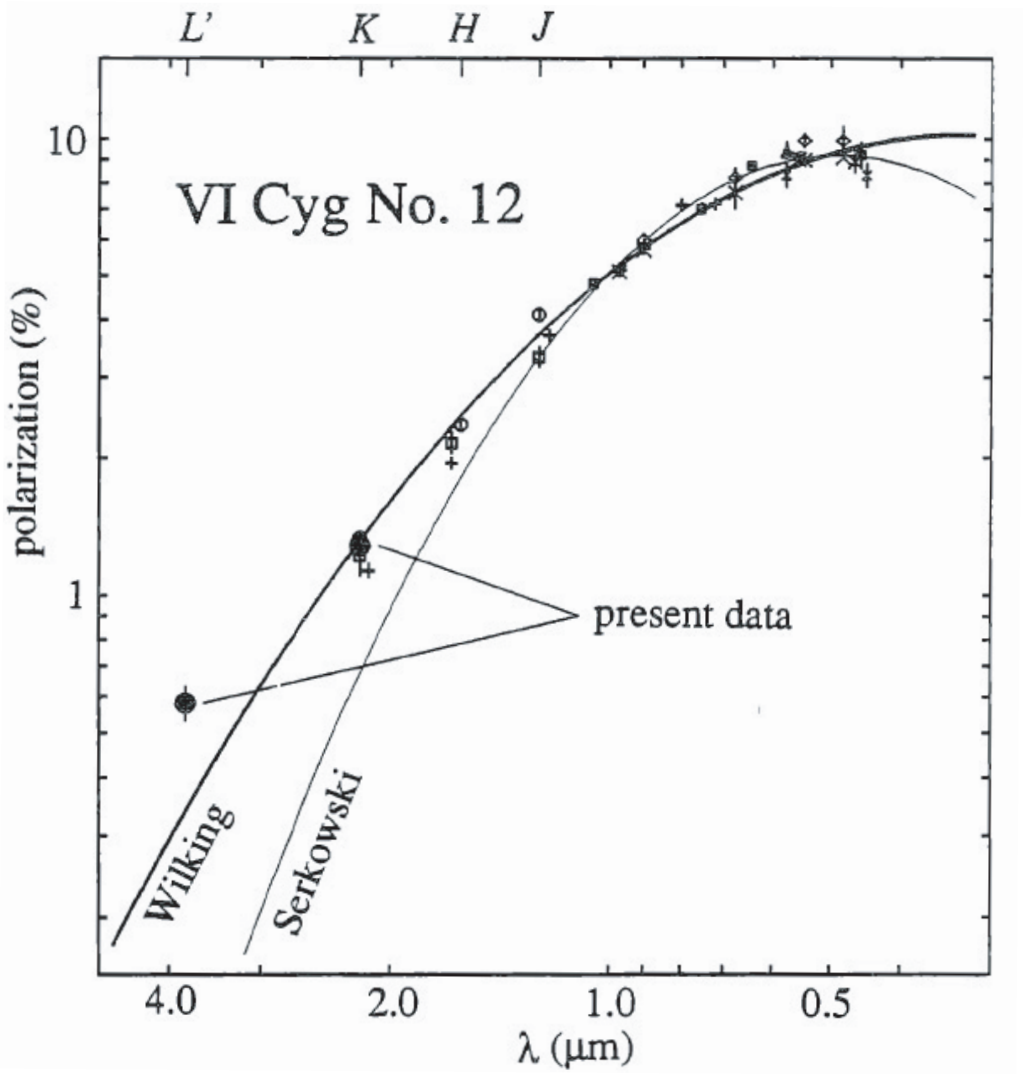

Figure 5.3: An example (VI Cyg No. 12) of the observed polarization and Serkowski's (thin line) and Serkowski-Wilking's (thick line) empirical formulae (Fig. 1 of Nagata 1990).

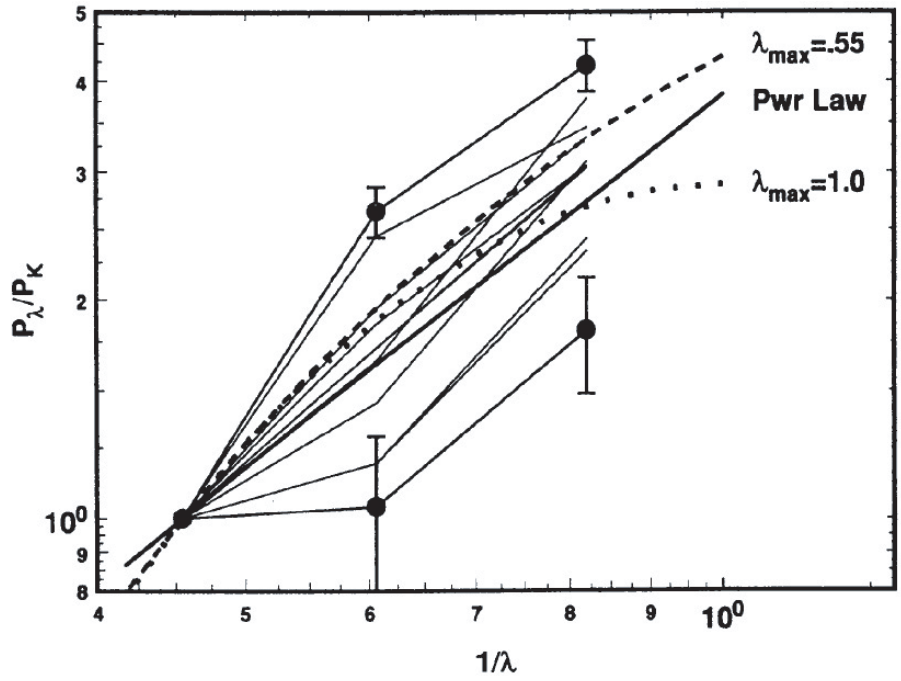

Figure 5.4: The normalized wavelength dependence of the polarization from 1−2.2 μm for all of the stars with K polarimetry and a signal to noise of greater than 4 to 1 in p_K (Fig. 10 of Creese et al. 1995).

However, Creese et al. (1995) suggest no systematic trend in the observed JHK polarization for about 10 reddened stars with respect to a power law (Fig. 5.4). In this chapter, we verify whether the wavelength dependence of polarization at NIR is really represented by a power law or not, and examine what types of dust grains cause the NIR polarization.

5.2 Results

We here examine the wavelength dependence of polarization. We select 3,651 sources detected under the criteria of $\delta p \leq 1\%$ and $p \geq 10\ \delta p$ in all the bands.

In Figure 5.5, the relation between p_J and p_H and that between p_H and p_{K_S} for the sources show good correlations with the mean slopes of 0.581 ± 0.004 and 0.620 ± 0.002, respectively (Table 5.1). The standard deviations, 0.076 and 0.047 for p_H/p_J and p_{K_S}/p_H, are comparable to the average errors, 0.055 and 0.063, suggesting that the standard deviations are mostly caused by the errors. Thus the wavelength dependence of polarization does not change significantly throughout the analyzed area (Fig. 3.1).

Assuming a power law ($p_\lambda \propto \lambda^{-\beta}$), and using the equations:

$$\beta_{JH} = -\frac{\ln(p_H/p_J)}{\ln(\lambda_H/\lambda_J)},$$

$$\beta_{HK_S} = -\frac{\ln(p_{K_S}/p_H)}{\ln(\lambda_{K_S}/\lambda_H)},$$

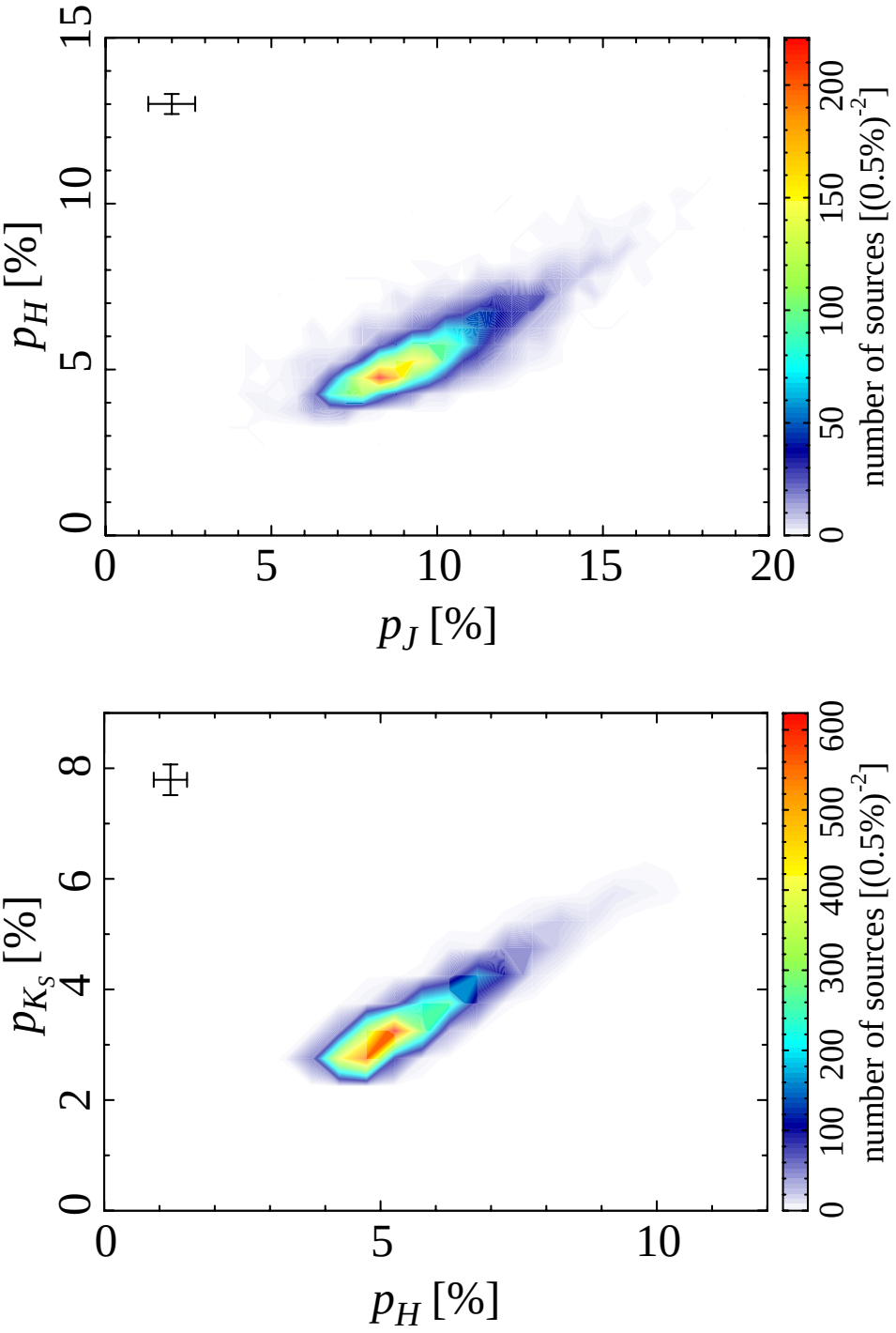

Figure 5.5: p_J vs. p_H (*top*) and p_H vs. p_{K_S} (*bottom*) for the sources that are detected in all the bands and with $\delta p \leq 1\%$ and $p \geq 10\ \delta p$. The upper left crosses in each panel denote the average errors of p.

Table 5.1: Wavelength Dependence of Polarization

	p_H/p_J	p_{K_S}/p_H	β_{JH}	β_{HK_S}
mean	0.581 ± 0.004	0.620 ± 0.002	2.08 ± 0.02	1.76 ± 0.01
standard deviation	0.076	0.047	0.46	0.25
average error	0.055	0.063	0.36	0.37

we calculate indices β_{JH} and β_{HK_S} for the sources. Histograms of β_{JH} and β_{HK_S} are shown in Figure 5.6. The means $\langle\beta_{JH}\rangle$ and $\langle\beta_{HK_S}\rangle$ for the sources are 2.08 ± 0.02 and 1.76 ± 0.01, respectively (Table 5.1). Although these values are not inconsistent with the empirical values of 1.6−2.0 (Nagata 1990; Martin & Whittet 1990; Martin et al. 1992), $\langle\beta_{JH}\rangle$ is larger than $\langle\beta_{HK_S}\rangle$. Degree of polarization decreases more slowly than a power law as the wavelength becomes longer from 1.25 to 2.14 μm; the wavelength dependence of polarization represents flattening toward longer wavelengths.

5.3 Discussion

In our results, $\langle\beta_{JH}\rangle$ is larger than $\langle\beta_{HK_S}\rangle$; the wavelength dependence of polarization shows flattening from 1.25 to 2.14 μm. In the previous studies (Wilking et al. 1980, 1982; Nagata 1990; Creese et al. 1995), similar flattening is also seen.

The value $\langle\beta_{JH}\rangle$ (2.08 ± 0.02) is close to the power law index α (1.99 ± 0.02) of the wavelength dependence of *extinction* toward the GC (Nishiyama et al. 2006). However $\langle\beta_{HK_S}\rangle$ (1.76 ± 0.01) is clearly below α, and flattening cannot be seen in the wavelength dependence of extinction from the H to K_S band. At longer wavelengths beyond 3 μm, both the wavelength dependence of polarization (Nagata 1990; Martin et al. 1992; Nagata et al. 1994) and extinction (Nishiyama et al. 2009b, and references therein) show flattening.

The wavelength dependence of polarization is determined by the polarizing grain properties such as shape, size distribution, and composition. From a comparison between observational data and theoretical models, the polarizing grain properties can be examined. Kim & Martin (1994, 1995a,b) fitted the model to modified Serkowski's law (Whittet et al. 1992) and a single power law ($\beta = 1.65$) for $\lambda = 1.64-5$ μm to examine the size (mass) distribution of dust grains. They obtained the most satisfactory result by adopting perfectly aligned oblate dust grains (axial ratio of 6:1). The resultant mass distribution has a peak at dust size of about 0.2 μm and a shoulder from the peak through dust size of 0.6 to 1.0 μm (Fig. 5.7). The shoulder is required to fit the infrared polarization with a power law behavior, which is the excess above the Serkowski's law. To explain the flattening (i.e., the excess above a power law behavior), greater numbers of such large-size dust grains would be necessary.

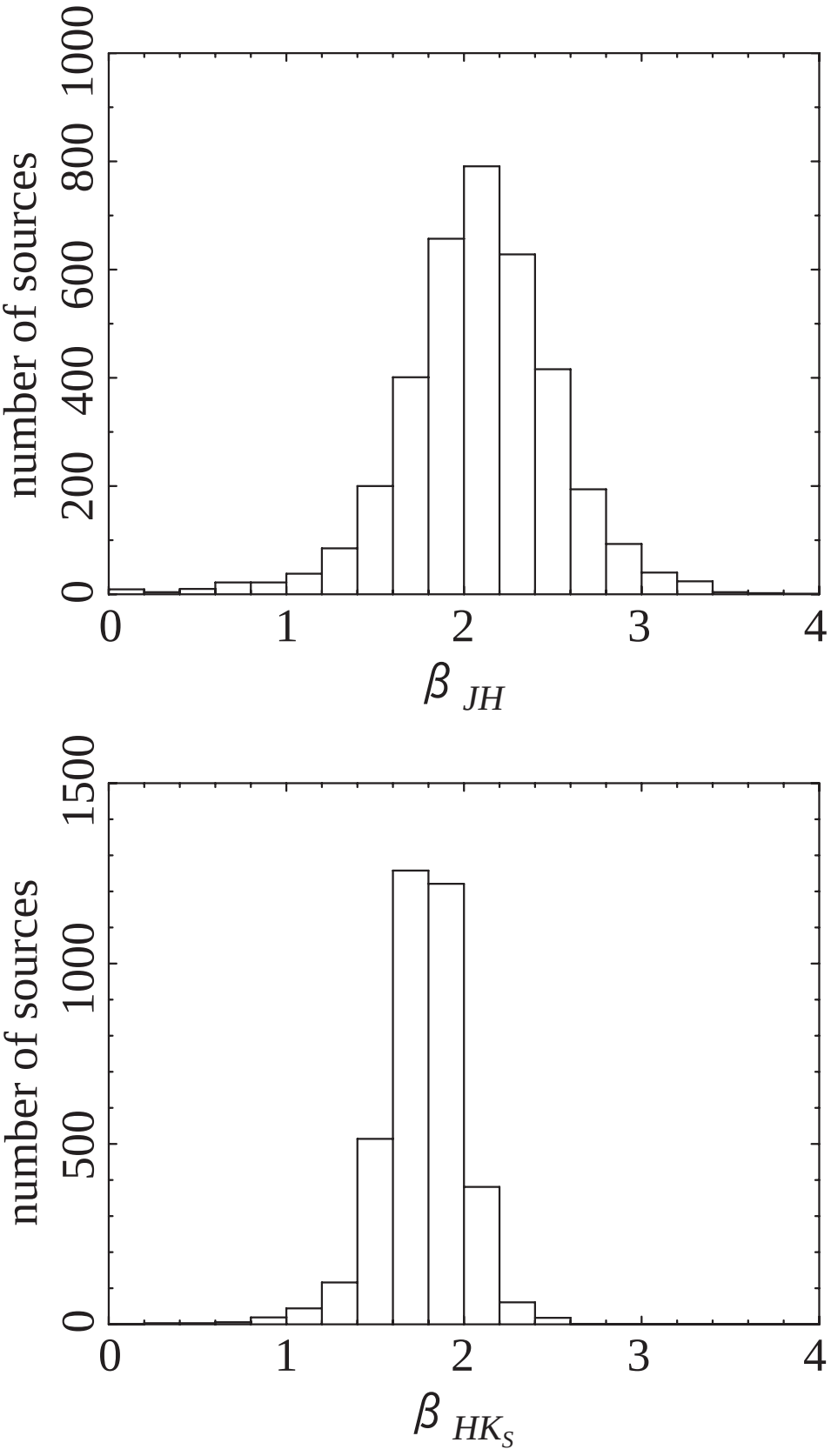

Figure 5.6: Histograms of β_{JH} (*top*) and β_{HK_S} (*bottom*) for the sources that are detected in all the bands and with $\delta p \leq 1\%$ and $p \geq 10\ \delta p$. The means, standard deviations, and average errors of β_{JH} and β_{HK_S} for the sources are shown in Table 5.1.

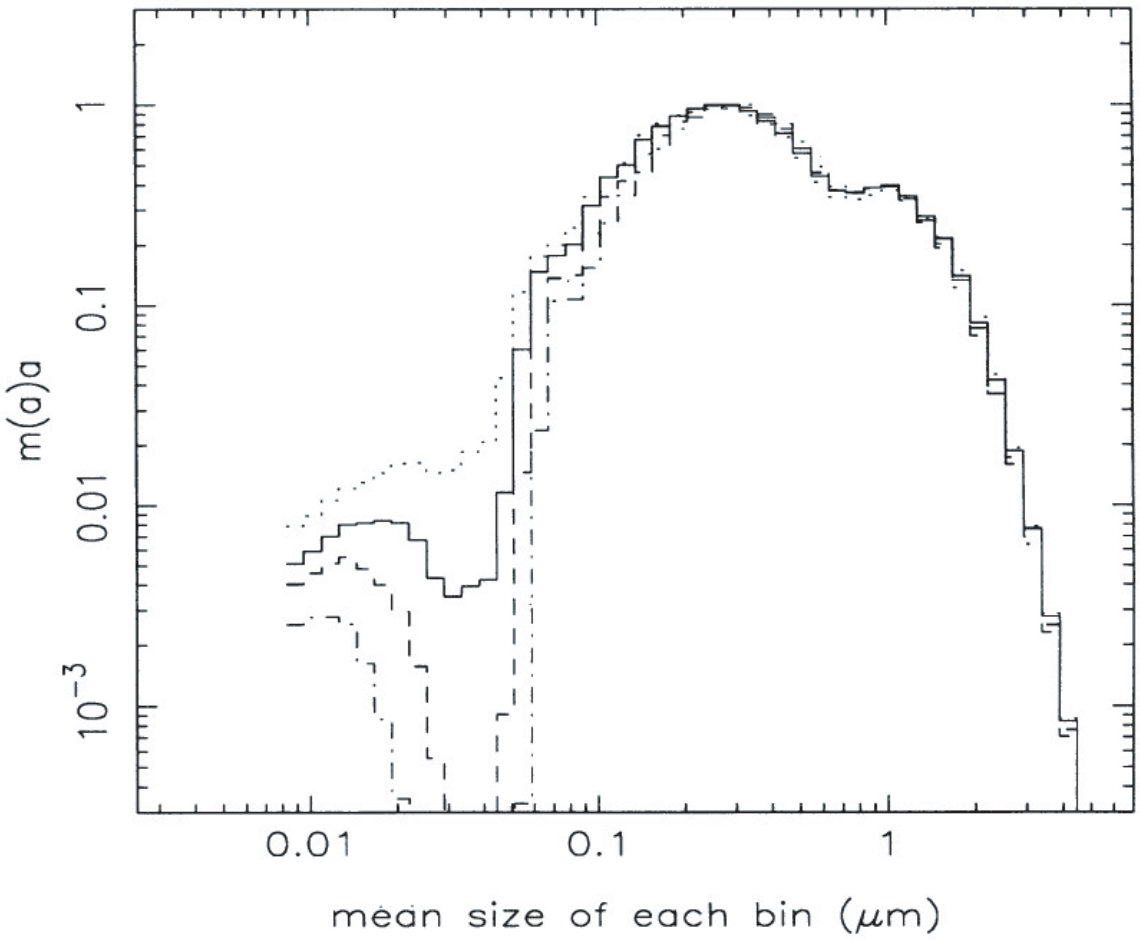

Figure 5.7: Mass distributions for 6:1 oblate spheroid model using "astronomical silicate (Draine & Lee 1984)" (Fig. 3*b* of Kim & Martin 1995b). Resultant mass distributions normalized to their maxima. The four lines are the fits to data from modified Serkowski curves using the maximum entropy method: dotted for HD 7252, solid for $\lambda_{\max} = 0.55$ μm, dashed for $\lambda_{\max} = 0.615$ μm, and dot-dashed for $\lambda_{\max} = 0.68$ μm.

5.4 Conclusion

We have examined the wavelength dependence of interstellar polarization at NIR toward the GC, based on the survey data.

The ratios of degree of polarization are $p_H/p_J = 0.581 \pm 0.004$ and $p_{K_S}/p_H = 0.620 \pm 0.002$, which correspond to $\beta_{JH} = 2.08 \pm 0.02$ and $\beta_{HK_S} = 1.76 \pm 0.01$ for the power law indices of the wavelength dependence of polarization. Degree of polarization keeps still higher than that expected from a single power law toward longer wavelengths (flattening from 1.25 to 2.14 μm). The flattening invokes greater numbers of aligned large-size dust grains in the mass distribution derived by Kim & Martin (1995b).

Bibliography

Behr, A. 1959, Zs. Astrophys., 47, 54

Coyne, G. V., Gehrels, T., & Serkowski, K. 1974, AJ, 79, 581

Creese, M., Jones, T. Jay., Kobulnicky, H. A. 1995, AJ, 110, 268

Draine, B. T. & Lee, H. M. 1984, ApJ, 285, 89

Draine, B. T. 2003, ARA&A, 41, 241

Dyck, H. M., & Jones, T. J. 1978, AJ, 83, 594

Gehrels, T. 1960, AJ, 65, 470

Kim, S.-H., & Martin, P. G. 1994, ApJ, 431, 783

Kim, S.-H., & Martin, P. G. 1995a, ApJ, 442, 172

Kim, S.-H., & Martin, P. G. 1995b, ApJ, 444, 293

Martin, P. G., & Whittet, D. C. B. 1990, ApJ, 357, 113

Martin, P. G., Adamson, A. J., Whittet, D. C. B., Hough, J. H., Bailey, J. A., Kim, S.-H., Sato, S., Tamura, M., & Yamashita, T. 1992, ApJ, 392, 691

Nagata, T. 1990, ApJ, 348, L13

Nagata, T., Kobayashi, N., & Sato, S. 1994, ApJ, 423, L113

Nishiyama, S., Nagata, T., Kusakabe, N., Matsunaga, N., Naoi, T., Kato, D., Nagashima, C., Sugitani, K., Tamura, M., Tanabe, T., & Sato, S. 2006, ApJ, 638, 839

Nishiyama, S., Tamura, M., Hatano, H., Kato, D., Tanabe, T., Sugitani, K., & Nagata, T. 2009b, ApJ, 696, 1407

Serkowski, K., Mathewson, D. L., & Ford, V. L. 1975, ApJ, 196, 261

Whittet, D. C. B., Martin, P. G., Hough, J. H., Rouse, M. F., Bailey, J. A., & Axon, D. J. 1992, ApJ, 386, 562

Wilking, B. A., Lebofsky, M. J., Kemp, J. C., Martin, P. G., & Rieke, G. H. 1980, ApJ, 235, 905

Wilking, B. A., Lebofsky, M. J., & Rieke, G. H. 1982, AJ, 87, 695

Chapter 6

Summary

We have carried out the NIR polarimetric imaging survey toward the GC using the IRSF 1.4 m telescope, NIR camera SIRIUS, and its polarimeter SIRPOL. The survey is planned to cover the region of $|l| \lesssim 2^\circ$ and $|b| \lesssim 1^\circ$, in which an area of about 7.6 deg^2 has been observed in the period from 2006 to 2009.

We have reduced and analyzed the survey data for an area of about 5.7 deg^2. The point source catalog, which contains positions (right ascension and declination), degrees of polarization, position angles, and magnitudes in the JHK_S bands for about 3.5 million sources, has been completed. For point sources, we have evaluated the accuracy of photometry to be about 0.03 mag, that of polarimetry to be about 0.3% for polarization degree and about 4° for position angle, and that of astrometry to be about $0\farcs02$ for right ascension and declination. The limiting magnitudes to polarization degree error of 1% are 14.0 mag, 13.4 mag, and 12.5 mag in the J, H, and K_S bands, respectively.

We have investigated the magnetic field toward the GC from position angles and the interstellar polarization efficiency. Most of position angles for the bulge sources are nearly parallel to the Galactic plane ($0^\circ \lesssim \langle\theta_{K_S}\rangle \lesssim 20^\circ$), indicating that the magnetic field between the GC and us runs almost parallel to the spiral arms and that this longitudinal direction shows the direction of the uniform component of the magnetic field. The average polarization efficiency of the ISM between the GC and us is about three times lower than that of the ISM close to us. Unlike the spatial variations of color excess and polarization degree depending on Galactic latitude, the polarization efficiency varies independently of the Galactic structure (from about 1 to 5% / mag in the K_S band). To the lines of sight with large dispersions of position angles, the polarization efficiency is low, and vice versa. These results for the polarization efficiency suggest that the directions of magnetic fields between the GC and us deviate from the longitudinal direction and are different each to each along the line-of-sight due to the random component of the magnetic field. Comparing our data with the model involving the decorrelation length of the random component of the magnetic field, we have suggested higher magnetic field strength of the random component relative to the uniform one between the GC and us. This higher strength of the random component may reflect violent activities in the GC.

We have also examined the wavelength dependence of interstellar polarization at the NIR wavelengths. The ratios of polarization degree were derived to be $p_H/p_J = 0.581 \pm 0.004$ and $p_{K_S}/p_H = 0.620 \pm 0.002$, the power law indices to be $\beta_{JH} = 2.08 \pm 0.02$ and $\beta_{HK_S} = 1.76 \pm 0.01$. Thus degree of polarization decreases less rapidly than that expected by a single power law (flattening toward longer wavelengths from 1.25 to 2.14 μm). To explain the flattening, great numbers of aligned large-size grains should be necessary.

We have presented the results of the polarimetric imaging survey toward the GC. The extensive survey data can also provide us an opportunity to work on the following scientific subjects:

(1) The magnetic field structure in the solar neighborhood based on disk sources.

(2) The three-dimensional structure of magnetic field based on periodic variable stars such as Cepheids and Miras, which have been catalogued with their distances on literatures.

(3) The magnetic field structures of known dark clouds, H II regions, and supernova remnants, which are expected to be perturbed from the uniform, large-scale magnetic field structure.

(4) The properties of dust grains derived from not only NIR interstellar polarization but also *extinction*.

(5) Search for YSOs and AGBs, which are intrinsically polarized sources.

Appendix A

Extended Polarized Sources toward the Galactic Center

Our survey allows us to detect and measure polarization for not only point sources but also extended sources. In this chapter, we present the results of search for extended polarized sources toward the GC.

A.1 Search for Extended Polarized Sources

From the survey data, we searched for extended polarized sources on Stokes I, Q, U, and PI images by eye inspection; extended sources with a size of larger than about $10''$ and having nonzero Q and/or U and PI values were sought out on images. We found 11 sources within the analyzed area (Fig. 3.1). Identifiers and positions of the sources are listed in Table A.1. Table A.1 also lists identifiers of the same sources, which have been also identified in previous studies.

In Figures A.1−A.10, JHK_S composite I and PI images, and K_S band polarization vector maps of the sources are shown. The spatial distribution of the sources is shown in Figure A.11.

Table A.1: Extended Polarized Sources

ID	α (J2000)[a]	δ (J2000)[b]	l[c]	b[d]	ID in previous studies
1	17:45:46.7	−28:05:29	0.739	0.410	ISOGAL-PJ174546.6−280529[e]
2	17:46:24.3	−29:22:23	−0.284	−0.374	[DB2000] 56[f], SF2[g]
3	17:45:39.4	−29:23:31	−0.385	−0.244	g35962−1[h], SF1-A[g]
4	17:45:41.2	−29:22:21	−0.365	−0.240	SF1-B[g]
5	17:47:44.3	−28:15:28	0.821	−0.045	
6	17:47:09.2	−28:46:17	0.315	−0.201	
7	17:47:09.6	−28:46:09	0.318	−0.201	
8	17:46:34.6	−28:59:56	0.055	−0.211	ISOGAL-PJ174634.6−285955[e]
9	17:47:19.9	−29:11:55	−0.031	−0.456	[FC2000] G359.97−0.46[i], SF3[g]
10	17:50:24.1	−28:50:27	0.622	−0.847	
11	17:49:30.2	−28:53:06	0.484	−0.701	

[a,b] Units of right ascension are hours, minutes, and seconds, and units of declination are degrees, arcminutes, and arcseconds.
[c,d] Units of Galactic longitude and latitude are degrees.
[e] Felli et al. (2002).
[f] Borissova et al. (2005).
[g] Nagayama et al. (2009).
[h] Testi et al. (1998).
[i] Forster & Caswell (2000).

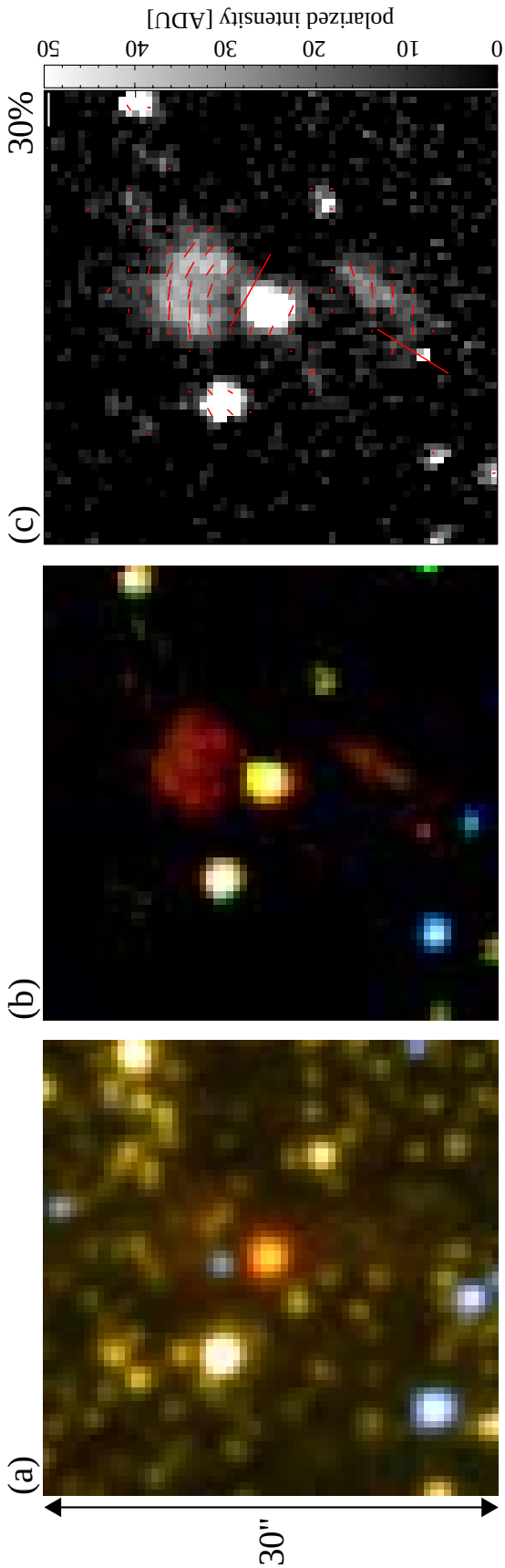

Figure A.1: (*a*) JHK_S composite I image of source 1. (*b*) JHK_S composite PI image of source 1. (*c*) K_S band polarization vector map of source 1 superposed on the PI image in the K_S band. The length of each bar is proportional to p_{K_S}. Each bar is parallel to the $\boldsymbol{E}$-vector of polarization (θ_{K_S}). The values p_{K_S} and θ_{K_S} of each vector are calculated from average values of Q_{K_S}/I_{K_S} and U_{K_S}/I_{K_S} in each 3 pixel × 3 pixel. p_{K_S} is debiased using its error, which is calculated from average errors of Q_{K_S}/I_{K_S} and U_{K_S}/I_{K_S}. The bar for 30% scale of polarization degree is shown at the upper right of the figure. North is up, and east is to the left.

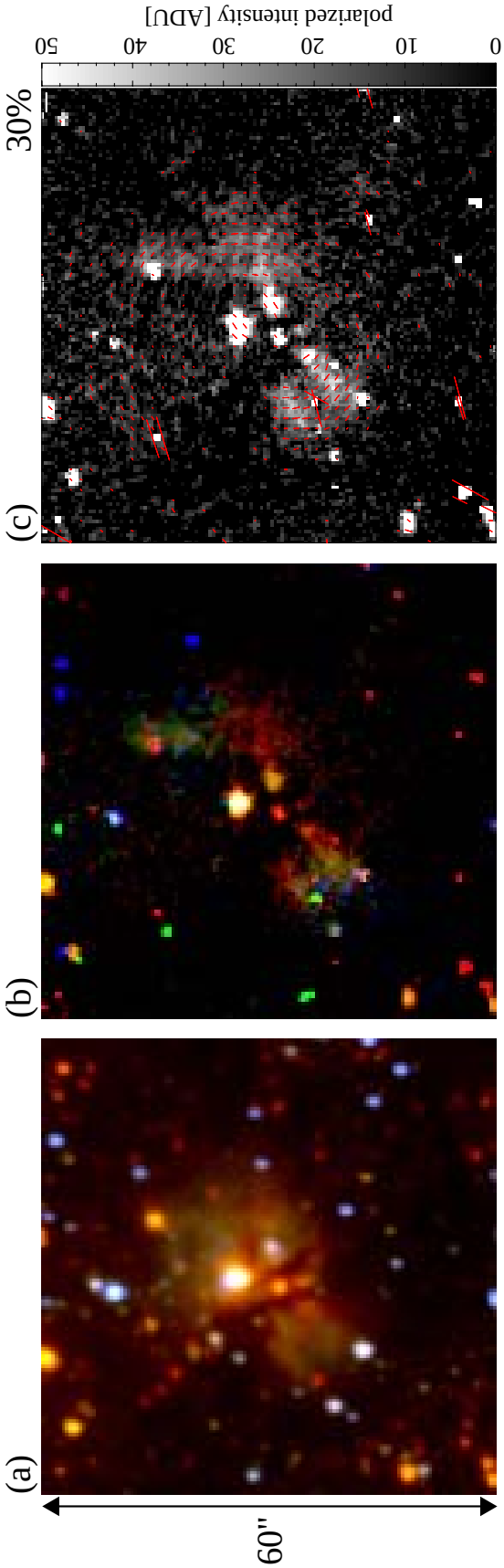

Figure A.2: Same as Figure A.1 except for source 2.

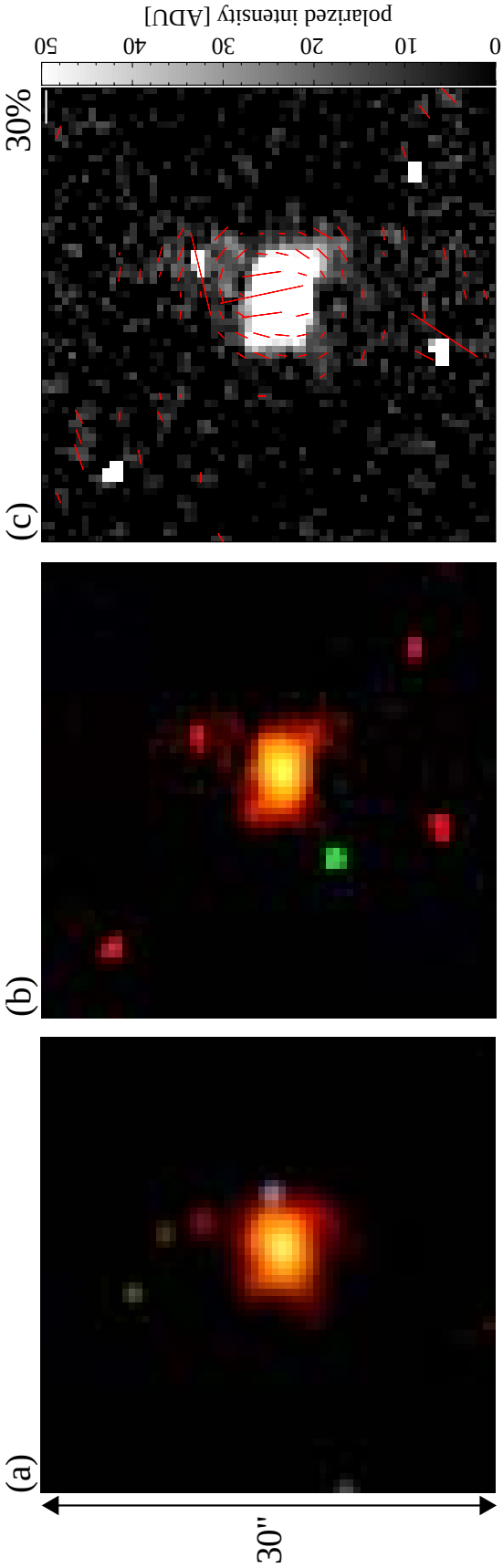

Figure A.3: Same as Figure A.1 except for source 3.

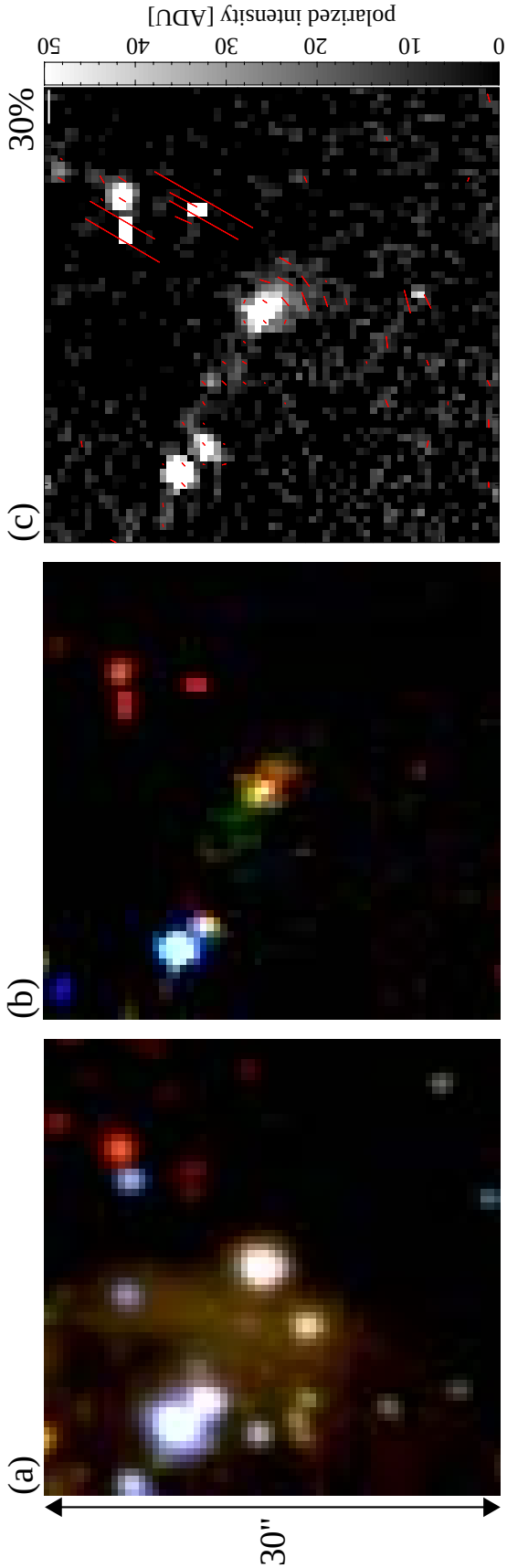

Figure A.4: Same as Figure A.1 except for source 4.

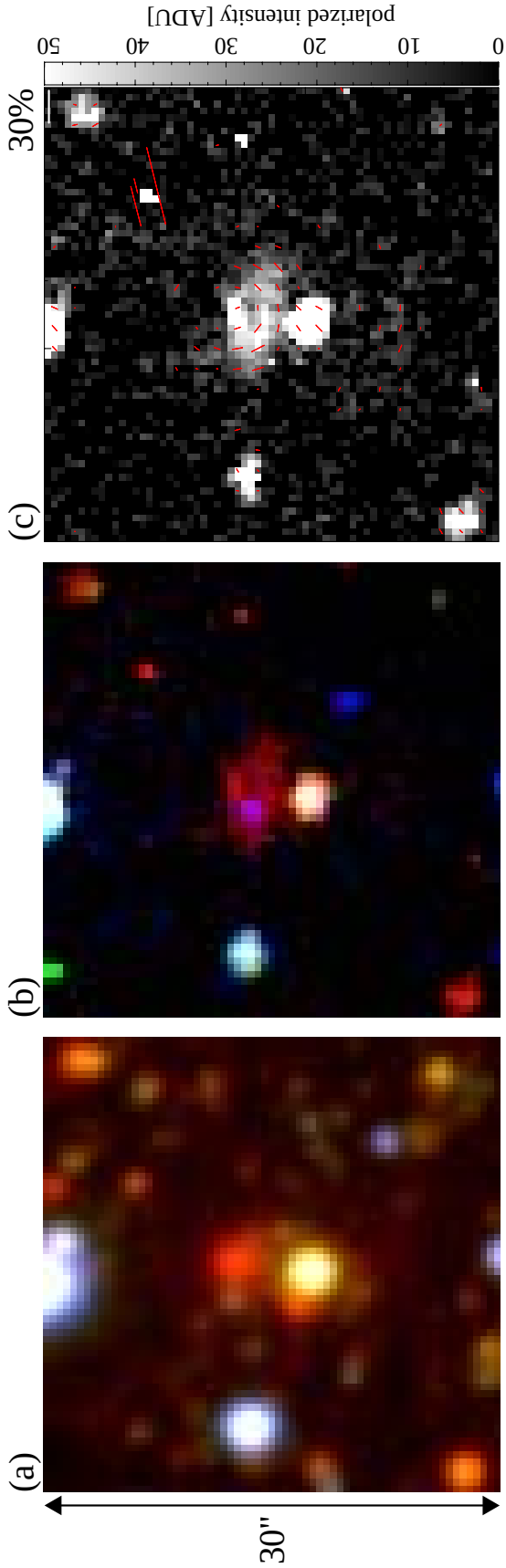

Figure A.5: Same as Figure A.1 except for source 5.

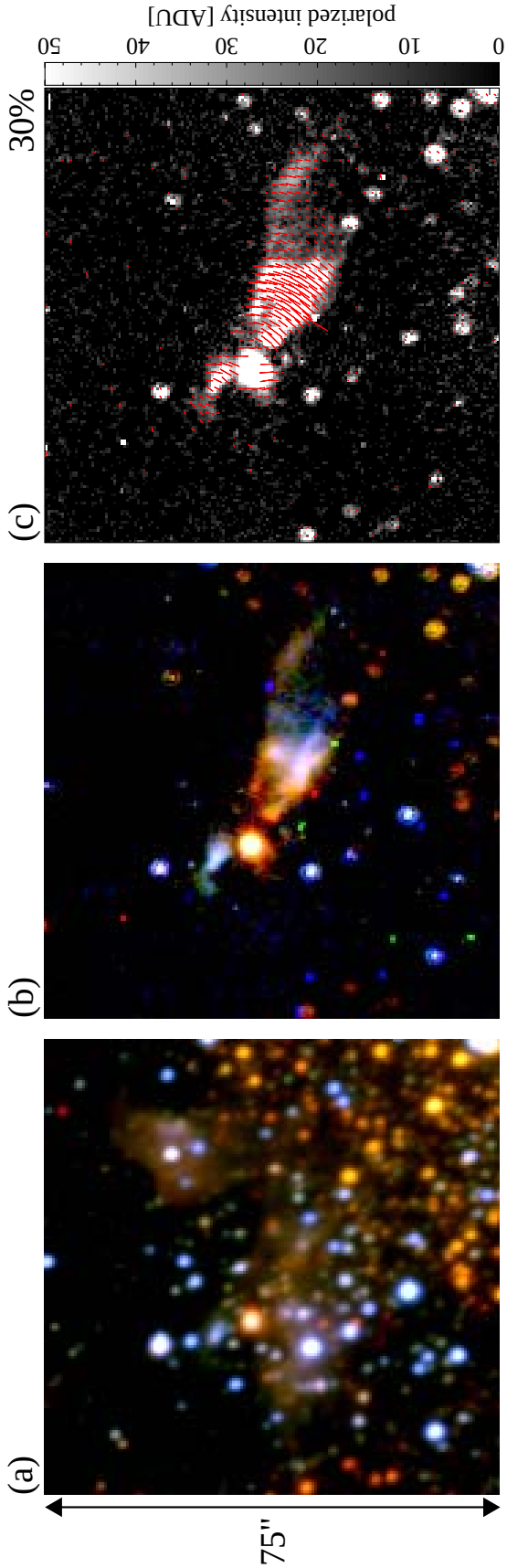

Figure A.6: Same as Figure A.1 except for sources 6 and 7.

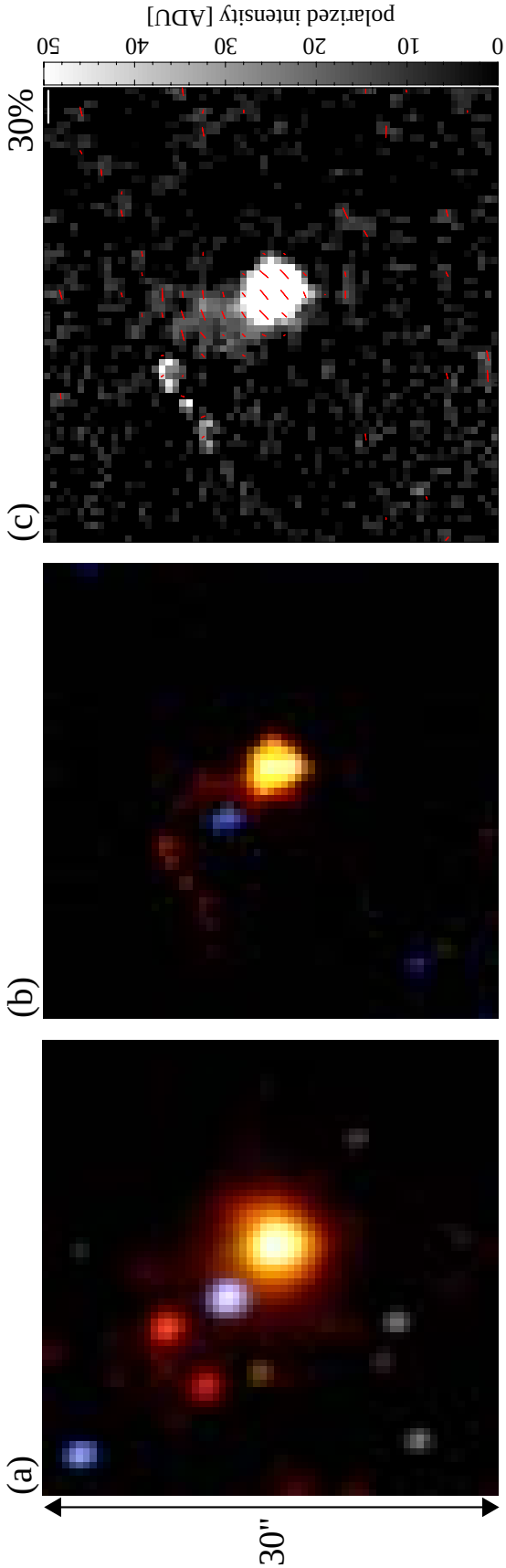

Figure A.7: Same as Figure A.1 except for source 8.

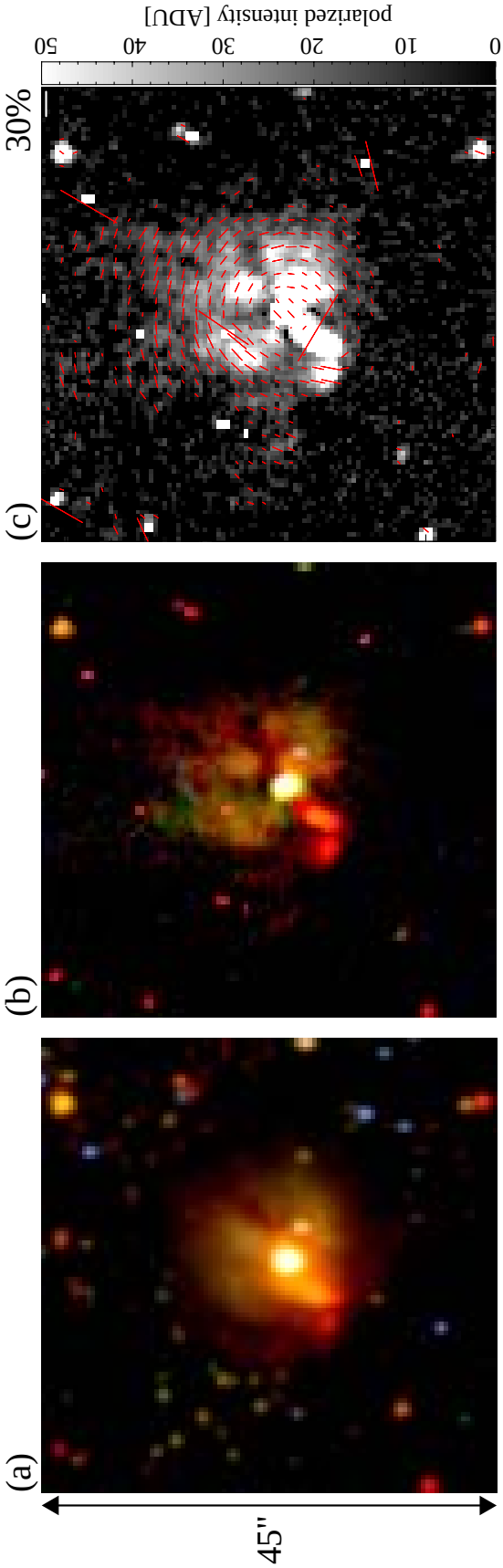

Figure A.8: Same as Figure A.1 except for source 9.

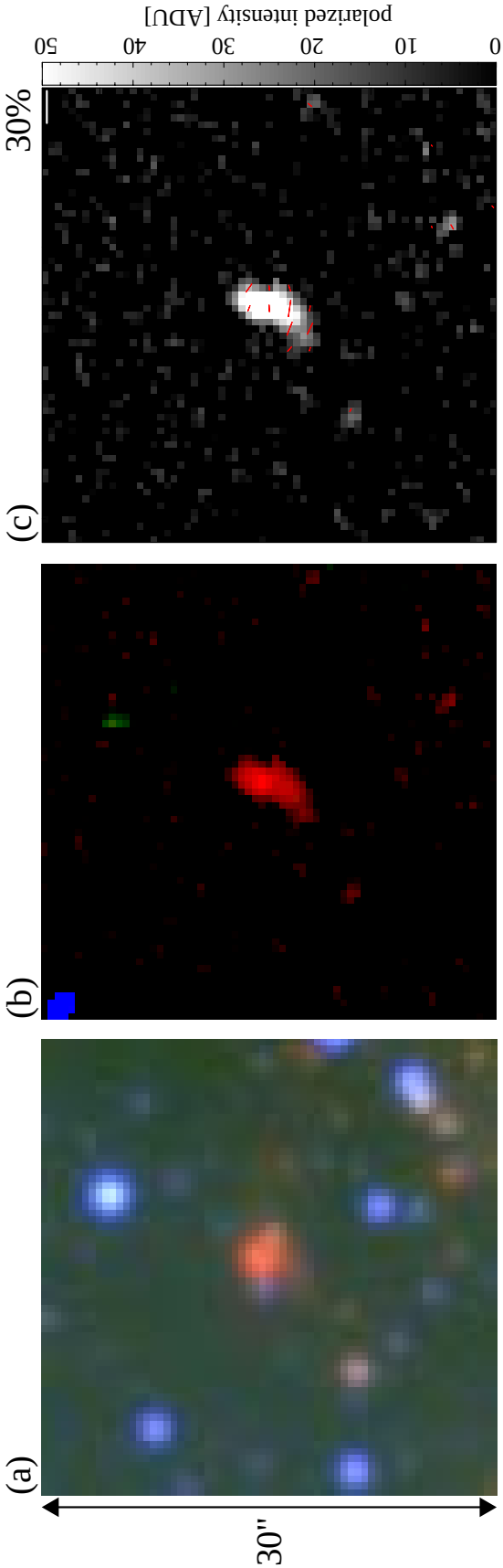

Figure A.9: Same as Figure A.1 except for source 10.

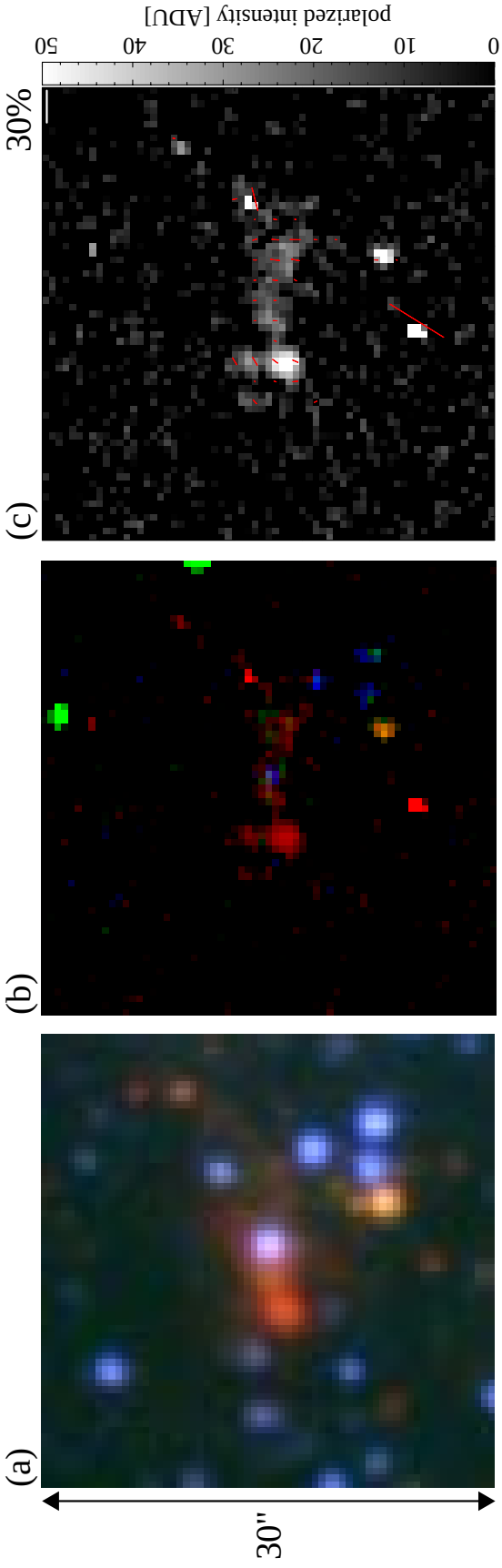

Figure A.10: Same as Figure A.1 except for source 11.

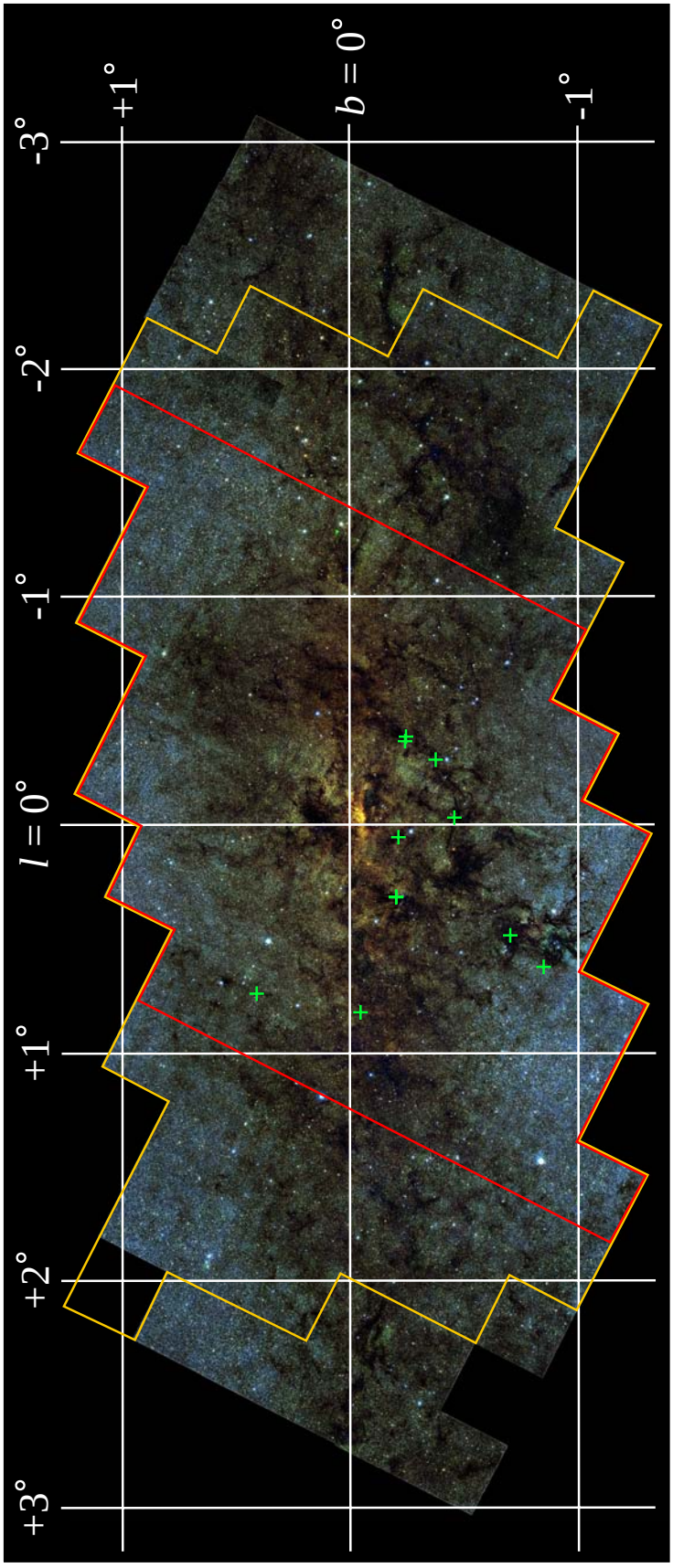

Figure A.11: Distribution of the extended polarized sources, which is shown by crosses. Background image is the JHK_S composite image of the GC (Fig. 1.5 of Nishiyama 2005). The survey area and analyzed area are indicated by yellow and red lines.

A.2 Each Extended Polarized Source

source 1

The extended polarized nebula shows a butterfly shape on the PI image (Fig. A.1b). The pattern of its polarization vectors is centrosymmetric (Fig. A.1c), suggesting that the nebula is associated with and illuminated by the central star (17454667−2805292; Table A.2), which is seen to be red on the I image (Fig. A.1a). The spectral energy distribution (SED) of the central star continuously rises from 1.25 to at least 5.8 μm (Fig. A.12a). The polarization of the central star is quiet large ($p_{K_S} \sim 18\%$) and its position angle ($\theta_{K_S} \sim 68°$) is almost perpendicular to the north-south extension of the reflection nebula. These suggest that the central star has an unresolved circumstellar structure (like a disk and/or envelope).

This source has been identified as a YSO candidate based on the ISO data at 7 and 15 μm (ISOGAL-PJ174546.6−280529; Felli et al. 2002).

source 2

The butterfly shaped nebula, which is seen on the PI image (Fig. A.2b), has two illuminating sources. The western side of the reflection nebula shows a centrosymmetric pattern of the polarization vectors (Fig. A.2c), whose normal lines point to the yellow bright source (17462423−2922182; Table A.2). This yellow illuminating source shows a SED rising toward the mid-infrared (MIR) wavelengths (Fig. A.12b). While the eastern side of the nebula is illuminated by the red faint star (17462432−2922237; Table A.2), to which each normal line of the centrosymmetric polarization vectors points. This red illuminating source shows a SED rising until 5.8 μm (Fig. A.12c). A dark lane, which divides the reflection nebula into the eastern and western sides, is seen around the red star (Fig. A.2a). The position angle of polarization of the red star ($\theta_{K_S} \sim 18°$) is roughly parallel to the dark lane and perpendicular to the southeastern extension of the eastern nebula.

This source has been identified as an ultracompact (UC) H II region ([DB2000] 56; Borissova et al. 2005, and SF2; Nagayama et al. 2009).

source 3

The red nebula shows a compact feature (Figs. A.3a and b). Its polarization vectors represent a centrosymmetric pattern (Fig. A.3c). Since the central star cannot be seen, it would be deeply embedded in the circumstellar structure.

This source has been identified as a YSO candidate based on JHK bands data (g35962−1; Testi et al. 1998), and an UC H II region (SF1-A; Nagayama et al. 2009). OH, H_2O, and CH_3OH masers, which are tracers of recent star formation, are associated with the source (359.62−0.25; Forster & Caswell 1989; Caswell 1996). Nagayama et al. (2009) suggested that the source is associated with a dark cloud (Fig. A.11), which is located at a distance of about 4 kpc from us and accompanies the masers.

source 4

The polarized bipolar nebula shows a centrosymmetric pattern of the polarization vectors (Figs. A.4*b* and *c*). Degrees of polarization at the northeastern side of the nebula are smaller than those at its southwestern side. This would be because of dilution of the polarized light by the emission from a local H II region (RCW 137; Rodgers et al. 1960), which is seen on the I image (Fig. A.4*a*). The central star (17454118−2922214; Table A.2) shows a flat SED until it rises at 4.5 μm (Fig. A.12*d*).

This source has been identified as an UC H II region (SF1-B; Nagayama et al. 2009).

source 5

The diffuse polarized nebula shows a centrosymmetric pattern of the polarization vectors (Fig. A.5*b* and *c*). The normal lines of each polarization vector point to the red source on the I image (Fig. A.5*a*), suggesting that it is the illuminating source of the reflection nebula (17474429−2815287; Table A.2), and that the yellow bright star is not associated with the nebula but a foreground source. The illuminating source shows a SED with IR excess and a peak at 5.8 μm (Fig. A.12*e*).

source 6

A conspicuous monopolar nebula is seen at the center of Figure A.6*b*. Its polarization vectors show a centrosymmetric pattern (Fig. A.6*c*), indicating that the illuminating central source is the bright red star (17470924−2846161; Table A.2) on the I image (Fig. A.6*a*). Large polarization ($p_J \sim 40\%$) of the central star implies the existence of an unresolved circumstellar structure. Its position angle ($\theta_J \sim 2^\circ$) is nearly perpendicular to the elongation of the reflection nebula. The SED of the central star rises until 5.8 μm (Fig. A.12*f*).

The source accompanies two CH_3OH masers (0.315−0.201 and 0.316−0.201; Caswell 1996).

source 7

Toward the northeast of source 6, a small bipolar nebula is seen (Fig. A.6*b*). The pattern of its polarization vectors is centrosymmetric (Fig. A.6*c*). The central star cannot be seen at the NIR wavelengths.

There are a star cluster ([DB2000] 6; Dutra & Bica 2000) and an H II region (RCW 141; Rodgers et al. 1960) at the south of sources 6 and 7, suggesting active star formation in this region.

source 8

The bright red source (17463456−2859559; Table A.2), which is seen on the I image (Fig. A.7a), illuminates a monopolar nebula (Fig. A.7b). The reflection nebula shows a centrosymmetric pattern of the polarization vectors (Fig. A.7c). Its elongation is almost perpendicular to position angle of polarization of the illuminating source ($\theta_H \sim 120°$). The illuminating source shows a SED rising toward the MIR wavelengths (Fig. A.12g).

This source has been identified as a YSO candidate (ISOGAL-PJ174634.6−285955; Felli et al. 2002).

source 9

The polarization vectors of the polarized nebula show a pattern of a concentric circle (Fig. A.8c). The illuminating source is the bright yellow star (Fig. A.8a; 17471985−2911545; Table A.2), whose SED rises until 2.2 μm and is almost flat from 2.2 to 8.0 μm (Fig. A.12h).

This source has been identified as an UC H II region (GC359.970−0.456 A; Forster & Caswell 2000, and SF3; Nagayama et al. 2009). The source accompanies a YSO candidate (g35997−1; Testi et al. 1998) situated at about 7″ southeast of the central star. The candidate is the red faint source at the edge of the nebula on the PI image (Fig. A.8b). OH, H_2O, and CH_3OH masers are associated with the candidate (359.97−0.46; Forster & Caswell 1989; Caswell 1996). The associations of the source and masers with a 4 kpc dark cloud have been suggested by Nagayama et al. (2009).

source 10

The polarization vectors of the diffuse polarized nebula show a centrosymmetric pattern (Fig. A.9b and c). The central star is seen to be fairly red on the I image (Fig. A.9a), and is detected only at wavelengths longer than 2.2 μm (17502403−2850269; Table A.2). The SED of the central star shows IR excess, and peaks at 4.5 μm (Fig. A.12i).

source 11

The diffuse monopolar nebula shows a centrosymmetric pattern of the polarization vectors (Fig. A.10b and c). The illuminating source is not detected in the J band (17493018−2853054; Table A.2), and shows highly red color on the I image (Fig. A.10a). The SED of the illuminating source rises until 5.8 μm (Fig. A.12j).

Table A.2: Central Stars of Extended Polarized Sources

ID	ID of central star	α (J2000)[a]	δ (J2000)[b]	l[c]	b[d]
1	17454667−2805292	17:45:46.67	−28:05:29.2	0.73916	0.41040
2	17462423−2922182	17:46:24.23	−29:22:18.2	−0.28291	−0.37277
	17462432−2922237	17:46:24.32	−29:22:23.7	−0.28404	−0.37384
4	17454118−2922214	17:45:41.18	−29:22:21.4	−0.36499	−0.23973
5	17474429−2815287	17:47:44.29	−28:15:28.7	0.82102	−0.04531
6	17470924−2846161	17:47:09.24	−28:46:16.1	0.31555	−0.20122
8	17463456−2859559	17:46:34.56	−28:59:55.9	0.05523	−0.21120
9	17471985−2911545	17:47:19.85	−29:11:54.5	−0.02993	−0.45570
10	17502403−2850269	17:50:24.03	−28:50:26.9	0.62239	−0.84659
11	17493018−2853054	17:49:30.18	−28:53:05.4	0.48373	−0.70054

[a,b] Units of right ascension are hours, minutes, and seconds, and units of declination are degrees, arcminutes, and arcseconds.
[c,d] Units of Galactic longitude and latitude are degrees.

p_J [%]	δp_J [%]	θ_J [°]	$\delta\theta_J$ [°]	J [mag]	δJ [mag]	p_H [%]	δp_H [%]	θ_H [°]	$\delta\theta_H$ [°]	H [mag]	δH [mag]
39.35	4.35	59.86	2.95	16.139	0.025	33.19	0.51	70.71	0.41	12.688	0.017
6.23	0.84	178.07	3.76	13.553	0.107	5.39	0.14	174.53	0.72	10.360	0.024
-	-	-	-	-	-	1.76	4.38	119.75	26.72	14.025	0.027
2.51	0.62	5.74	7.49	13.457	0.050	1.16	0.14	20.89	3.31	11.536	0.037
-	-	-	-	-	-	-	-	-	-	15.726	0.051
40.00	2.45	178.72	1.67	14.554	0.073	-	-	-	-	12.471	0.083
1.67	0.41	124.03	6.82	13.496	0.015	1.54	0.07	119.92	1.26	9.902	0.016
12.14	0.68	153.51	1.76	13.762	0.040	6.74	0.14	155.11	0.58	10.446	0.032
-	-	-	-	-	-	-	-	-	-	-	-
-	-	-	-	-	-	6.84	2.75	161.72	11.08	15.799	0.138

* A hyphen means that the source is not detected in the band.

Table A.2: *Continued*

p_{K_S} [%]	δp_{K_S} [%]	θ_{K_S} [°]	$\delta\theta_{K_S}$ [°]	K_S [mag]	δK_S [mag]
17.59	0.13	67.81	0.22	9.938	0.009
-	-	-	-	7.672[e]	0.027[e]
0.92	0.76	125.84	18.27	10.716	0.036
0.70	0.10	26.64	4.22	10.169	0.018
2.69	0.30	21.51	3.18	11.282	0.078
-	-	-	-	10.181[f]	0.048[f]
-	-	-	-	7.292[e]	0.021[e]
-	-	-	-	7.799[e]	0.023[e]
5.64	0.20	78.47	1.01	11.118	0.072
5.77	0.46	149.30	2.32	11.994	0.119

[e] The data are from the 2MASS Point Source Catalog (Skrutskie et al. 2006) due to saturation of the bright sources in the survey data.
[f] The data are from the 2MASS Point Source Catalog because the source is not detected in the K_S band in the survey data due to confusion. It is noted that photometry of the source by 2MASS and that in the J and H bands by us would contain unresolved multiple sources.

[3.6] [mag]	δ[3.6] [mag]	[4.5] [mag]	δ[4.5] [mag]	[5.8] [mag]	δ[5.8] [mag]	[8.0] [mag]	δ[8.0] [mag]
-	-	-	-	2.935	0.003	-	-
-	-	-	-	3.689	0.006	-	-
-	-	5.533	0.006	4.106	0.005	3.209	0.006
8.253	0.006	7.995	0.007	5.683	0.007	-	-
9.582	0.008	-	-	7.438	0.008	7.871	0.016
7.294	0.006	5.884	0.005	5.516	0.008	-	-
-	-	-	-	3.201	0.005	-	-
6.162	0.018	5.067	0.006	4.159	0.006	3.167	0.005
-	-	6.261	0.003	-	-	5.181	0.006
7.319	0.005	5.751	0.007	4.074	0.004	3.663	0.007

[*] The data for Spitzer/IRAC (3.6, 4.5, 5.8, and 8.0 μm) magnitudes and their errors are from Ramirez et al. (2008).

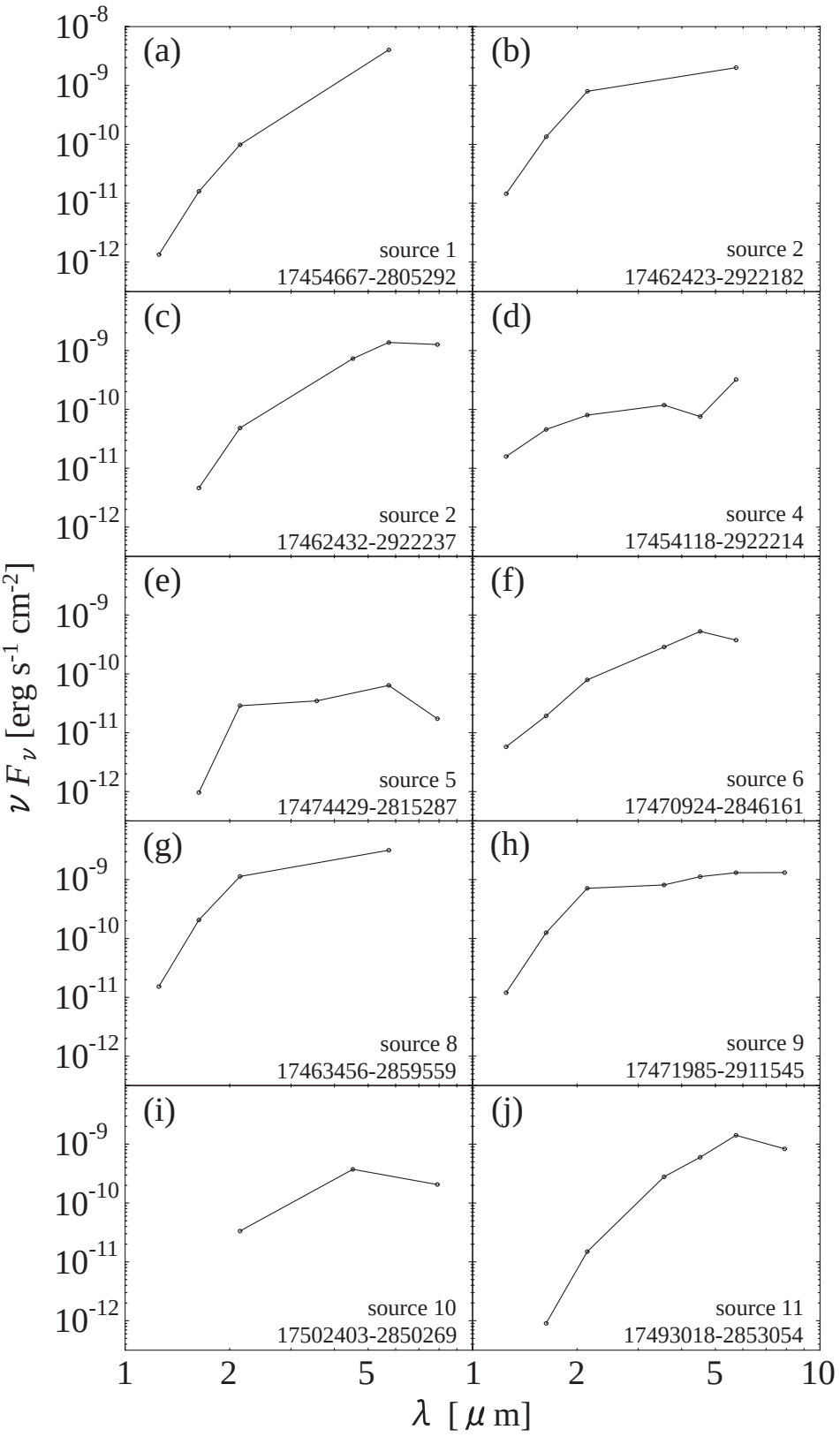

Figure A.12: SEDs of the central stars of the extended polarized sources. The central wavelength and zero-point flux of each band are listed in Table A.3.

Table A.3: Central Wavelength and Zero-Point Flux of Each Band

	J	H	K_S	[3.6]	[4.5]	[5.8]	[8.0]
central wavelengths [μm]	1.25	1.63	2.14	3.56	4.52	5.73	7.91
zero-point flux [Jy][a]	1594	1024	666.8	280.9	179.7	115.0	64.13

[a] The values in the J, H, and K_S bands are not in the IRSF system, but in the 2MASS system (Cohen et al. 2003). The values at 3.6, 4.5, 5.8, and 8.0 μm are from Reach et al. (2005).

A.3 Conclusion

We have searched for extended polarized sources in about $3^\circ \times 2^\circ$ region toward the GC by eye inspection. As a result, we have identified 11 extended polarized sources. The polarized nebulae of all the sources show centrosymmetric patterns of the polarization vectors, suggesting that the nebulae are illuminated by their central stars and that circumstellar structures (disks and/or envelopes) exist. The central illuminating sources show IR excess in their SEDs. Among the sources, 6 sources have been identified as YSO candidates or UC H II regions in the previous studies, and the others were newly discovered in this study.

Bibliography

Borissova, J., Ivanov, V. D., Minniti, D., Geisler, D., & Stephens, A. W. 2005, A&A, 435, 95

Caswell, J. L. 1996, MNRAS, 283, 606

Cohen, M., Wheaton, Wm. A., & Megeath, S. T. 2003, AJ, 126, 1090

Dutra, C. M. & Bica, E. 2000, A&A, 359, L9

Felli, M., Testi, L., Schuller, F., & Omont, A. 2002, A&A, 392, 971

Forster, J. R., & Caswell, J. L. 1989, A&A, 213, 339

Forster, J. R. & Caswell, J. L. 2000, ApJ, 530, 371

Nagayama, T., Sato, S., Nishiyama, S., Murai, Y., Nagata, T., Hatano, H., Kurita, M., Tamura, M., Nakajima, Y., Sugitani, K., Oka, T., & Sofue, Y. 2009, PASJ, 61, 283

Nishiyama, S., 2005, Ph.D. thesis, Nagoya University

Ramirez, S. V., Arendt, R. G., Sellgren, K., Stolovy, S. R., Cotera, A., Smith, H. A., Yusef-Zadeh, F. 2008, ApJS, 175, 147

Reach, W. T., Megeath, S. T., Cohen, M., Hora, J., Carey, S., Surace, J., Willner, S. P., Barmby, P., Wilson, G., Glaccum, W., Lowrance, P., Marengo, M., & Fazio, G. G. 2005, PASP, 117, 978

Rodgers, A. W., Campbell, C. T., & Whiteoak, J. B. 1960, MNRAS, 121, 103

Skrutskie, M. F., Cutri, R. M., Stiening, R., Weinberg, M. D., Schneider, S., Carpenter, J. M., Beichman, C., Capps, R., Chester, T., Elias, J., Huchra, J., Liebert, J., Lonsdale, C., Monet, D. G., Price, S., Seitzer, P., Jarrett, T., Kirkpatrick, J. D., Gizis, J. E., Howard, E., Evans, T., Fowler, J., Fullmer, L., Hurt, R., Light, R., Kopan, E. L., Marsh, K. A., McCallon, H. L., Tam, R., Van Dyk, S., Wheelock, S. 2006, AJ, 131, 1163

Testi, L., Felli, M., Persi, P., & Roth, M. 1998, A&AS, 129, 495

Appendix B

Interstellar Extinction Map toward the Galactic Center

B.1 Introduction

Because of high degree and nonuniformity of interstellar extinction toward the GC by intervening dust in the Galactic plane, it is difficult to study the properties of stellar populations in the Galactic bulge and the structure of the bulge itself. A detailed interstellar extinction map has been needed, and several efforts using NIR and MIR observations have been devoted for last two decades (Table B.1).

The first wide field interstellar extinction map of a $2^\circ \times 1^\circ$ area around the GC was provided by Catchpole et al. (1990) (Fig. B.1). They compared K magnitudes and $H-K$ colors of sources with those of giant branch of 47 Tuc in each $400'' \times 400''$ cell to determine extinction values. Schultheis et al. (1999) used the data in the J and K_S bands from the DENIS survey together with isochrones calculated for red giant branch (RGB) and asymptotic giant branch (AGB) phases. They mapped interstellar extinction toward the inner Galactic bulge between $-8^\circ < l < 8^\circ$ and $-1.^\circ5 < b < 1.^\circ5$ with steps of $1'$ (radius of sampling windows is $2'$; Fig. B.2). Dutra et al. (2003) have drawn the interstellar extinction map toward the central $10^\circ \times 10^\circ$ of the Galaxy (Fig. B.3). Extinction values were determined by comparing K_S magnitudes and $J-K_S$ colors from 2MASS with those

Table B.1: Interstellar Extinction Maps toward the GC

	area	resolution	data	extinction
Catchpole et al. (1990)	$2^\circ \times 1^\circ$	$400''$	H, K	$A_V = 0{-}35$ mag
Schultheis et al. (1999)	$16^\circ \times 3^\circ$	$4'$	J, K_S (DENIS)	$A_V = 0{-}35$ mag
Dutra et al. (2003)	$10^\circ \times 10^\circ$	$4'$	J, K_S (2MASS)	$A_{K_S} = 0{-}3$ mag
Schultheis et al. (2009)	$2^\circ \times 1.^\circ4$	$2'$	J, K_S (2MASS), [3.6], [5.8] (Spitzer)	$A_V = 0{-}90$ mag
this study	$3^\circ \times 2^\circ$	$30''$	H, K_S (IRSF)	$E(H-K_S) = 0{-}3$ mag

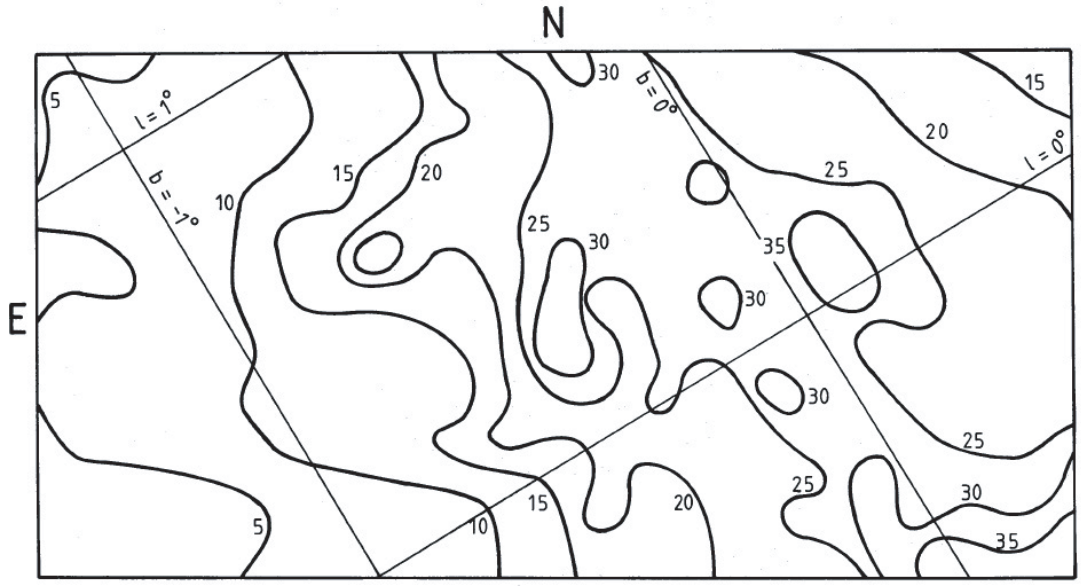

Figure B.1: Contour map of A_V on the plane-of-the-sky based on observations of the most frequent value of A_V made in adjacent 400 × 400 arcsec^2 area of sky (Fig. 4 of Catchpole et al. 1990). Galactic coordinates are also shown.

of the upper RGB of Baade's window on color-magnitude diagrams in each $4' \times 4'$ cell. Measured visual extinction A_V ranges from about 5 to 35 mag in these studies. These authors suggested a general trend of decreasing (increasing) extinction values away from (close to) the Galactic plane and the presence of filamentary and clumpy structures in regions with high extinction.

The previous interstellar extinction maps derived from NIR observations cannot trace high extinction. Schultheis et al. (2009) suggested that the values only for regions where A_V is less than 25 mag in the maps are realistic. And they derived a new interstellar extinction map of the GC region ($2^\circ \times 1.^\circ 4$), extending to much higher values of A_V from a comparison of the 2MASS data in the J, K_S bands and the Spitzer/IRAC data at 3.6, 5.8 μm with isochrones for evolved (RGB and AGB) stars (Fig. B.4). The values in $2' \times 2'$ cells were determined from $J - K_S$ colors for $A_V < 20$ mag, while [3.6]−[5.8] colors for $A_V > 20$ mag. The highest values of A_V they detected reach about 90 mag.

The interstellar extinction maps toward the GC previously published have an angular resolution of $\geq 2'$. Gosling et al. (2006, 2009) conducted high-resolution observations toward the GC ($1.^\circ 6 \times 0.^\circ 8$) using VLT/ISAAC, and suggested that the characteristic scale for the size of complex structures in the ISM is $5-15''$. In this chapter, we present a new interstellar extinction map toward the GC with an angular resolution of $30''$ using the survey data. Although our interstellar extinction map also cannot resolve the small-scale structures, the map is the finest map now available thanks to higher resolution compared with DENIS and 2MASS.

Figure B.2: Map of extinction in the inner Galactic bulge (Fig. 3 of Schultheis et al. 1999; http://www-denis.iap.fr/articles/extinction/emap.ps). The image color represents an A_V range in magnitudes from 0 (black) to 35 (white).

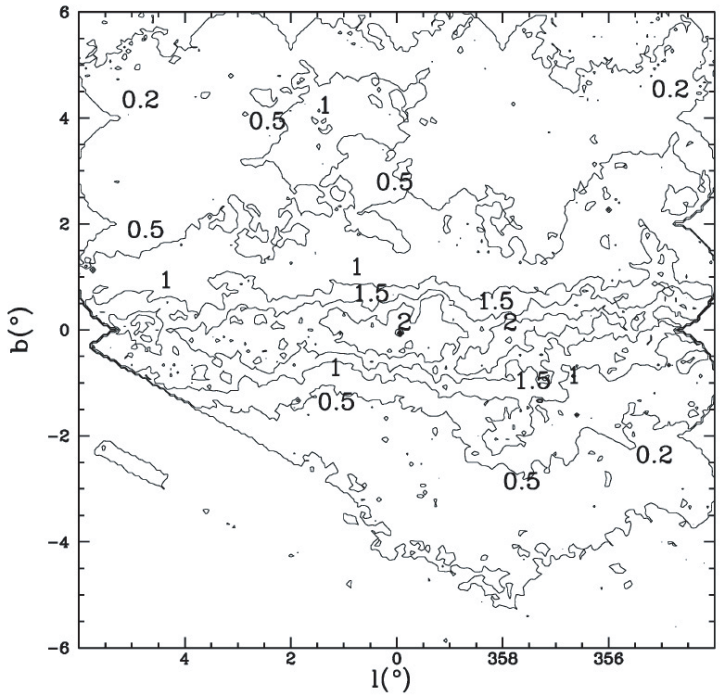

Figure B.3: A_K extinction map within 10° × 10° of the GC (Fig. 3 of Dutra et al. 2003). The contours represent the following extinction values: $A_K = 0.2$, 0.5, 1.0, 1.5, and 2.0.

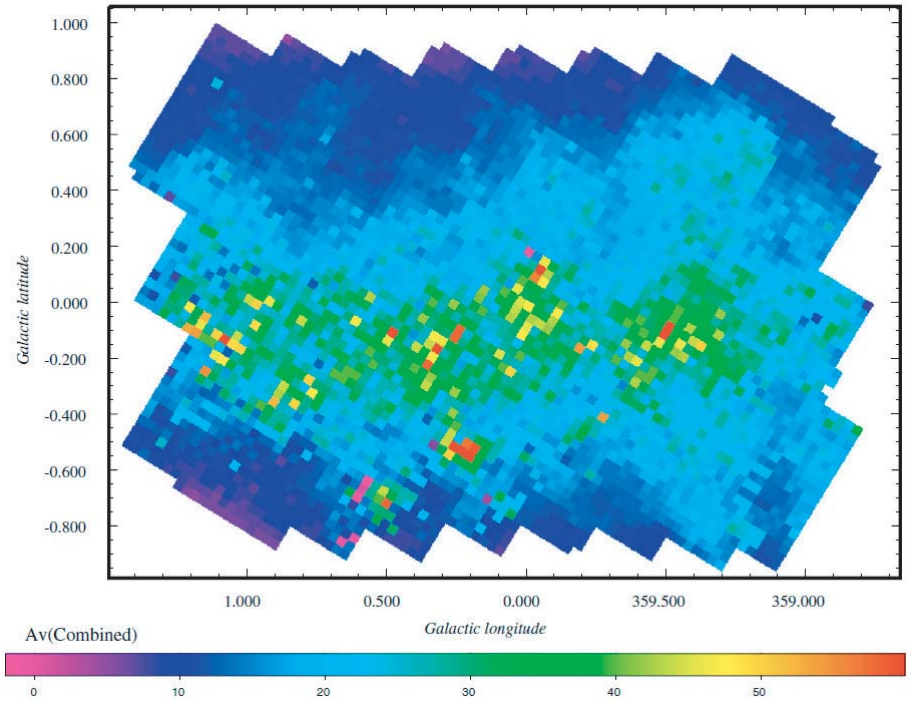

Figure B.4: Combined interstellar extinction map of the central 280 pc × 200 pc of the GC (Fig. 4 of Schultheis et al. 2009). For $A_V < 20$ 2MASS $J - K_S$ color was used, while $A_V > 20$ IRAC [3.6]−[5.8] color was used.

B.2 Results and Discussion

The procedures to construct an interstellar extinction map toward the GC are same for Figure 4.6 (§4.2.2), except for using the bulge sources with $\delta(H - K_S) \leq 0.1$ mag and cells with a size of $30'' \times 30''$. In Figure B.5, we present the resultant map, which is expressed by means of color excess $\langle E(H - K_S) \rangle$ for the bulge sources.

The map shows the spatial variation of extinction, which starts from $\langle E(H - K_S) \rangle \sim 2$ mag near the Galactic plane and decreases to $\langle E(H - K_S) \rangle \lesssim 0.5$ mag toward high Galactic latitude. A lot of clumpy and filamentary structures of extinction are seen especially close to the Galactic plane. These general features are similar to the results of the previous studies, particularly that of Schultheis et al. (2009, Fig. B.4). However, fine structures of clumps and filaments can be seen in our map by virtue of higher resolution compared to the previous studies. A chain of filamentary structures lying from $\sim(-30', -10')$ to $\sim(10', -30')$ corresponds to the dark clouds located at a distance of about 4 kpc from us (Nagayama et al. 2009). A clump at the eastern tip of the chain is one of the regions with the highest extinction in our observed area, and no sources are detected toward the dense part of the clump. A clump centered on $\sim(-5', 10')$ is also one of the highest extinction regions, and may be a nearby dark cloud away from the GC as well.

The uncertainty map is calculated as standard deviations of $E(H - K_S)$ for the bulge sources in each cell (Fig. B.6). The standard deviations of $E(H - K_S)$ are higher to the lines of sight with higher extinction, indicating that there exist unresolved structures in the ISM (Gosling et al. 2006, 2009) and that extinction values steeply vary from line-to-line of sight.

As in the cases of the interstellar extinction maps obtained from NIR observations, the values for high extinction regions in our map must be underestimated. We check how deep our map (IRSF map) can trace extinction by comparing it with the map of Schultheis et al. (2009; Spitzer map) based on MIR observations. First we apply common grids of the Spitzer map with a size of $2' \times 2'$ to our data, then calculate means of $E(H - K_S)$ for the bulge sources in each cell. To compare the values in $E(H - K_S)$, the values A_V of the Spitzer map are converted to $E(H - K_S)$. We once convert the values A_V to $E(J - K_S)$ using the interstellar extinction law $E(J - K_S) = 0.167 \times A_V$ (Glass 1999), and convert to $E(H - K_S)$ using $E(H - K_S)/E(J - K_S) = 0.343$ (Nishiyama et al. 2006). Figure B.7 shows a comparison between extinction values $E(H - K_S)_{\rm IRSF}$ in the IRSF map and $E(H - K_S)_{\rm 2MASS\&Spitzer}$ in the Spitzer map. Both values provide good agreement up to about 1.5 mag, but beyond this limit some values $E(H - K_S)_{\rm 2MASS\&Spitzer}$ are higher than values $E(H - K_S)_{\rm IRSF}$. This indicates that the IRSF map is able to trace extinction toward the GC adequately only for the regions where $E(H - K_S) \lesssim 1.5$ mag. The limit corresponds to $A_V \sim 26$ mag using the conversion factor from Glass (1999). Recently from observations toward the GC, Nishiyama et al. (2008) reported smaller conversion factor $[E(J - K_S) = 0.126 \times A_V]$ than the classical ones. If we adopt the factor, the limit is equivalent to $A_V \sim 35$ mag.

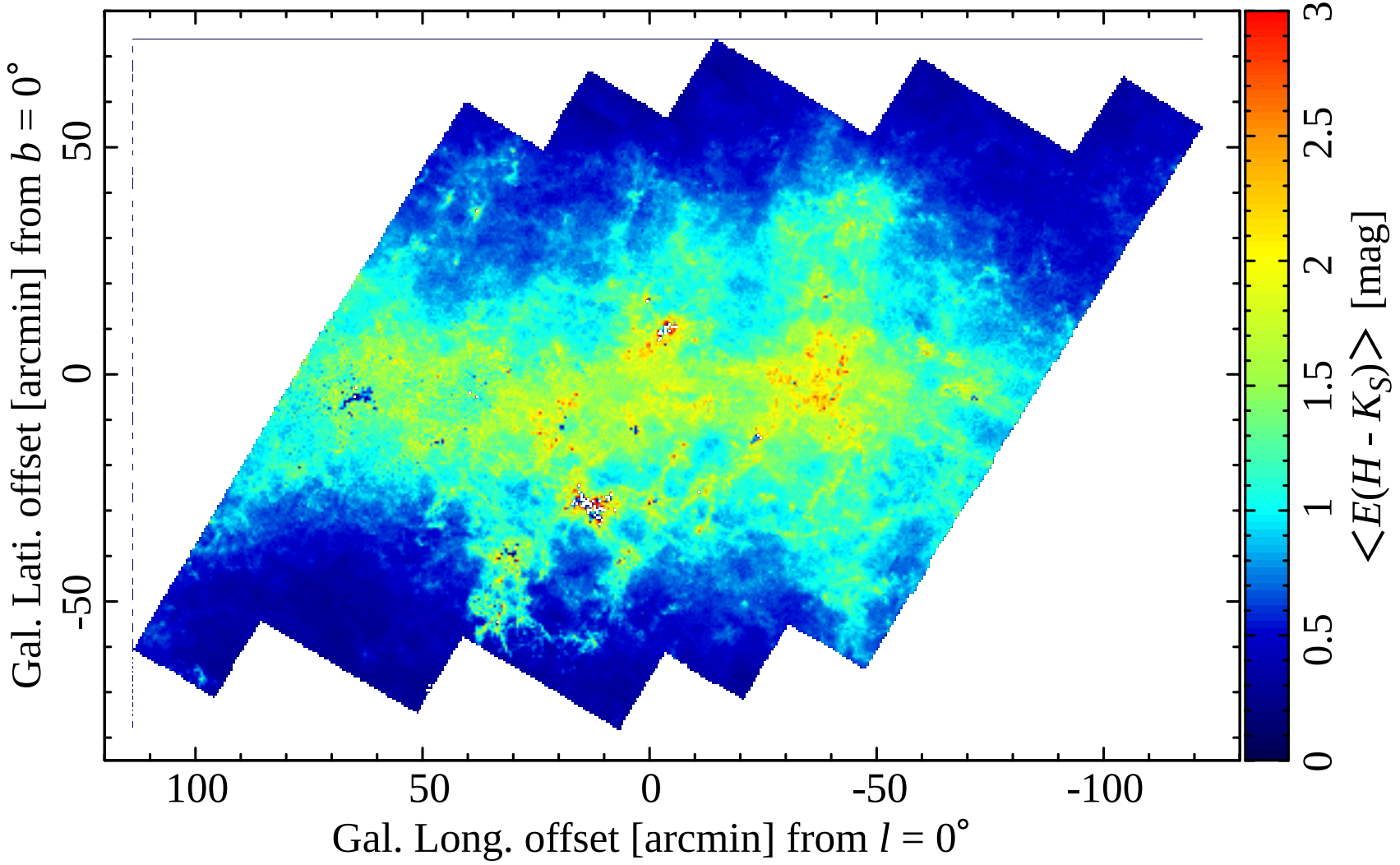

Figure B.5: Interstellar extinction map toward the GC. Each pixel represents a mean of $E(H-K_S)$ for the bulge sources with $\delta(H-K_S) \leq 0.1$ mag in each cell with a size of $30'' \times 30''$. The white pixels include no sources and means cannot be measured.

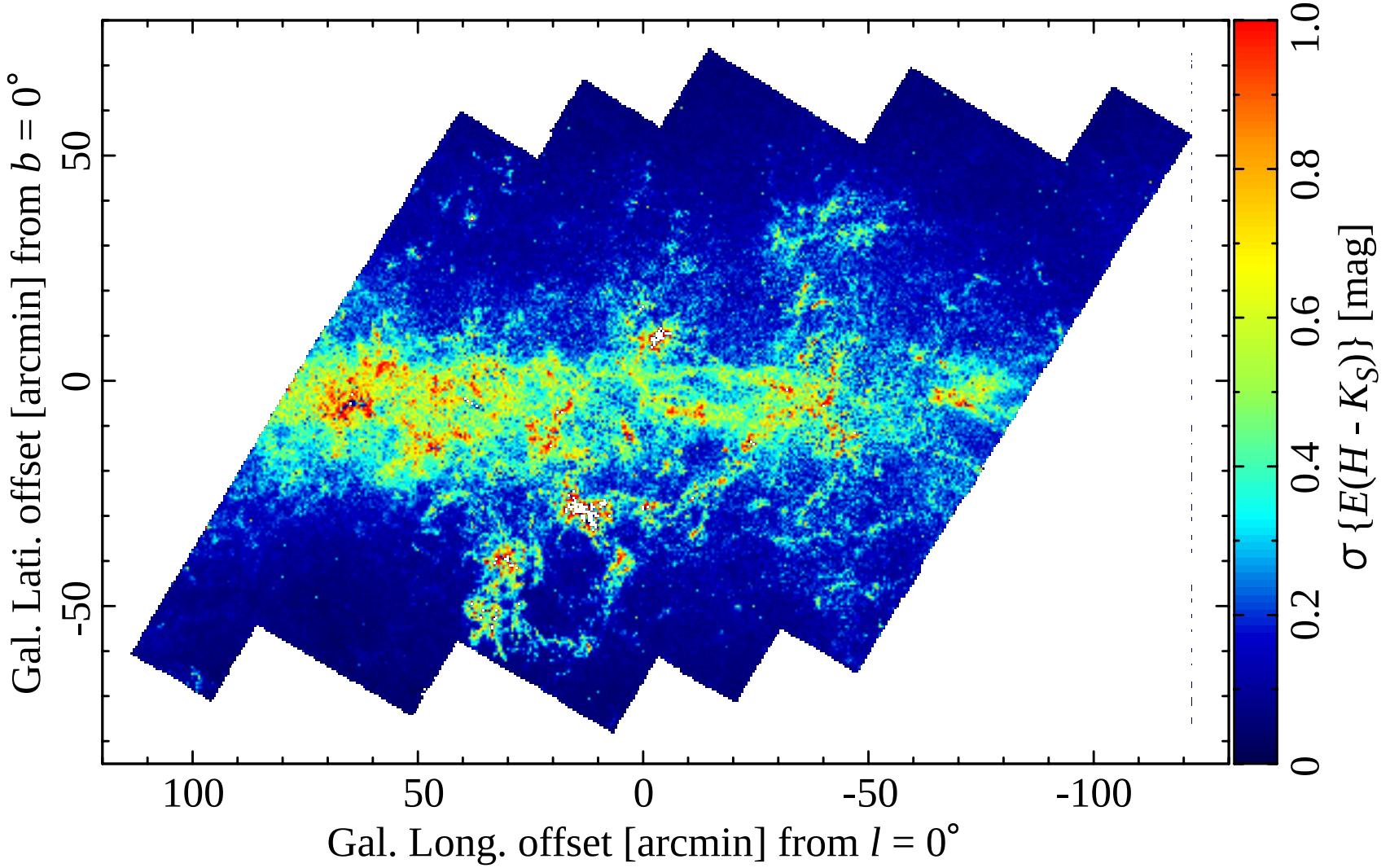

Figure B.6: Uncertainty map of the interstellar extinction map. Each pixel represents a standard deviation of $E(H-K_S)$ for the bulge sources with $\delta(H-K_S) \leq 0.1$ mag in each cell with a size of $30'' \times 30''$. The cells including one or no source(s) are drawn by white pixels.

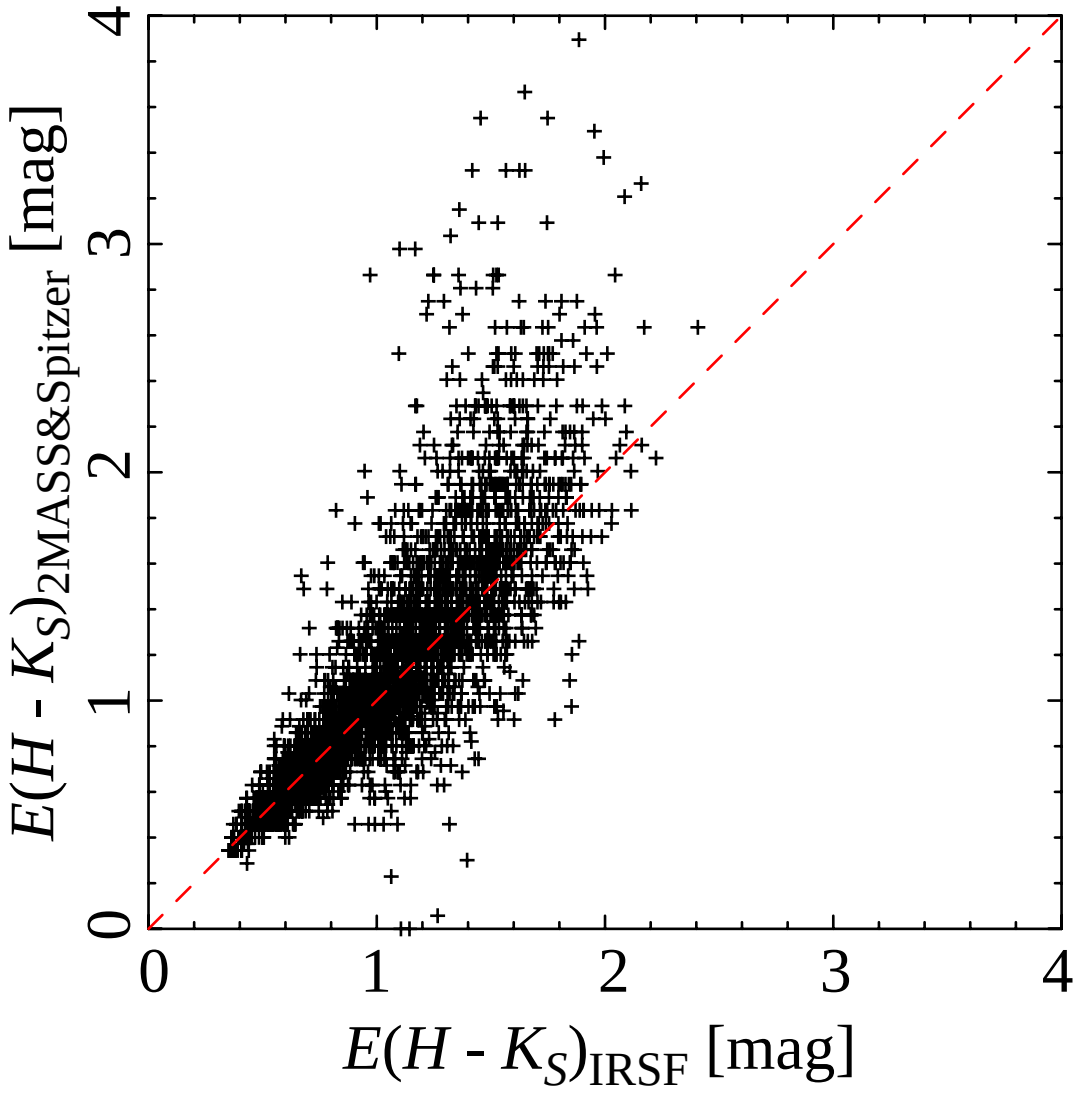

Figure B.7: Comparison between extinction values $E(H - K_S)_{\rm IRSF}$ and $E(H - K_S)_{\rm 2MASS\&Spitzer}$ for each cell with $2' \times 2'$ in size. The dashed line represents the identity function.

B.3 Conclusion

We have presented the interstellar extinction map toward the GC obtained from the survey data. The map has the angular resolution of $30''$, which is the finest among the maps now available, and shows unprecedented fine structures of clumps and filaments. The sensitivity of the map is limited to $E(H - K_S) \lesssim 1.5$ mag, which corresponds to $A_V \lesssim 35$ mag. Beyond this limit, extinction values toward the GC should be underestimated.

Bibliography

Catchpole, R. M., Whitelock, P. A., & Glass, I. S. 1990, MNRAS, 247, 479

Dutra, C. M., Santiago, B. X., Bica, E. L. D., & Barbuy, B. 2003, MNRAS, 338, 253

Glass, I. S. 1999, Handbook of Infrared Astronomy (Cambridge: Cambridge Univ. Press)

Gosling, A. J., Blundell, K. M., & Bandyopadhyay, R. 2006, ApJ, 640, L171

Gosling, A. J., Bandyopadhyay, R. M., & Blundell, K. M. 2009, MNRAS, 366

Nagayama, T., Sato, S., Nishiyama, S., Murai, Y., Nagata, T., Hatano, H., Kurita, M., Tamura, M., Nakajima, Y., Sugitani, K., Oka, T., & Sofue, Y. 2009, PASJ, 61, 283

Nishiyama, S., Nagata, T., Kusakabe, N., Matsunaga, N., Naoi, T., Kato, D., Nagashima, C., Sugitani, K., Tamura, M., Tanabe, T., & Sato, S. 2006, ApJ, 638, 839

Nishiyama, S., Nagata, T., Tamura, M., Kandori, R., Hatano, H., Sato, S., & Sugitani, K. 2008, ApJ, 680, 1174

Schultheis, M., Ganesh, S., Simon, G., Omont, A., Alard, C., Borsenberger, J., Copet, E., Epchtein, N., Fouque, P., & Habing, H. 1999, A&A, 349, L69

Schultheis, M., Sellgren, K., Ramirez, S., Stolovy, S., Ganesh, S., Glass, I. S., & Girardi, L. 2009, A&A, 495, 157